Cal Poly

Caltech

SCEC
AN NSF+USGS CENTER

UC Irvine

UCLA

UC Santa Barbara

USC

Influence of Ground Motion Selection and Scaling Approaches on Seismic Performance Assessment of Bridges

Esra Zengin, Saiid Saiidi, Yousef Bozorgnia

Department of Civil and Environmental Engineering
University of California, Los Angeles

A report on research supported by United States Geological Survey and Southern California Earthquake Center

Report GIRS-2023-11

DOI: 10.34948/N3Z30Q

University of California, Los Angeles (headquarters)

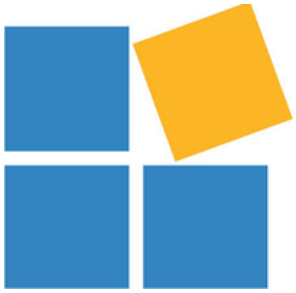

Natural Hazards Risk & Resiliency Research Center

B. John Garrick Institute for the Risk Sciences

Influence of ground motion selection and scaling approaches on seismic performance assessment of bridges

Esra Zengin, Saiid Saiidi, Yousef Bozorgnia

Civil and Environmental Engineering Department
University of California, Los Angeles

A report on research conducted with support from the California Department of Transportation.

Report GIRS-2023-11
DOI: 10.34948/N3Z30Q

Natural Hazards Risk and Resiliency Research Center
B. John Garrick Institute for the Risk Sciences
University of California, Los Angeles (Headquarters)

November 2023

ABSTRACT

NRHAs are carried out using sets of 25 ground motions, which are selected and scaled to be compatible with various target spectra based on different GMSS approaches at five target seismic hazard levels. The five pulse records are explicitly selected from the pool of 25, all of which fall within the specified pulse period range. In addition to the traditional GMSS approach, which scales the ground motion to a target spectrum derived from elastic probabilistic seismic hazard analysis (PSHA), a recently proposed GMSS approach is employed. This new approach scales the ground motion to target spectra derived from inelastic PSHA at various ductility levels, known as constant ductility inelastic spectra. The Uniform Hazard Spectrum (UHS) and the Conditional Mean Spectrum (CMS) are used as target spectra for both elastic and inelastic ground motion selection. The influence of GMSS approaches on the distribution of engineering seismic demand parameters (EDP), including column drift ratio, displacement ductility ratio, residual drift ratio, and the probability of exceeding damage states at return periods of 975 years and 2475 years, are examined. Fragility curves and EDP risk curves are derived for each site. The inelastic PSHA-based GMSS approach showed promise in reducing the dispersion in structural responses, particularly in high seismicity sites. The elastic PSHA-based GMSS approach can yield either conservative or unconservative results compared to the inelastic PSHA-based GMSS approach, depending on the mismatch between recorded and target inelastic spectra.

ACKNOWLEDGMENTS

This study was supported by the California Department of Transportation (Caltrans) and coordinated by the Natural Hazards Risk and Resiliency Research Center (NHR3) headquartered at UCLA. The support is gratefully acknowledged. The findings, conclusions, or recommendations in this publication are those of the authors and do not necessarily represent those of the sponsors.

The authors would like to express their sincere gratitude to Dr. Elmira Shoushtari for her support in OpenSees bridge modeling. Additionally, special thanks to Dr. Amarjeet Saini for generously providing the experimental fragility curve data used in this study.

CONTENTS

LIST OF FIGURES

LIST OF TABLES

1 Introduction

1.1. OVERVIEW

Understanding and predicting bridge responses to seismic events are critical for ensuring public safety and minimizing economic losses. Central to achieving this understanding are ground motion selection and scaling processes, which profoundly impact structural response, fragility curve assessment, and seismic risk evaluation. The choices made during the ground motion selection and scaling (GMSS) process may affect the results obtained from nonlinear response history analysis (NRHA). Therefore, the realistic selection of ground motions is crucial for obtaining reliable estimations of structural demands and ensuring the safety and reliability of bridges.

In seismic design, engineers commonly select ground motions based on the causal parameters of the controlling scenario event, such as magnitude, source-to-site distance, and site characteristics. Traditional GMSS approaches aim to "match" (in a general sense) the response spectra of records and target spectrum over a vibration period of interest. Commonly used GMSS approaches often employ the Uniform Hazard Spectrum (UHS) as the target spectrum. The UHS is typically derived from probabilistic seismic hazard analysis (PSHA) based on the elastic response of a single-degree-of-freedom (SDOF) oscillator. This method may be overly conservatist because it does not distinguish the structural period. As an alternative to UHS, the Conditional Mean Spectrum (CMS) has been proposed for seismic performance assessment and record selection that aims to overcome the inherent conservatism of UHS. Moreover, the Conditional Spectrum (CS) considers the aleatory variability of ground motions, providing a more comprehensive perspective on seismic risk assessment of structures. While the majority of GMSS approaches utilize elastic spectral ordinates of ground motion as the intensity measure (IM), other IMs such as peak ground motion values and damage indices have also been considered. Monteiro et al. (2019) showed that the Fajfar index (Iv), peak ground velocity (PGV), and root mean square velocity (vRMS) result in significantly lower dispersion across the fitted fragility curves for a population of bridges. Some studies have developed GMSS approaches that incorporate advanced scalar and vector IMs (Kohrangi et al. 2016, Tarbali et al. 2019, Zengin and Abrahamson (2020a, 2020b, 2021), Zengin 2022). Bradley (2010) introduced a generalized conditional intensity measure (GCIM) approach that explicitly considers various IMs beyond spectral accelerations, including cumulative absolute velocity, Arias Intensity, and significant durations.

Recently, Bahrampouri et al. (2023) introduced a methodology to incorporate the inelastic response of the SDOF oscillator in PSHA, addressing the limitations of relying solely on the elastic response of the SDOF oscillator. This approach aims to incorporate the effects of yielding, plastic deformation, and hysteretic energy dissipation, providing a more realistic, yet simple, more realistic representation of the behavior of the structure. The authors developed ground-motion models (GMMs) for inelastic SDOF system and computed PSHAs using the inelastic GMM. They also proposed a GMSS approach designed to select and scale ground motions to match the response spectra of these records with both elastic and inelastic target spectra across various ductility levels. This project presents different GMSS approaches and their impact on ground motion representation and bridge responses. The goal is to provide insights that can assist engineers and practitioners in making informed choices for seismic design and risk assessment of bridges in earthquake-prone regions.

1.2. OBJECTIVES AND SCOPE

This study aims to evaluate the impact of the traditional elastic PSHA-based and recently proposed inelastic PSHA-based GMSS approaches on the seismic performance assessment of a representative three-span bridge assumed to be located at five California sites, each with different seismicity: Oakland, Los Angeles, Long Beach, San Francisco, and San Bernardino. A modified version of the Arroyo de la Laguna bridge, designed according to Caltrans Seismic Design Criteria (SDC 2019), serves as the case study. The modeling involves simplifications, including the bridge being cast-in-place with integral bent caps, a zero-skew angle, seat-type abutment with sacrificial shear keys, and columns boundary conditions treated as two-way hinges. The scope of the study did not include the effect of variable pier heights, skew angle, and integral abutments and the backfill effect.

1.3. ORGANIZATION OF REPORT

Chapter 2 presents the target pseudo-spectral acceleration (PSA) levels derived from PSHA for five California sites considered. It also provides a concise overview of both elastic and inelastic-based GMSS approaches. A detailed description of a three-span bridge, including modeling assumptions, geometric and material properties, as well as the constitutive models adopted in the three-dimensional (3D) OpenSees model, has been presented. Chapter 2 also shows the results of moment-curvature, modal, and pushover analyses of the bridge model. Chapter 3 presents comparative analyses of different GMSS approaches on seismic response parameters (i.e., column drift ratio, ductility demand, residual drift ratio) of the three-span bridge. The chapter presents NRHA results obtained from 25 sets of ground motions that are selected and scaled to "follow" the mean target UHS and CMS, including pre-specified record-to-record variability, derived from elastic- and inelastic- PSHA at five return periods ranging from return periods T_R=200 to 5000 years. The chapter also explores the effect of pulse records on residual drift ratios, compares elastic

and inelastic analysis methods to assess the validity of equal displacement rule and evaluates the effects of GMSS approaches in terms of the probability of exceedance of damage states, fragility curves, and seismic risk curves for the bridge model. Chapter 4 summarizes the research findings and conclusions, along with a list of potential future research topics.

2 Ground Motion Selection and Scaling Approaches & Case Study Bridge

This chapter presents the information about the five California sites selected in this study and discusses the elastic and inelastic probabilistic seismic hazard analysis (PSHA) required to derive the target spectra for ground motion selection and scaling. It also provides a concise overview of the selected ground motions and highlights the differences between elastic and inelastic PSHA-based ground motion selection and scaling (GMSS) approaches. Additionally, this chapter provides a detailed description of a three-span bridge, including modeling assumptions, geometric and material properties, as well as the constitutive models adopted in three-dimensional (3D) OpenSees bridge model. Finally, the results of the moment-curvature, pushover, and modal analyses of the bridge model are presented.

2.1 SITE AND SEISMIC HAZARD DESCRIPTION

Site-specific elastic and inelastic PSHA were performed using the elastic and inelastic ground-motion models (GMMs) for ten sites in different seismicity regions of California in the study of Bahrampouri et al. (2023). Specifics of the elastic and inelastic PSHA results are reported in Bahrampouri et al. (2023), and summarized below:

- The sites were assumed to have rock site conditions with a shear wave velocity of V_{S30} = 760 m/s.
- The elastic GMM was NGA-West2 Campbell and Bozorgnia (CB14) model.
- A new GMM for inelastic single-degree-of-freedom (SDOF) system was developed. Similar to other NGA GMMs, the new inelastic model has median prediction as well as aleatory variability.
- Using the new inelastic GMM and UCERF3 seismic sources in California (Field et al. 2014), PSHA was computed for inelastic C_y spectra for each site, where C_y corresponds to the yield strength (F_y) to weight (W) ratio of an inelastic SDOF system.
- Computations of the inelastic PSHA were carried out using OpenSHA software program (Field et al. 2003).

According to the Caltrans Seismic Design Criteria (SDC 2019), the design spectrum for Safety Evaluation Earthquake (SEE) is derived from a 5% probability of exceedance in 50 years (975-year return period). This spectrum is practically equivalent to a 7% probability of exceedance in 75 years, representing the assumed bridge 75-year design life. Seismic demand is assessed using a 5% damped pseudo-spectral acceleration (PSA) response spectrum. Out of the ten sites, five were chosen based on their PSA level and PSA ratio. The PSA ratio was calculated by dividing the PSA at the return period (T_R) of 2475 years by the PSA at T_R=975 years. The target fundamental period was assumed to be 1.0 second (which was verified by the finite element analysis). Figure 2.1 illustrates the UHS of 10 CA cites at T_R=975 years and T_R=2475 years. Figure 2.2 illustrates the PSA ratios and the average PSA ratio of the sites. Using the aforementioned criteria, San Bernardino, Long Beach, Oakland, San Francisco and Los Angeles were selected. Table 2.1 lists the latitude and longitude information of the sites. Figure 2.3 illustrates the site-specific seismic hazard curves based on elastic PSHA. The seismicity ranking of the sites based on a return period of 975 years revealed the following order: San Bernardino ranked highest in terms of seismic hazard, followed by Oakland, Los Angeles, San Francisco, and Long Beach. These findings elucidated seismic vulnerability differences among sites, emphasizing the significance of site-specific characteristics for assessing seismic risks. The target spectra, i.e., CMS and UHS, were computed at five return periods of TR=200, 475, 975, 2475, and 5000 years.

Table 2.2 lists the PSA (T=1.0 s) values used to represent the elastic target intensity measure (IM) levels at each return period. It is evident that PSA (T=1.0 s) for San Bernardino is approximately twice the value for Long Beach for TR of up to 975. For TR of 2475 and 5000 the ratio is nearly 1.5. Figure 2.4 illustrates the UHS of inelastic C_y for various ductility (μ) levels for the city of San Bernardino. As expected, (see, e.g., Bozorgnia et al. 2010; Bozorgnia and Bertero 2004), Cy demand decreased as the μ increased.

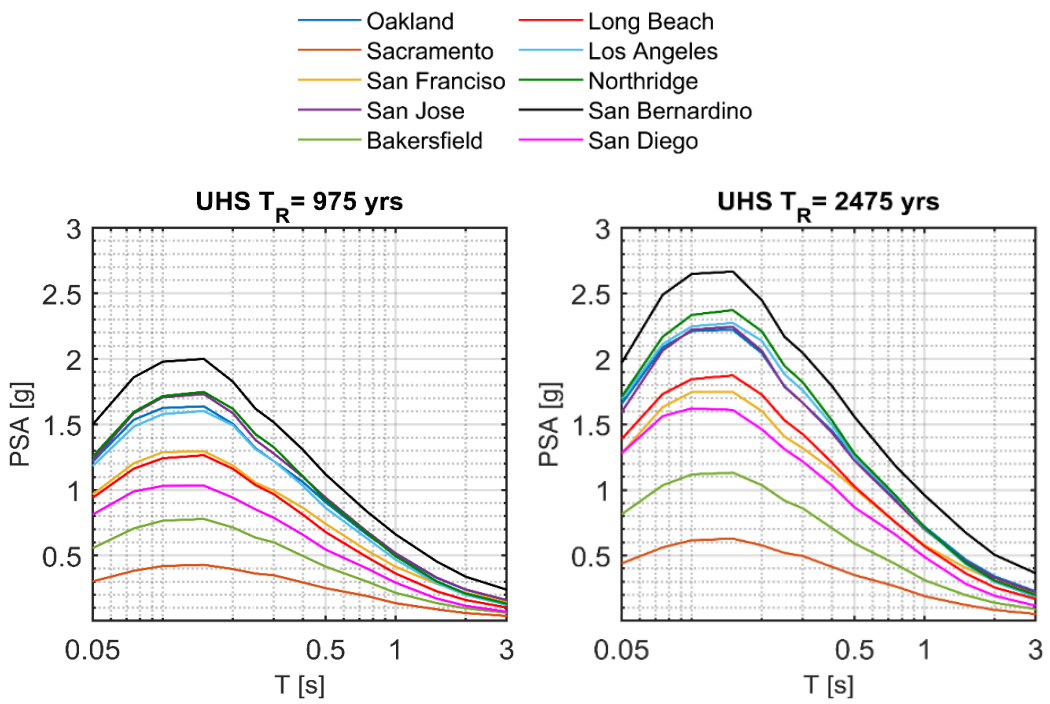

Figure 2. 1. UHS for ten CA sites at T_R=975 years (left panel), and at T_R=2475 years (right panel).

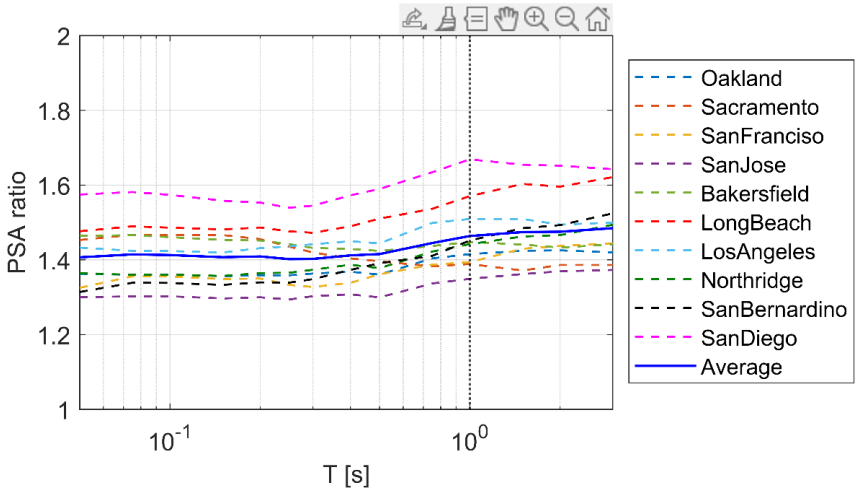

Figure 2. 2. PSA ratios (UHS T_R=2475/T_R=975 years) of the ten CA sites and the average PSA ratio.

Table 2. 1. Latitude and longitude information of the five selected sites in California.

Site	Longitude (°)	Latitude (°)
Oakland	-122.27255	37.8053046
San Francisco	-122.41926	37.7792597
Long Beach	-118.19564	33.7680362
Los Angeles	-118.24293	34.0535267
San Bernardino	-117.29276	34.1045714

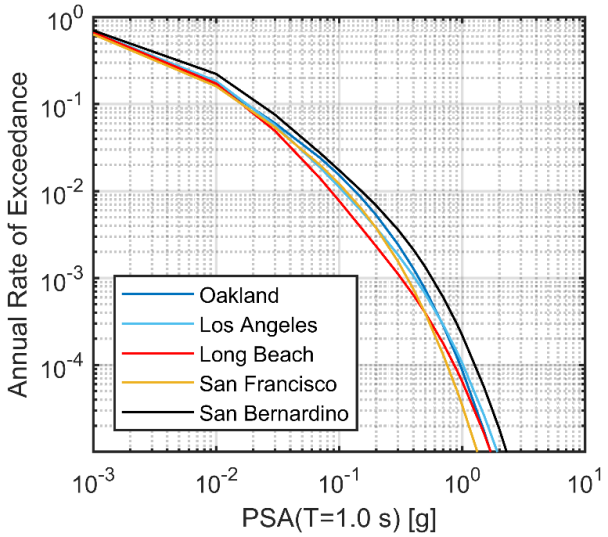

Figure 2. 3. Seismic hazard curves based on elastic PSHA at PSA (T=1.0 s) for five CA sites considered in this study.

Table 2. 2. Target PSA (T=1.0 s) [g] corresponding to each T_R for each site.

Return Period (T_R)	Oakland	Los Angeles	Long Beach	San Francisco	San Bernardino
200 years	0.21	0.17	0.13	0.17	0.24
475 years	0.32	0.28	0.21	0.26	0.40
975 years	0.44	0.41	0.31	0.35	0.56
2475 years	0.62	0.61	0.50	0.50	0.81
5000 years	0.78	0.80	0.67	0.62	1.03

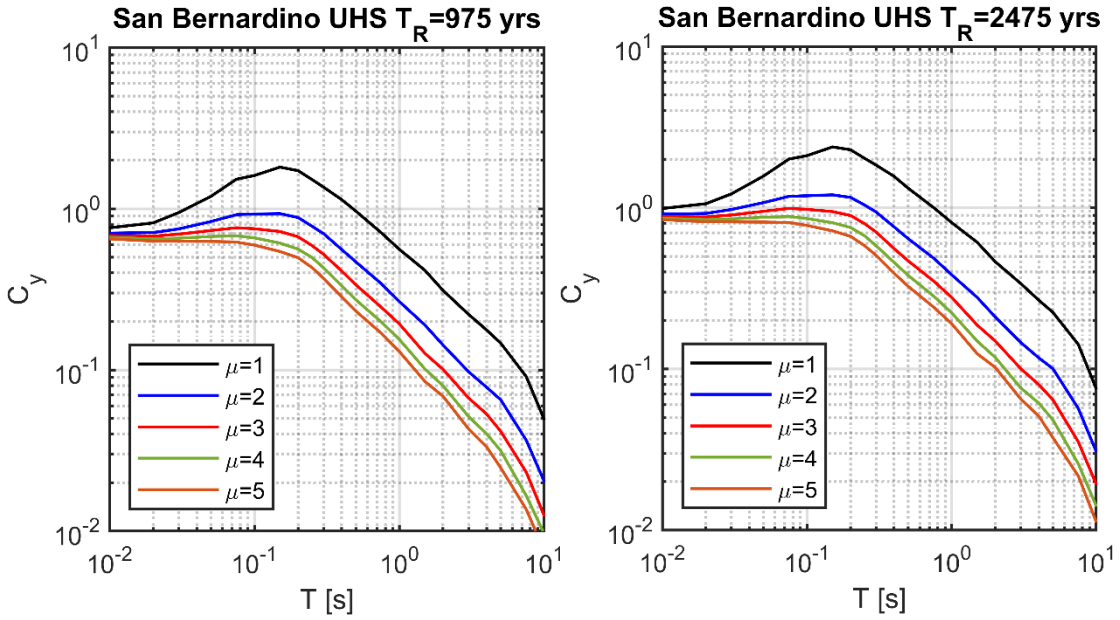

Figure 2. 4. UHS of inelastic C_y for various μ levels at two T_R levels for San Bernardino.

2.2 GROUND MOTION SELECTION AND SCALING APPROACHES

The study involves the utilization of a subset containing 7,203 ground motions from the NGA-West2 database. These motions were employed in the analysis of inelastic SDOF oscillator responses (Bahrampouri, et al., 2023) and utilized in the development of NGA-West2 CB14 GMM. In this database, the records having closest rupture distances (R_{rup}) larger than 80 km were excluded. Further information about the database can be found in Mazzoni et al. (2023). The magnitude (**M**) and R_{rup} values from disaggregation of the UHS varied with T_R levels, ranging from **M** 6.5 to M 8.0 and 0 to 20 km, respectively. This information is important for further constraining the database. The selected ground motions to be used for the structural analysis covered a magnitude range of **M** 5.5 to M 7.9 and R_{rup} range of 0 to 40 km, with no restrictions on the site classes. The maximum scale factor applied to the records was limited to 5.

The linear-scaling approaches employed in this study aimed to achieve compatibility between the desired target mean and the variance of the spectra at each IM level within the period range of 0.4 sec to 4.0 sec. Multiple target spectra were utilized for different return periods. The target record-to-record variability was considered as half of the aleatory standard deviation (or sigma) of the CB14 GMM. By linear scaling of the records, the peaks and troughs of the ground motions were preserved across the specified period range.

The first approach can be considered as a traditional approach, in which the ground motions were scaled to have an average spectrum compatible with the target UHS or CMS derived from *elastic* PSHA. Here, this approach was referred to as the elastic PSHA-based GMSS approach. The second approach, called the inelastic PSHA-based GMSS approach, scaled the ground

motions to align with multiple target spectra that reflect varying ductility levels (i.e., constant-ductility inelastic spectra), which were derived from the inelastic PSHA. The inelastic PSHA-based GMSS approach involves using the Kullback-Leibler Divergence (KLD) criterion (Kullback and Leibler 1951, Bahrampouri et al. 2023) as a cost function for ground motion selection based on a target spectrum. The KLD criterion measures the information lost when approximating one distribution with another. The cost function aims to minimize the mismatch in means and standard deviations between the target and scaled ground motions. This approach offers advantages over conventional methods by avoiding subjective weighting, normalizing the mean mismatch by the standard deviation of the target, and improving handling of standard deviation mismatch. The ground motion selection process utilizes the greedy search algorithm, starting with ground motions that best match the target mean and iteratively adding or substituting ground motions based on the cost function until the desired suite size is achieved. Detailed information on this approach can be found in Bahrampouri et al. (2023).

Sets of 25 individual components of the ground motion were selected and scaled. The ground-motion selection process involved two stages. Initially, 20 ground motions were scaled using the RotD50 component. Subsequently, among two horizontal components, the components that best matched with the target spectrum were selected for NRHA of the bridge model in the transverse direction. Out of the 25 records, a subset of five pulse records was explicitly selected based on their pulse periods (T_p), covering a range from 0.5 seconds to 2.0 seconds (Shahi and Baker 2014). In this case, the sum of squared errors (SSE) approach was utilized to select and scale the pulse records. The SSE was computed by comparing the natural logarithmic spectral acceleration at period T_i of the ground motion with the elastic target spectrum. The ground motion with the smallest SSE was chosen for further analysis. It is important to note that there was no distinction between pulse and non-pulse records when selecting the subsets of 20 ground motions. After analyzing the selected records for different sites at various T_R levels, it was observed that subsets with T_R values less than 2475 years generally contained only a few records with pulses (1 to 4). However, as the T_R value reached or exceeded 2475 years, the number of pulse records in these subsets showed a notable increase, ranging from 3 to 10. The results showed that the sites with high seismicity (e.g., San Bernardino and Oakland) had more pulse-records, and their T_p values were typically greater than $3T_1$.

The Los Angeles site was selected to present and discuss typical results in the body of this report. The target PSA (T=1.0 s) listed in Table 2.2 showed that the PSA values for this site were in between the low values for Long Beach and the high values of San Bernardino. Figure 2.5 compares the spectra of the suite mean and standard deviation with the targets, The figure presents both elastic and inelastic UHS with different ductility levels at T_R=975 years for Los Angeles. The right panel shows the mismatches between mean and standard deviation, which were calculated by taking the difference between the suite mean (or standard deviation) and the target mean (or standard deviation) in natural log units. Figure 2.6 illustrates the comparisons based on inelastic

PSHA-based GMSS approach. In Figures 2.7 and 2.8, comparisons are presented for the cases utilizing the CMS, where the conditioning period was 1.0 s.

The results indicated that, for UHS cases, both GMSS approaches yielded a reasonable fit to the *elastic target spectrum*. However, the elastic PSHA-based ground motions did not align well with the target inelastic spectra at different ductility levels. They tended to overestimate the target mean and not accurately capture the target standard deviation. On the contrary, the inelastic PSHA-based ground motions demonstrated a remarkable agreement with both the target mean and standard deviation across multiple response spectra. For CMS cases, the elastic PSHA-based GMSS approach tended to slightly underestimate the target mean of inelastic response spectrum at high ductility levels and poorly captured the target standard deviation over the specified period range. The inelastic-based GMSS for CMS resulted in a very good compatibility on the mean and standard deviation targets. The selection results for the other sites demonstrated that depending on the target hazard level and the constraints imposed during the ground motion selection and scaling process (e.g., number of records, target period range, distance range, etc.), the elastic PSHA-based GMSS approach yielded comparable or overestimated results compared to the inelastic PSHA-based GMSS approach. The inelastic PSHA-based GMSS approach performed well for all target spectra. Comparisons between the spectra of the suite mean and standard deviation with the targets for elastic and inelastic PSHA-based GMSS approaches for each site, each return period, and each target spectrum are presented in Appendix A.

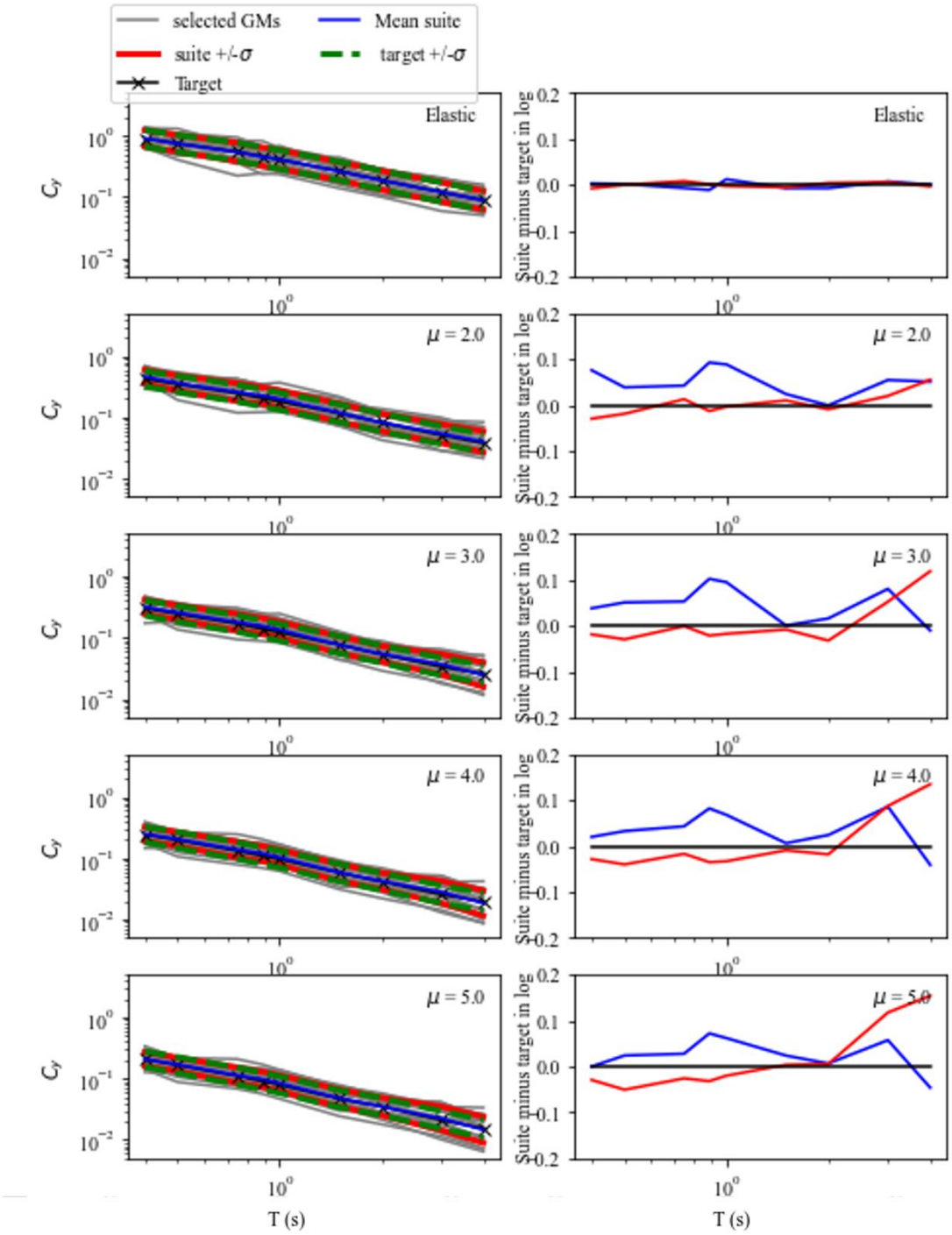

Figure 2. 5. Comparisons of the spectra of the suite mean and standard deviation with the targets for elastic and inelastic **UHS** representing different ductility levels, at T_R=975 years, for Los Angeles, using **elastic** PSHA-based GMSS approach.

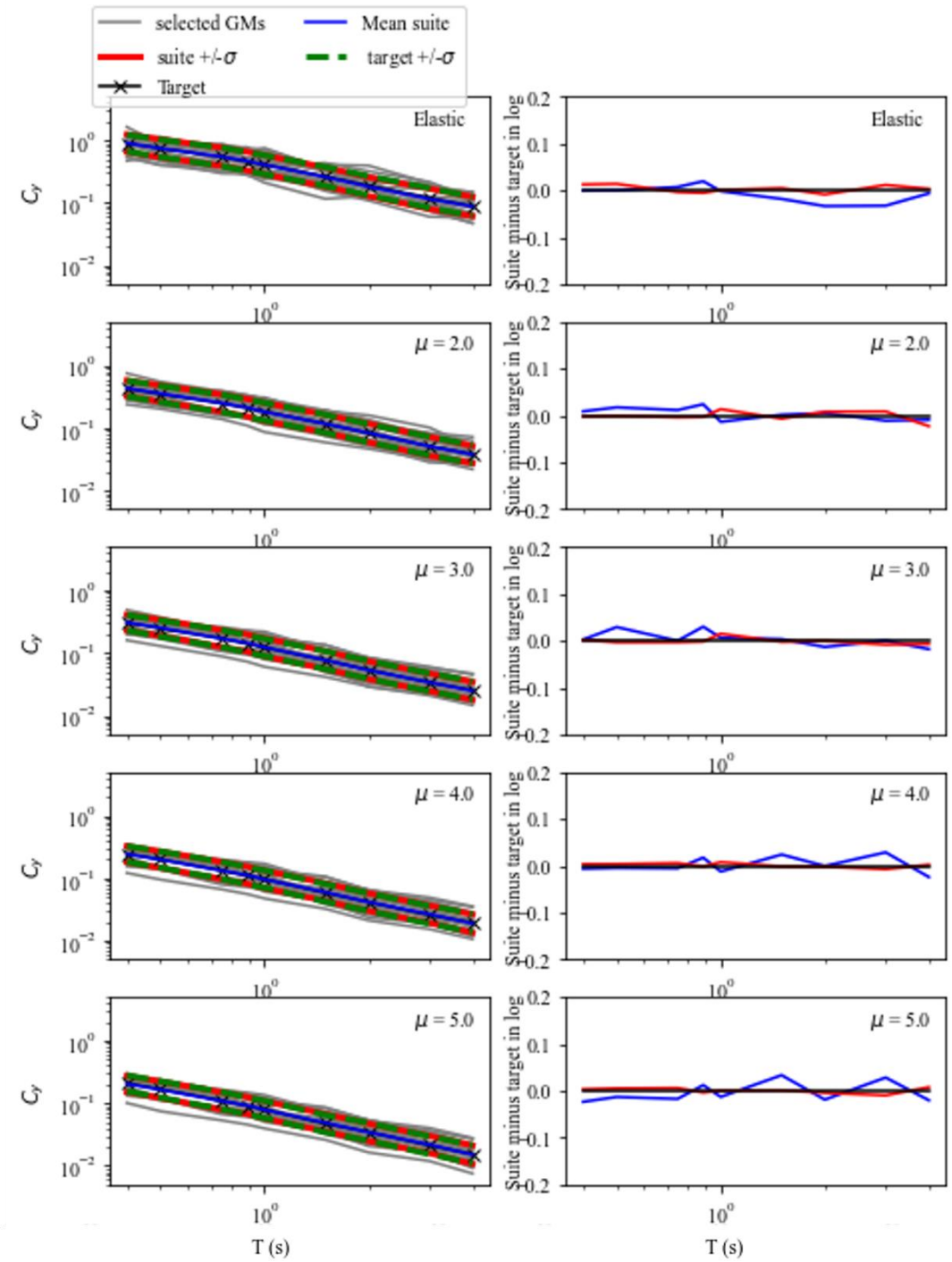

Figure 2. 6. Comparisons of the spectra of the suite mean and standard deviation with the targets for elastic and inelastic **UHS** representing different ductility levels, at T_R=975 years, for Los Angeles, using **inelastic** PSHA-based GMSS approach.

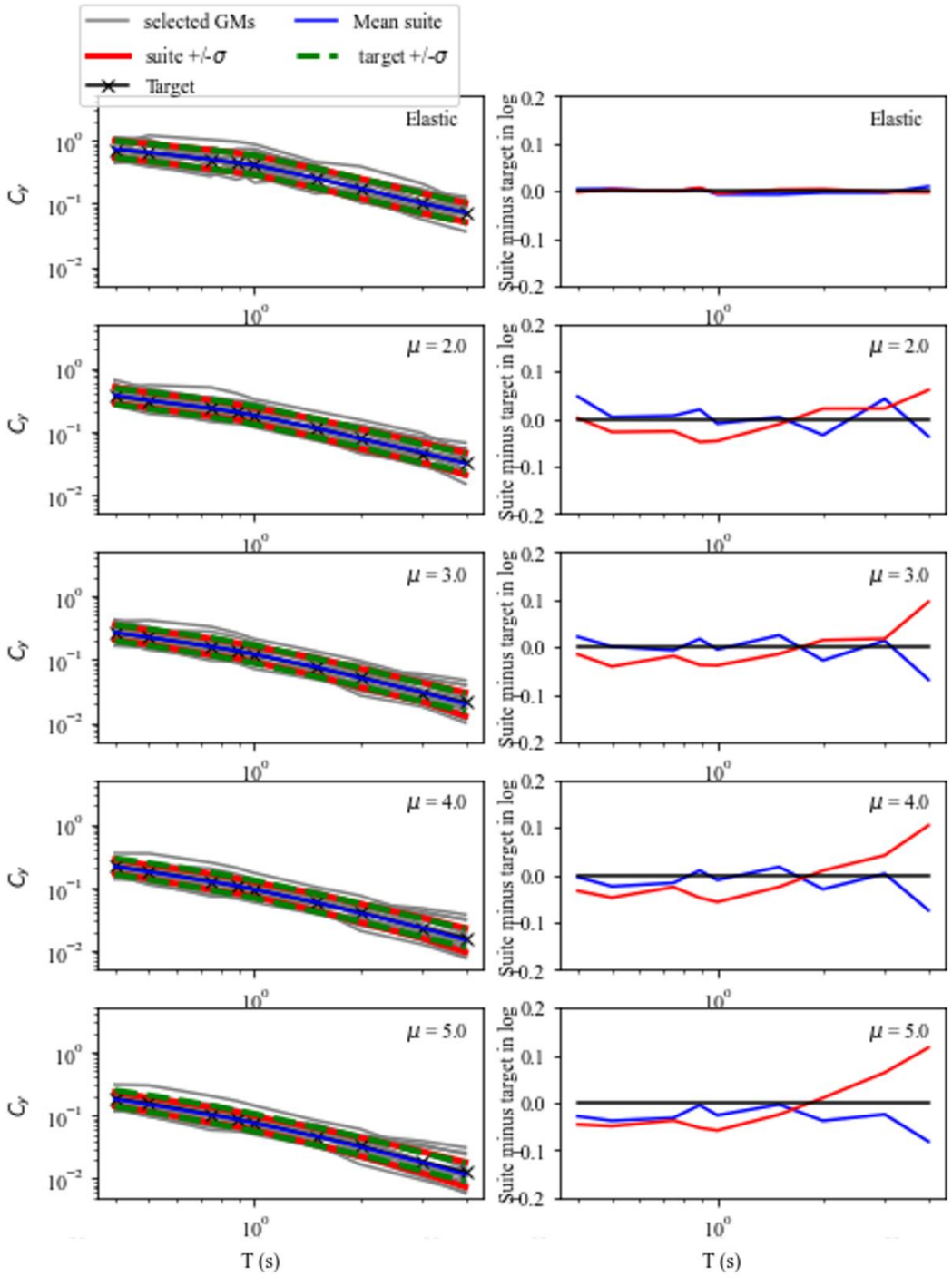

Figure 2. 7. Comparisons of the spectra of the suite mean and standard deviation with the targets for elastic and inelastic **CMS** representing different ductility levels, at T_R=975 years, for Los Angeles, using **elastic** PSHA-based GMSS approach.

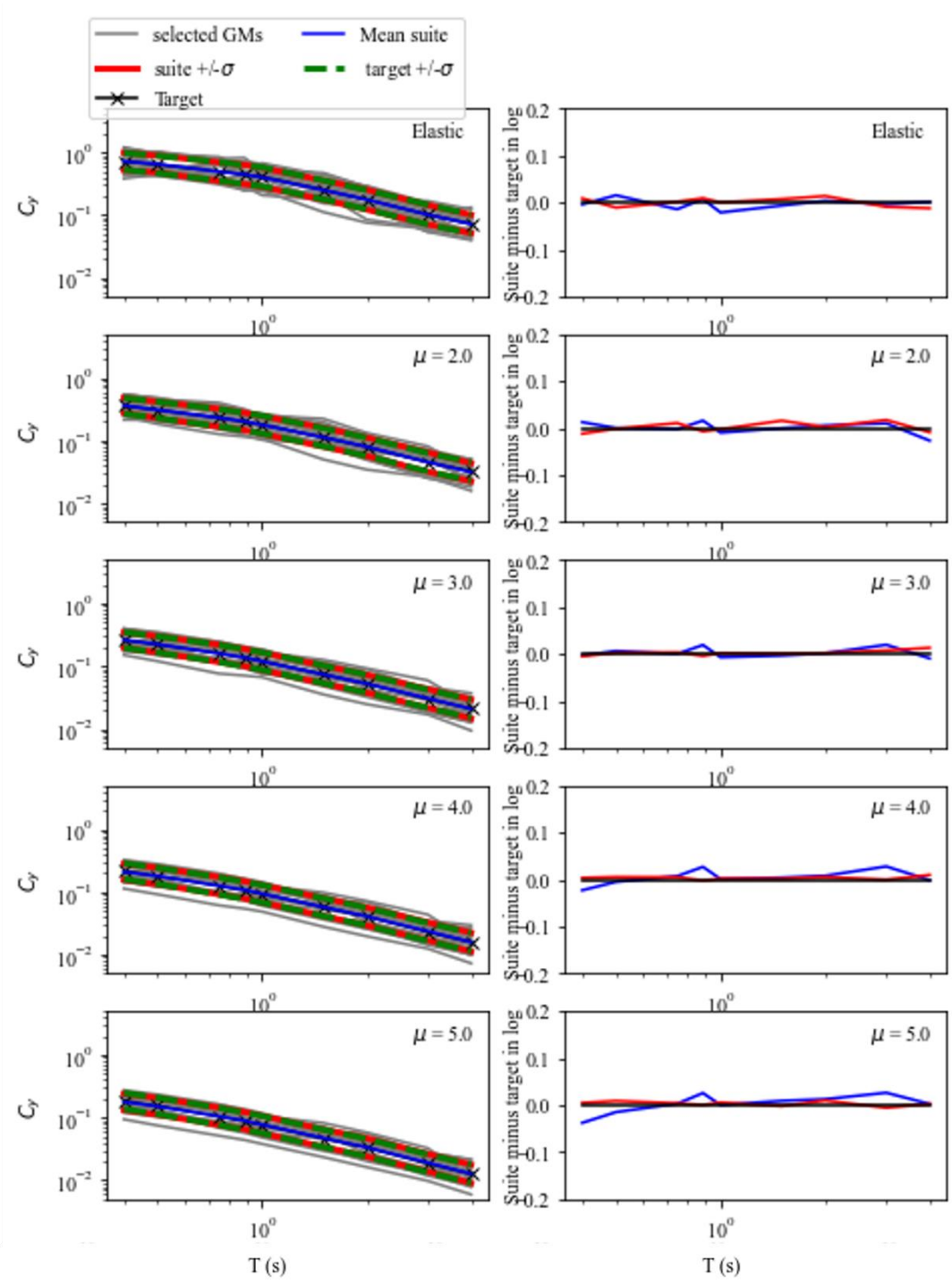

Figure 2. 8. Comparisons of the spectra of the suite mean and standard deviation with the targets for elastic and inelastic **CMS** representing different ductility levels, at T_R=975 years, for Los Angeles, using **inelastic** PSHA-based GMSS approach.

2.3 THREE-SPAN BRIDGE INFORMATION

A modified version of the three-span, three-column bent, the Arroyo de la Laguna bridge that was designed according to the Caltrans Seismic Design Criteria (SDC 2019) was employed. The structural drawings were supplied by Caltrans. The bridge comprises of three spans, with the side spans measuring 90 ft and the middle span measuring 130 ft. The bridge superstructure consists of six California Wide Flange girders (CA WF60) with a combined width of 64 ft. The piers in the original bridge consist of three columns with a diameter of 60" and are connected to 24" diameter Cast-in-Drilled-Hole (CIDH) piles. The bridge abutment is skewed at an angle of 40° and features a seat-type abutment supported by 30" diameter CIDH piles. The bridge utilizes methods and details for Accelerated Bridge Construction (ABC). Several simplifying modeling assumptions were made in this study. The structure was assumed to be cast-in-place with integral bent caps. The skew angle was assumed to be zero, as the study of the impact of skew angle on the study of GMSS approaches for bridges is beyond the scope of this research. The columns boundary conditions were assumed as two-way hinges that allow for unrestrained rotational movement in two principal directions acting as "pins." "Pin" details are commonly used at the column bases of many California bridges to reduce the foundation cost.

Figure 2.9 provides an elevation view of the draft version of the Arroyo de la Laguna Bridge and Figure 2.10 illustrates the superstructure cross section of the bridge. Figure 2.11 shows the elevation and plan views of the modified bridge model, along with the column, hinge, and girder cross sections of the modified bridge model used in this study. The column height in the bridge model was adjusted to achieve a cracked section transverse period of 1.0 sec. Table 2.3 lists the structural properties of the modified three-span bridge.

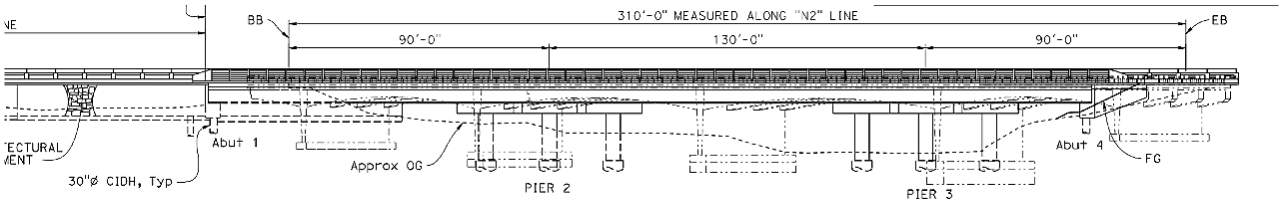

Figure 2. 9. Elevation view of draft version of Arroyo de la Laguna Bridge (Preliminary structural drawings by Caltrans)

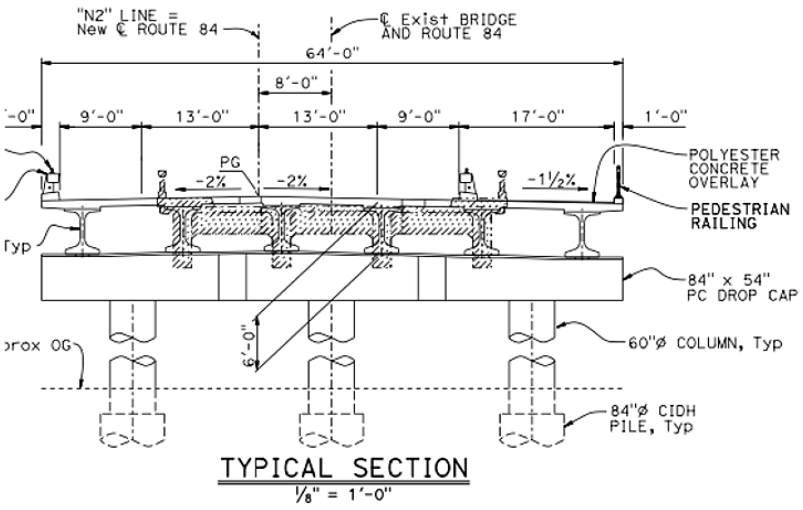

Figure 2. 10. Elevation view of the draft version of the bridge (Preliminary structural drawings by Caltrans)

(a)

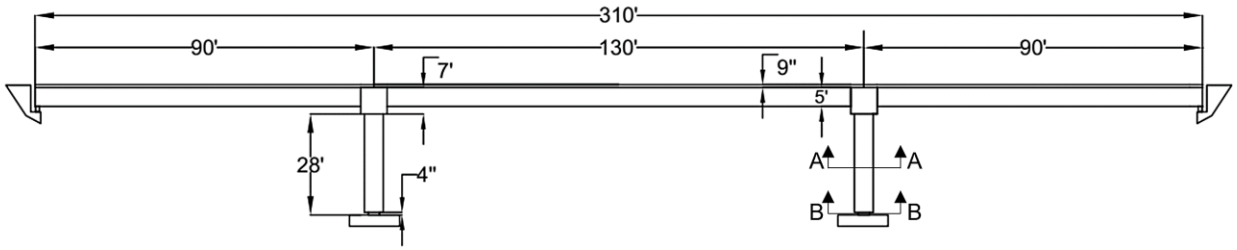

(b)

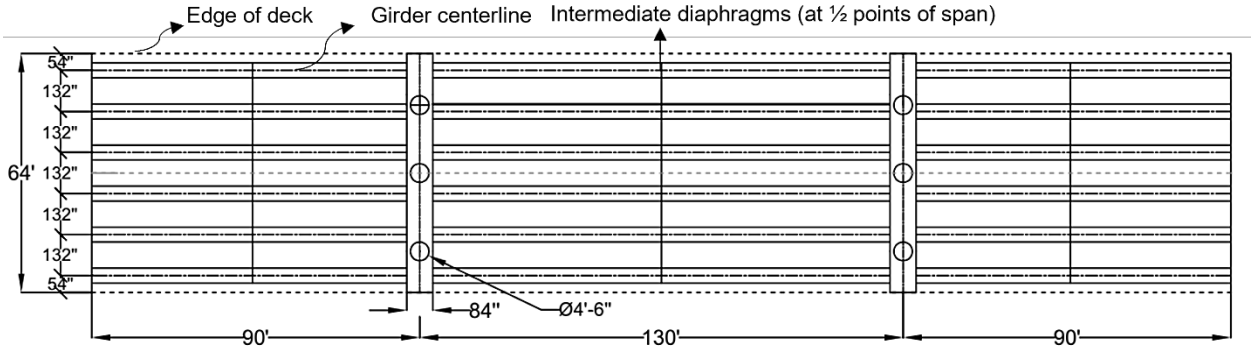

(c)

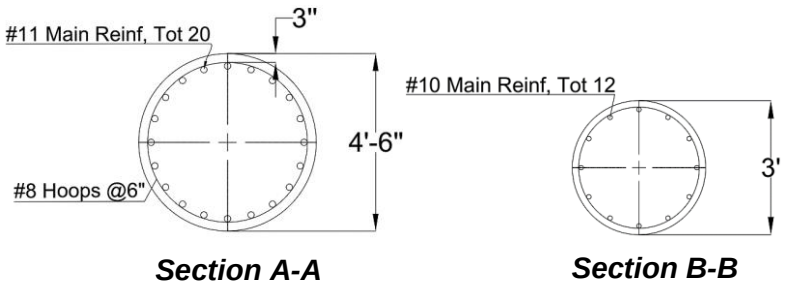

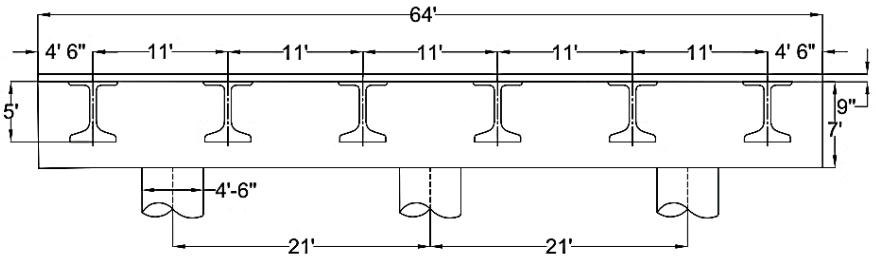

Figure 2. 11. (a) Elevation view of the bridge model (b) Plan view of the bridge model (c) Cross sections of the column, hinge, and girder.

Table 2. 3. Structural properties of the bridge model

Property	Description
Number of spans	3
Length of spans	90 ft, 130 ft, and 90 ft
Total length of bridge	310 ft
Skew angle	0°
Total width of deck	64 ft
Deck	Total Area=64ft *310ft, thickness=9 in
Girder (Area, moment of inertia about local axes, torsional constant)	A= 963.2 in^2, I_x=478505 in^4, I_y=89786 in^4, J=28148 in^4
Column	Diameter=54 in, A=2290.2 in^2, $I_x=I_y$=834785.6 in^4, J_{col} =417392.8 in^4 (polar moment of inertia) Height= 28 ft
Column reinforcement	Longitudinal reinforcement: #11 (total 20), Transverse reinforcement: #8 @ 6 in, Longitudinal reinforcement ratio: 1.4%
Axial Load Index (ALI)	0.076
Precast cap-beam	84"x84"
Abutment type	Seat-type

2.4 THREE-DIMENSIONAL BRIDGE MODEL

To accurately capture the nonlinear behavior of the bridge, a comprehensive three-dimensional (3D) model of the bridge was developed using the OpenSees software (Mazzoni et al. 2006, Mc Kenna et al. 2010). This software allows for the implementation of various material models and element types, enabling realistic representation of the nonlinear structural response of bridges. Based on the Caltrans SDC (2019), Ordinary Standard Bridges (OSB) follow the "strong beam-weak column" principle, allowing for plastic hinge mechanisms in Seismic Critical Members (SCMs) such as columns and Type I-II shafts. However, there are ductility limits for individual columns and global ductility levels that must be met. Sacrificial elements, on the other hand, are designed to absorb and dissipate energy up to moderate level seismic events but fail afterward thus protecting the more critical components of the bridge. They are typically easier and less costly to repair or replace compared to other elements such as piles and foundation. Earthquake-resisting elements, such as shear keys, provide longitudinal and transverse resistance under service loads. These elements help maintain the integrity of the bridge structure during seismic events. The bridge decks, girders, and cap beams are classified as capacity-protected (CP) members. This designation implies that these members are designed to remain elastic even when adjacent members experience plastic deformation.

To simulate the nonlinear responses of columns, the fiber-section Euler-Bernoulli force-based beam-column elements with distributed plasticity *(forceBeamColumn*) were employed. These elements consider the interaction between axial force and bending moment at the section level. The element flexibility matrices and deformations were evaluated numerically at five Gauss-Lobatto integration points distributed along the length of the column (Neuenhofer and Filippou 1998, Scott and Hamutçuoğlu 2008).

In this study, different stress-strain relationships for fiber sections, including unconfined concrete (cover), confined concrete (core), and reinforcing steel were considered. Figure 2.12 illustrates the stress-strain curves for the Concrete02 (Yassin 1994) and Steel02 (Menegotto and Pinto 1973) uniaxial material models employed in the study. Table 2.4 presents the constitutive model properties for unconfined and confined concrete materials. The theoretical stress-strain relationship developed by Mander et al. (1988) was utilized to estimate the properties of confined concrete in the column, disregarding the tensile strength of the concrete. The parameters to define the stress-strain behavior of Steel02, listed in Table 2.5. The Steel02 material model accounts for the Bauschinger effect. However, this material model does not consider cyclic strength and stiffness degradation resulting from factors such as bar buckling and fatigue. To account for torsional deformation in the column fiber section, torsional stiffness was assigned to the backbone curve. This torsional stiffness was determined by the equation 0.2 x G_{conc} x J_{col}, where G_{conc} represents the shear modulus of concrete and J_{col} represents the polar moment of inertia. It is important to note that the torsional stiffness was reduced by 80% to account for the cracking of the column cross-section (Aviram et al. 2008, Shoushtari et al. 2021). The P-delta effect was considered in the bridge model to account for the interaction between axial loads and lateral deflection. Note that the consideration of secondary moments induced by the P-delta effect provides a more accurate representation of the structural response.

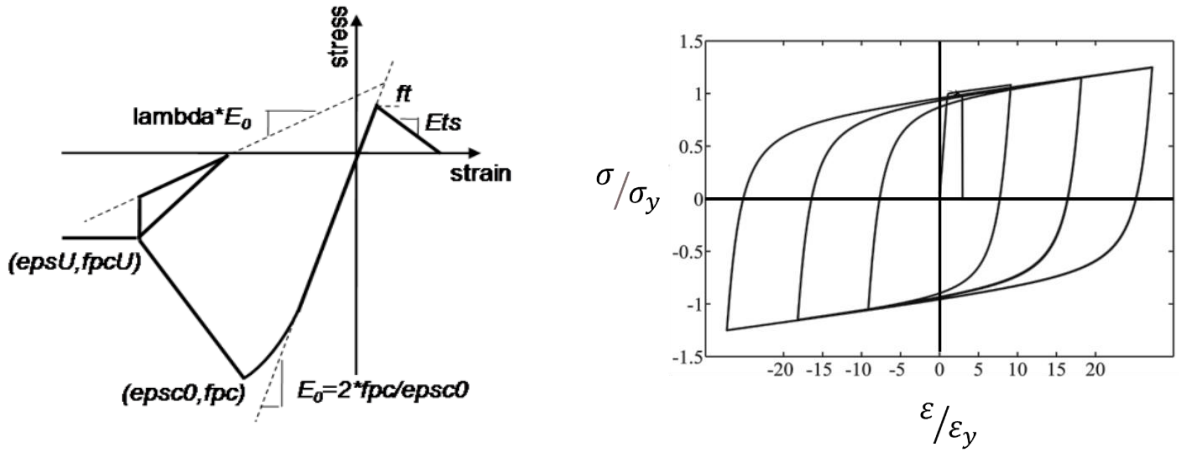

Figure 2. 12. Stress-strain relationship for concrete and reinforcing steel (Steel02).

Table 2. 4. Constitutive model properties for concrete material

Model parameters	Unconfined concrete	Confined concrete
fpc, compressive strength at 28 days (ksi)	3.60 (expected fce=4.68ksi)	5.36
epsc0, concrete strain at maximum strength	0.002	0.0069
fpcU, concrete crushing strength (ksi)	0.72	4.84
epscU, concrete strain at crushing strength	0.004	0.018

Table 2. 5. Constitutive model properties for Steel02 material

Model parameters	Input value
f_{ye}, yield strength (ksi)	68
E_s, initial elastic tangent (ksi)	29000
Strain hardening ratio (b)	0.01
R_0, parameters to control transition from elastic to plastic branches	18.5

The superstructure of the bridge was modeled using elastic beam-column elements (*elasticBeamColumn*). The input parameters for these elements included the cross-sectional area, elastic modulus, shear modulus, moment of inertia about local axes, and torsional constant. To model the bridge superstructure, the grillage-beam technique was utilized, chosen for its simplicity and accuracy in comparison to more complex 3D finite element shell and beam models. This technique represents the superstructure as a series of longitudinally and transversely connected beams. The torsional constants of the deck beam elements were reduced by a factor of 0.5. The Poisson's ratio of the grillage beams was set to zero, assuming no interaction between axial force

and bending moment in the perpendicular directions. To incorporate cracking effects, the deck and girder elements were assigned 40% of their sectional rigidity. Additionally, rigid connections (*rigidLink beams*) were established among the girder, cap beam, and deck elements to ensure structural continuity. In the grillage model, each bridge span was divided into multiple elements, allowing for an even distribution of the lumped mass of the deck along the entire span. The masses of the girder and cap beam were also distributed along their respective lengths. At each end of the deck, a roller support was defined to simulate the behavior of a seat-type abutment after shear-key failure. Figure 2.13 depicts the 3D bridge model extracted from the OpenSees program.

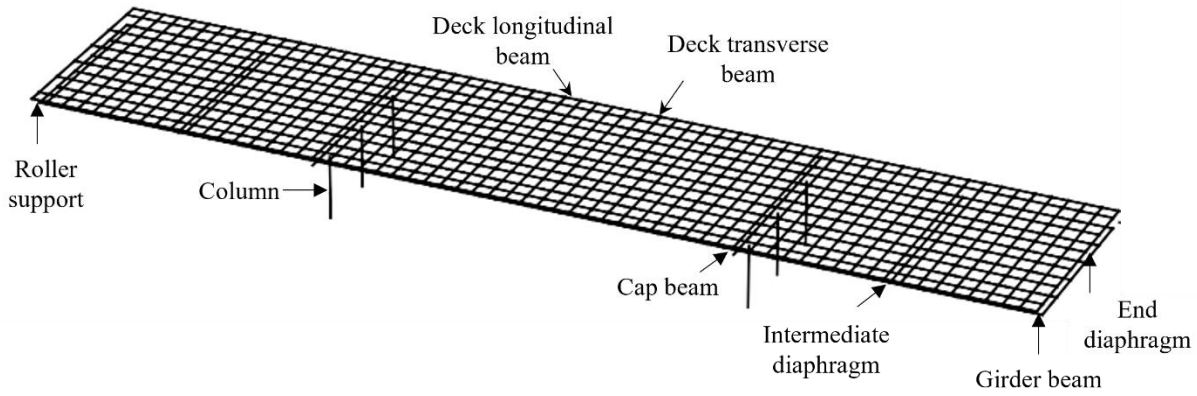

Figure 2. 13. 3D view of the bridge model extracted from the OpenSees program.

2.5 MOMENT-CURVATURE ANALYSIS

Moment-curvature ($M-\phi$) analysis is a widely used method in structural engineering to evaluate the nonlinear behavior of reinforced-concrete sections, which provides valuable insights into its flexural capacity and curvature ductility. This information is used to determine the pushover behavior of reinforced concrete columns. Caltrans incorporates $M-\phi$ analysis as a part of their design and assessment procedures for bridges and other concrete structures. This analysis allows engineers to assess the strength and ductility of the bridge elements, helping them make informed decisions about design modifications, reinforcement detailing, and structural performance. Bridges must have sufficient plastic hinge ductility and energy dissipation capacity to handle Design Seismic Hazards (DSH) or the SEE. When the DSH for life safety occurs, OSBs may experience significant damage but must avoid collapse.

Caltrans specifies global displacement criteria for the frames or the piers in the OSB and Recovery Standard Bridge. In that regard, displacement capacity must be greater than the displacement demand imposed on the bridge during a seismic event. This can be expressed as:

$$\Delta_C \geq \Delta_D \tag{2.1}$$

where Δ_C for columns can be determined through idealized $M-\phi$ analysis, using the following equations:

$$\Delta_C = \Delta_Y^{col} + \Delta_P \tag{2.2}$$

in which Δ_Y^{col} represents the idealized effective yield displacement of the column, and Δ_P represents the idealized plastic deformation capacity due to rotation of the plastic hinge, which are given by

$$\Delta_Y^{col} = \frac{L^2}{3} \times \phi_Y \tag{2.3}$$

$$\Delta_P = \theta_P (L - \frac{1}{2} L_P) \tag{2.4}$$

where $L =$ distance from the point of maximum moment to the point of contra-flexure; $\phi_Y =$ idealized yield curvature defined by an elasto-plastic representation of the cross section $M-\phi$ curve; $\theta_P =$ plastic rotation capacity ($\theta_P = L_P \phi_P$) with ϕ_P denoting the idealized plastic curvature capacity ($\phi_P = \phi_u - \phi_y$); and ϕ_u=curvature capacity at the failure limit state. Additionally, L_P stands for the equivalent analytical plastic hinge length given by

$$L_P = 0.08L + 0.15 f_{ye} d_{bl} \geq 0.3 f_{ye} d_{bl} \tag{2.5}$$

where f_{ye} = expected yield strength for ASTM A706 reinforcement (ksi); d_{bl} = nominal bar diameter of longitudinal column reinforcement (in.).

Seismic deformation demands in structures encompass displacements, rotations, curvatures, or strain during seismic events. Displacement ductility and curvature ductility are essential measures of inelastic response, with the former representing overall structural behavior and the latter focusing on local section response. The displacement ductility capacity of a critical member can be defined as:

$$\mu_{c=\frac{\Delta_c}{\Delta_Y^{col}}} \tag{2.6}$$

Figure 2.14 illustrates the local displacement capacity of a typical cantilever column with fixed based.

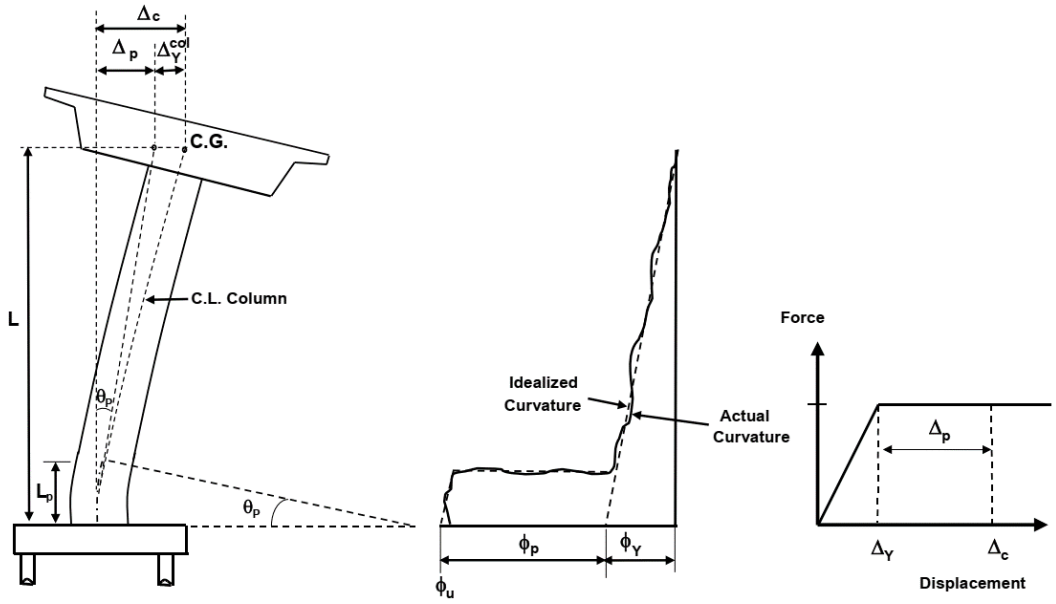

Figure 2. 14. Local displacement ductility capacity of a typical cantilever column with fixed based (SDC, 2019).

A moment-curvature analysis was conducted using the OpenSees program. In $M - \phi$ analysis of the column section, the following considerations were made:

- The axial load on the column section was calculated using one-half of the column self-weight and the tributary weight of the superstructure.
- The plastic moment capacity of ductile concrete elements was computed based on expected material properties specified in Caltrans SDC (2019).
- The actual curve was idealized using an elasto-plastic response, achieved by balancing the areas between the actual and idealized curves, as shown in Figure 2.15.

The analysis results showed that the column in the bridge model had a displacement ductility capacity of 5.01. The displacement ductility capacity of the three-span bridge, on the other hand, was determined based on pushover analysis of the bridge, which is discussed in the subsequent section.

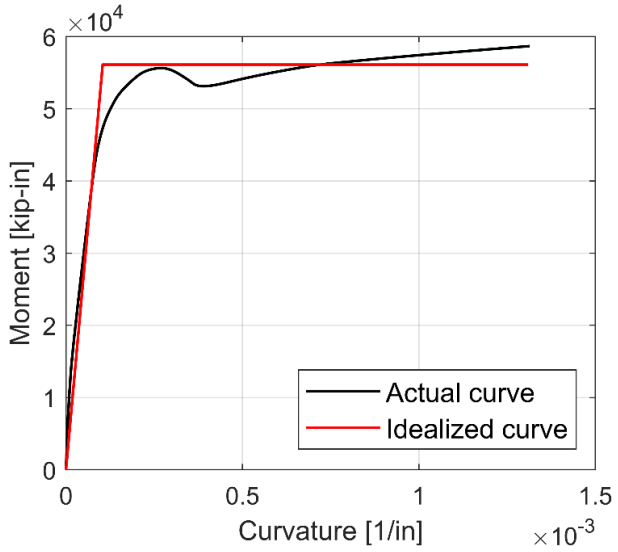

Figure 2. 15. Actual and idealized $M - \phi$ diagrams

2.6 MODAL ANALYSIS

Modal analyses revealed that the first mode of the bridge corresponded to a rotational mode with a period of 1.31 seconds. The second and third modes represented transverse and longitudinal modes, both with a period of 1.0 second. The fourth mode corresponded to symmetric-bending modes with a period of 0.18 seconds. Table 2.6 lists the modal periods and frequencies for the three-span bridge model. Figure 2.16 shows the mode shapes of the 3D bridge model. In the case of damping model, mass proportional and the last committed stiffness proportional Rayleigh damping was applied. A critical-damping ratio of 5% was applied at two modes such as 1st and 3rd modes of the bridge model. Importantly, it should be emphasized that the distributed plasticity model exhibited low sensitivity to the choice of damping model, and the Rayleigh damping model demonstrated its effectiveness in producing satisfactory results (Chopra and McKenna 2016).

Table 2. 6. Modal periods and frequencies obtained from the three-span bridge model.

Mode	T (s)	Frequency (Hz)
1	1.31	0.76
2	1.0	1.0
3	1.0	1.0
4	0.18	5.56

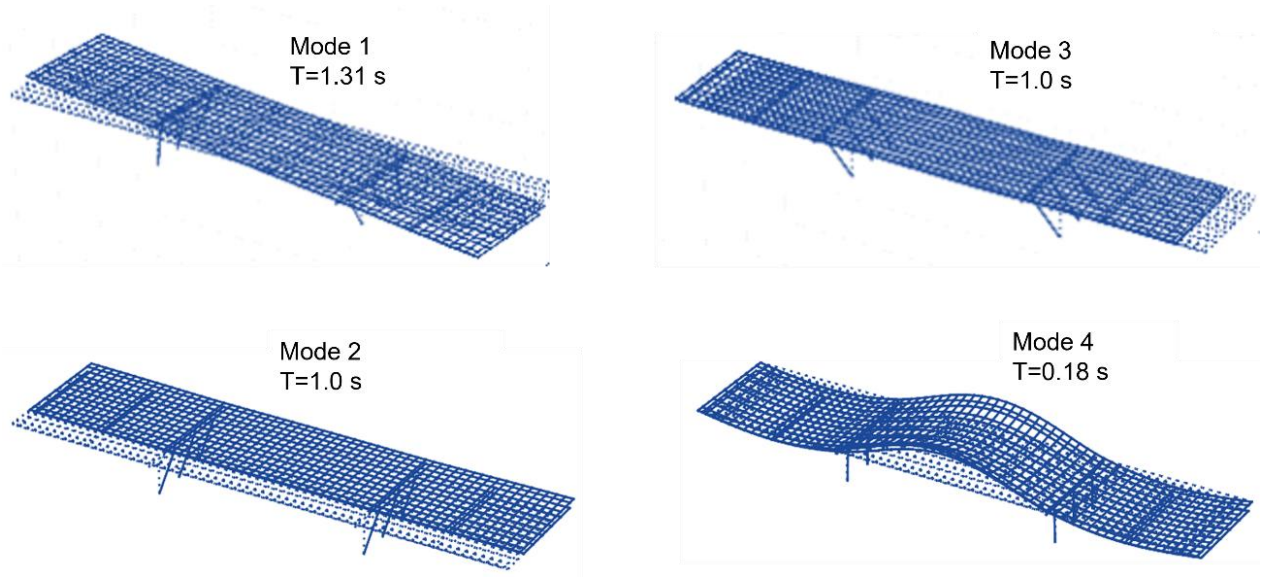

Figure 2. 16. The first four mode shapes of the bridge model.

2.7 PUSHOVER ANALYSIS

A displacement-controlled pushover analysis for the bridge model was performed in the transverse direction. Reference loads were applied at the center of the pier caps, incrementally pushing the bridge to a target displacement level, set at 10% of the total column height (i.e., drift ratio of 10%). The P-delta effects were included in the analysis. Figure 2.17 illustrates the pushover analysis results in the transverse direction. The total base shear of the bridge structure was calculated by summing the base shears for each column obtained in the pushover analysis. The pushover curve was idealized by a bilinear relationship using the equal-area approximation. The idealized pushover curve of the bridge is also plotted in Figure 2.17. The ultimate displacement of the bridge was defined as the point at which the base shear forces decrease to 85 percent of their peak values. Using the idealized pushover curve, the bridge's yield displacement was found as 3.1 inches, and the ultimate displacement as 31.2 inches. The displacement ductility capacity of the bridge structure was quantified by taking the ratio of ultimate displacement to yield displacement, resulting in a value of 10.0. The column drift ratio at failure was 9.3%.

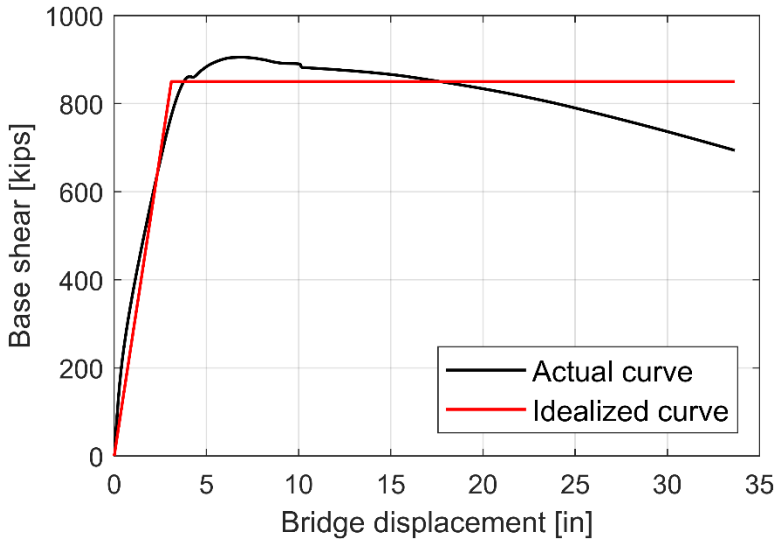

Figure 2. 17. The actual and idealized pushover curves of the bridge in the transverse direction.

3 Seismic Performance and Risk Assessment of Bridge Structures

This chapter investigates the impact of elastic and inelastic PSHA-based GMSS approaches on engineering demand parameters (EDPs) for a three-span bridge model. It includes comparative studies on the distribution of structural responses at two specified T_R levels, i.e., T_R=975 years and 2475 years, an investigation of effects of pulses on residual drift ratios, and comparisons of elastic and inelastic analyses methods (to assess the accuracy of "equal displacement rule"). This chapter also discusses the influences of GMSS approaches on damage states, fragility curves, and risk curves of the three-span bridge model.

3.1 NONLINEAR STRUCTURAL RESPONSES AT SPECIFIED SEISMIC HAZARD LEVELS

The selected and scaled ground motions were applied in the transverse direction of the bridge. The bridge symmetric design and equal stiffness of the bents resulted in nearly zero in-plane rotation, which was estimated by taking the ratio of the difference in abutment displacements at both ends (obtained from NRHA) to the bridge length. The negligible in-plane rotation indicated that the rotational mode of the bridge (i.e., first mode) was not activated. The structural response parameters considered in this study were column drift ratio (CDR), transverse displacement ductility demand (μ_D), and residual drift ratio (RDR). The CDR was computed by taking the ratio of the maximum absolute transverse displacement at the top of the column to the column height. The μ_D was determined by the calculating the ratio between the maximum absolute displacement at the top of the column and yield displacement of the bridge obtained from the static pushover analysis. The RDR was computed by dividing the bridge's final permanent transverse displacement by column height. To ensure that the bridge model has come to a complete stop, five seconds of zero-accelerations were added to the end of all acceleration time series.

Figures 3.1-3.5 depict the cumulative distribution functions (CDFs) of CDR, μ_D, and RDR obtained from elastic PSHA-based and inelastic PSHA-based GMSS approaches at T_R =975 years

and T_R =2475 years for the five sites. CDF gives the probability of a random variable being less than or equal to a particular value. For sites characterized by relatively high seismicity, such as Oakland, Los Angeles, and San Bernardino, the use of elastic PSHA-based UHS ground motions led to mean values of approximately 10% higher, or comparable, for CDR and μ_D values in comparison to the inelastic PSHA-based ground motions at T_R=975 years. For sites with relatively lower seismicity like Long Beach and San Francisco, both GMSS approaches yielded similar mean values. At T_R=2475 years, the mean CDR and μ_D values obtained from both approaches exhibited reasonable similarity, indicating that the overestimation by elastic PSHA-based ground motions did not significantly impact the results. Nevertheless, for the site characterized by the highest seismicity, namely San Bernardino, the inelastic PSHA-based GMSS approach demonstrated greater efficiency in reducing the dispersion in structural responses, thereby preventing conservative estimates of seismic demand.

The CMS-based ground motions selected by different GMSS approaches showed comparable mean CDR, and also μ_D, values for both return periods. This could be attributed to the good agreement between the mean spectra of elastic PSHA-based ground motions and the target inelastic spectra at different ductility levels for the selected T_R levels. It should be noted, however, that in Los Angeles and San Francisco, the inelastic spectra of the records, when scaled using the elastic-PSHA based GMSS approach, exceeded the target CMS inelastic spectra for return periods both greater than and lower than 975 years (see Appendix A). These differences led to conservative fragilities using the elastic-PSHA based GMSS approach compared to the inelastic-PSHA based GMSS approach, as discussed in the subsequent section.

The CMS-based ground motions tended to generate lower mean values compared to UHS-based ground motions, especially at higher seismic hazard levels (e.g., T_R =2475 years). This is expected as the UHS does not represent a single scenario earthquake and it includes higher spectral acceleration values, which in turn, leads to conservative estimates of the mean responses. Additionally, it was observed that the dispersion levels in structural response tended to increase with higher T_R levels for UHS-based cases, while CMS-based cases provided more stable estimates of dispersion.

In the case of RDRs, the mean RDR values for most sites, including Oakland, Los Angeles, Long Beach, and San Francisco, remained below 0.2% at T_R =975 years and 2475 years. However, for San Bernardino, the mean RDRs reached approximately 0.21% at T_R =975 years and 0.6% at T_R =2475 years. Although the mean RDRs were below the 1% post-earthquake serviceability limit established by some design codes such as Japan, the large dispersions in RDRs, particularly in the upper tails of the CDF plots, resulted in exceedance of the 1% RDR for sites with high seismicity. Higher dispersions were observed in RDRs compared to CDR and μ_D. Importantly, it was observed that the RDRs were influenced by pulse characteristics of the ground motion.

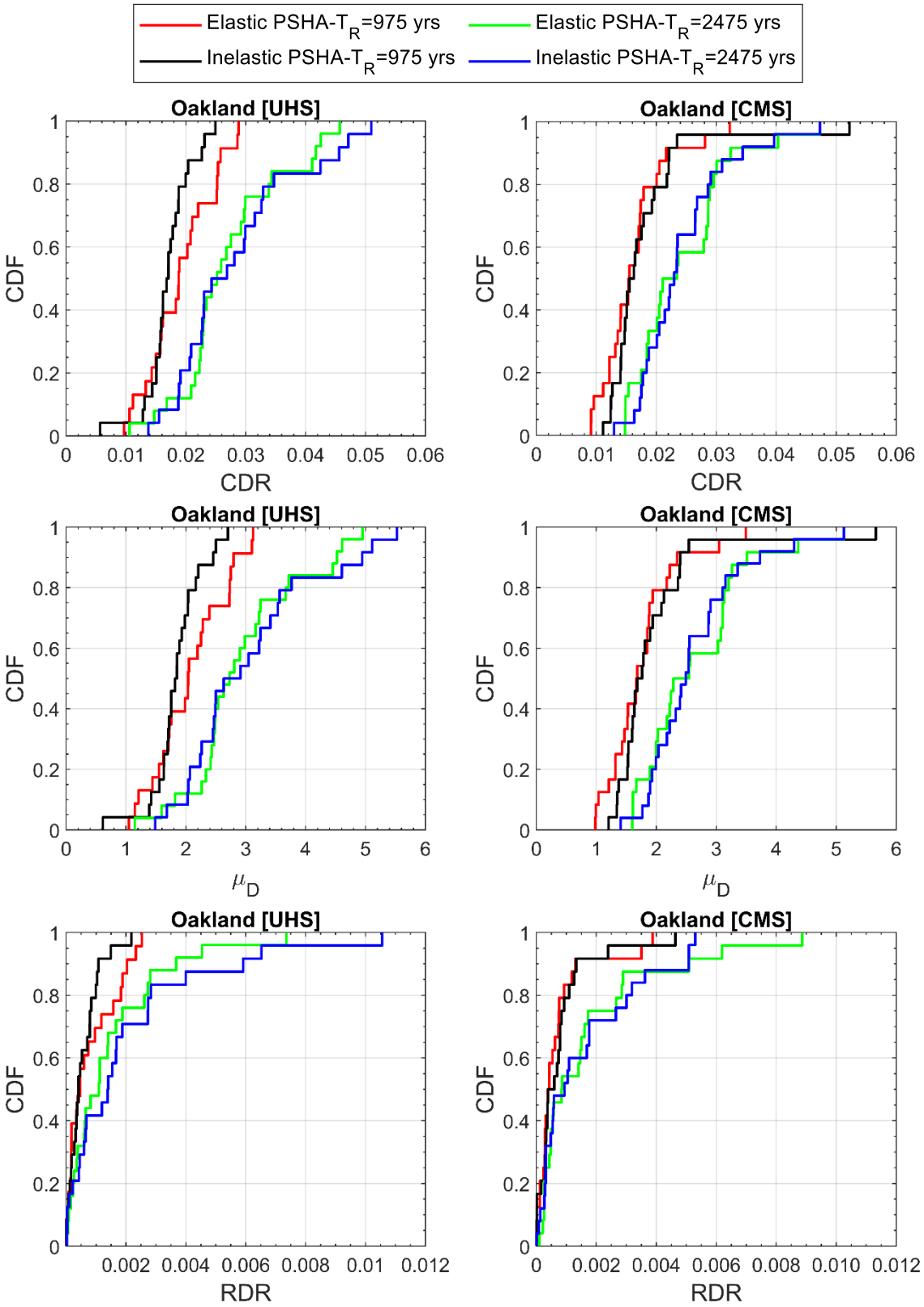

Figure 3. 1. CDFs of CDR, μ_D, and RDR obtained from elastic PSHA and inelastic PSHA-based GMSS approaches at T_R =975 years and T_R =2475 years in Oakland.

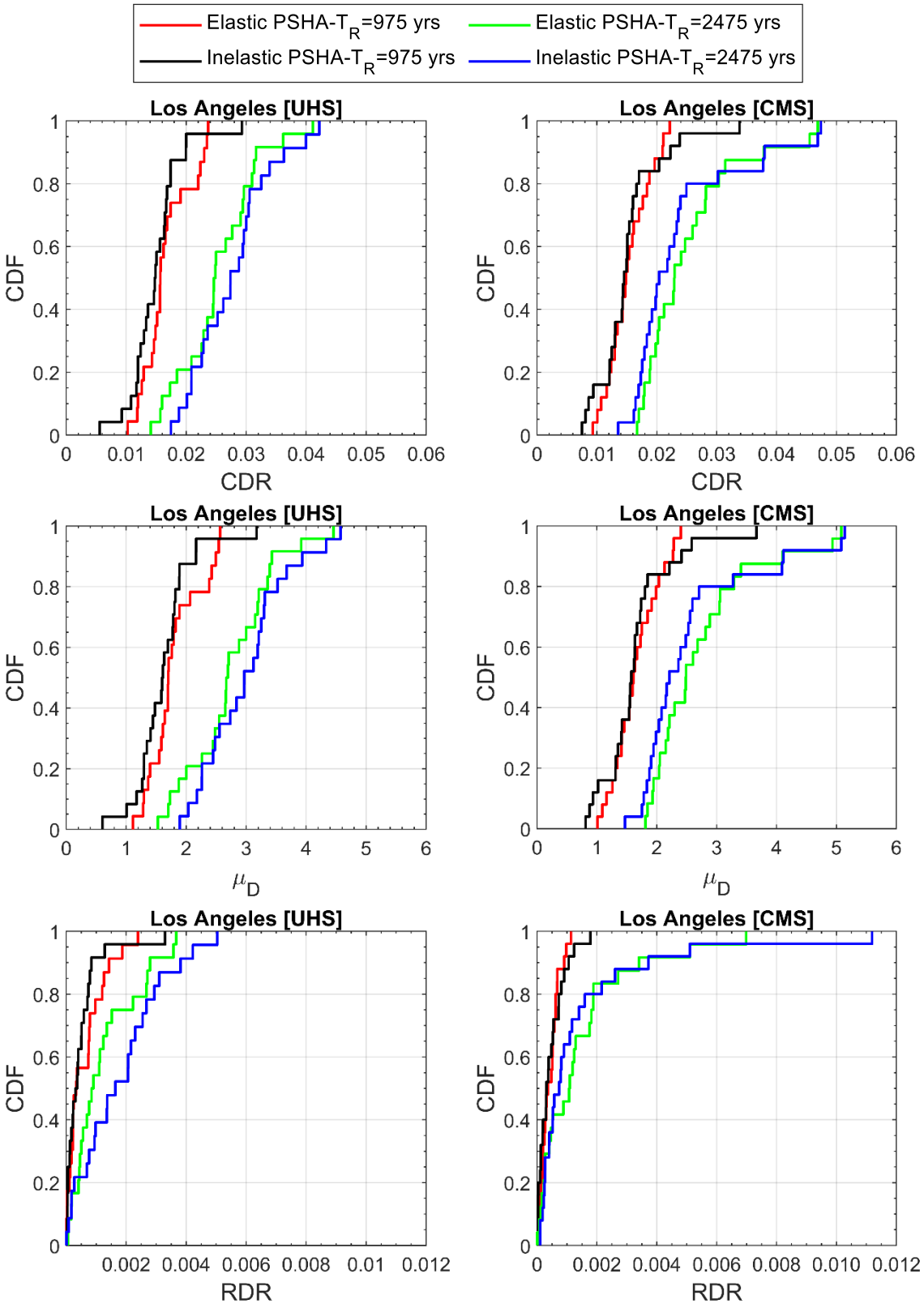

Figure 3. 2. CDFs of CDR, μ_D, and RDR obtained from elastic PSHA and inelastic PSHA-based GMSS approaches at T_R =975 years and T_R =2475 years in Los Angeles.

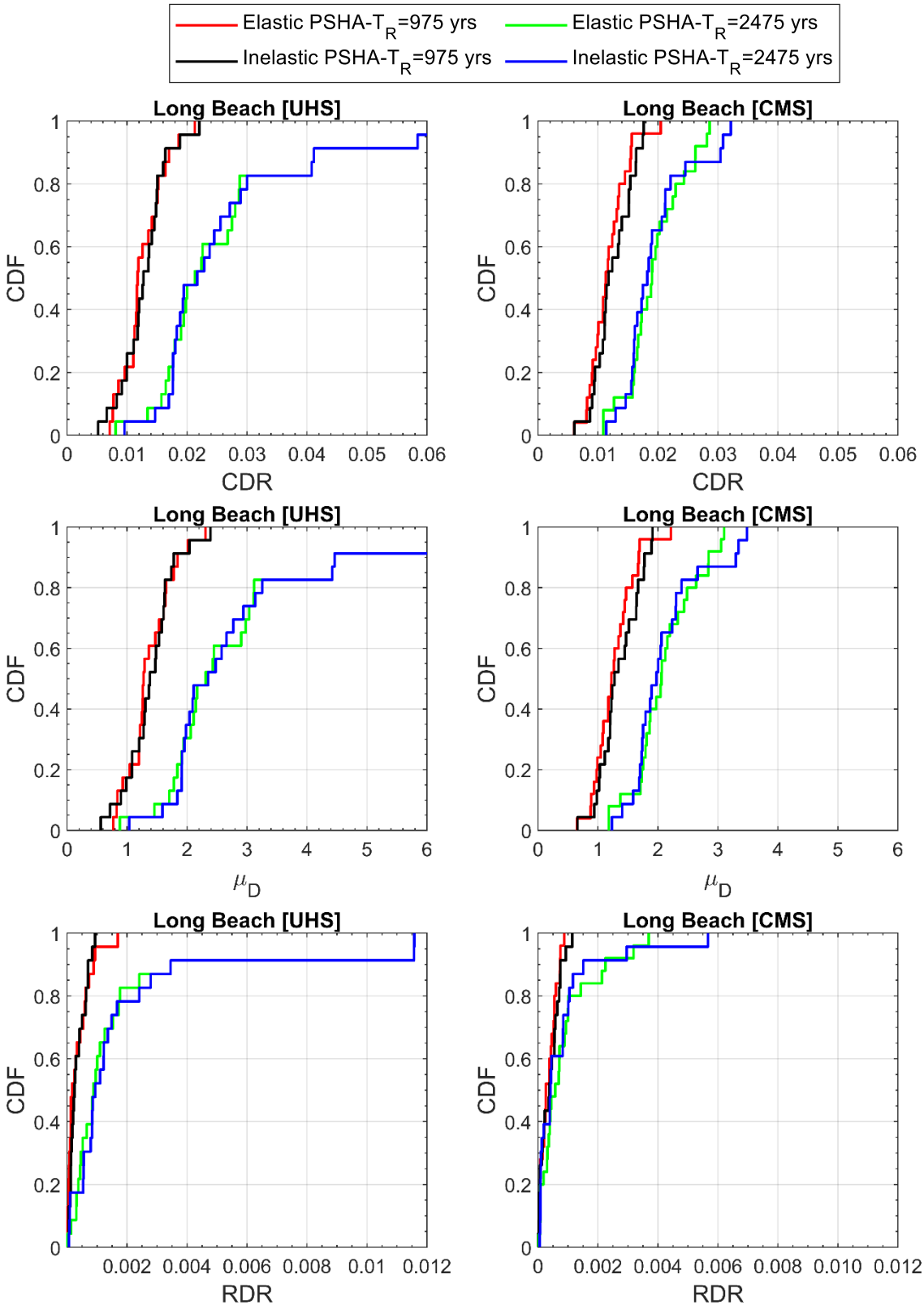

Figure 3. 3. CDFs of CDR, μ_D, and RDR obtained from elastic PSHA and inelastic PSHA-based GMSS approaches at T_R =975 years and T_R =2475 years in Long Beach.

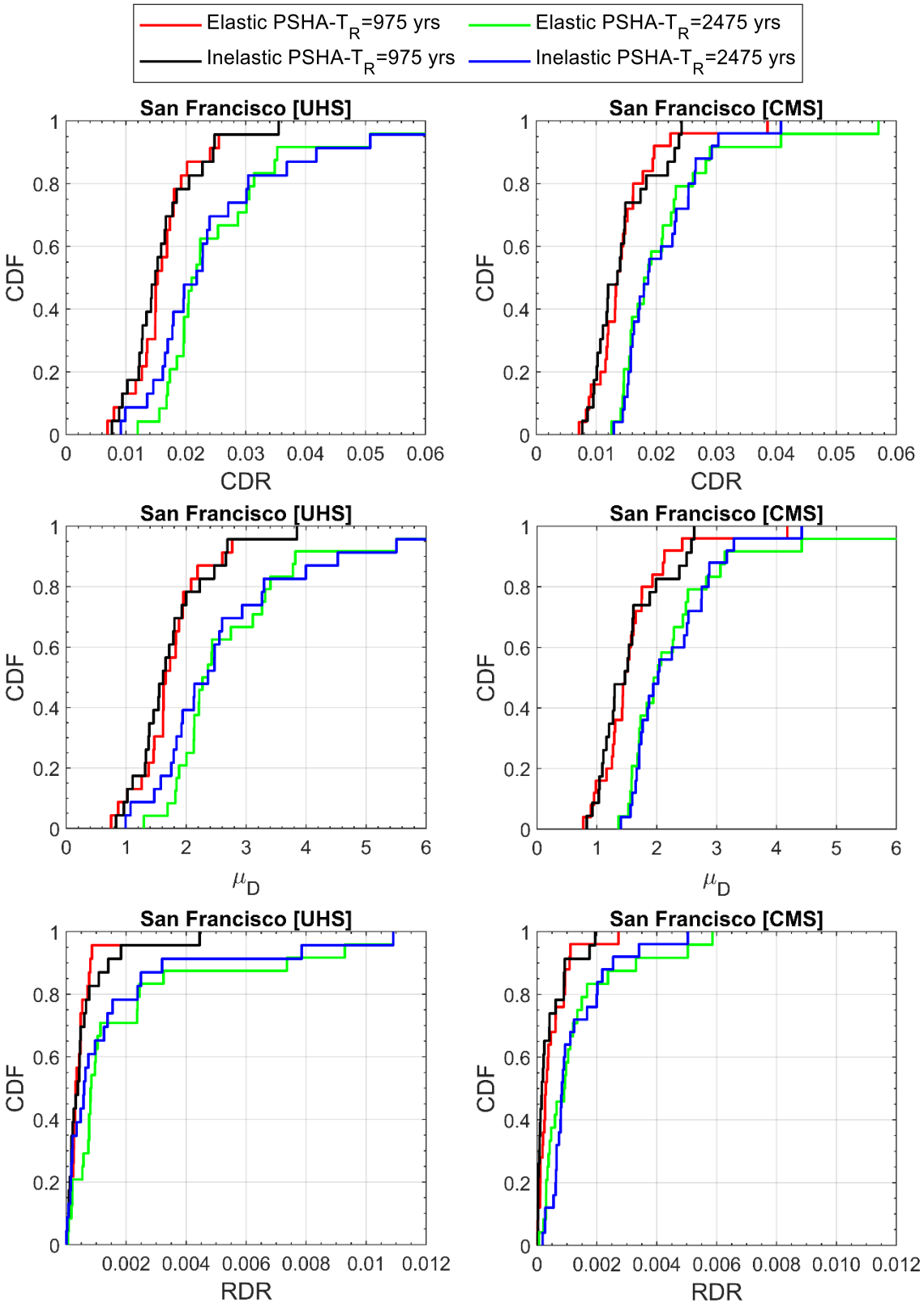

Figure 3. 4. CDFs of CDR, μ_D, and RDR obtained from elastic PSHA and inelastic PSHA-based GMSS approaches at T_R =975 years and T_R =2475 years in San Francisco.

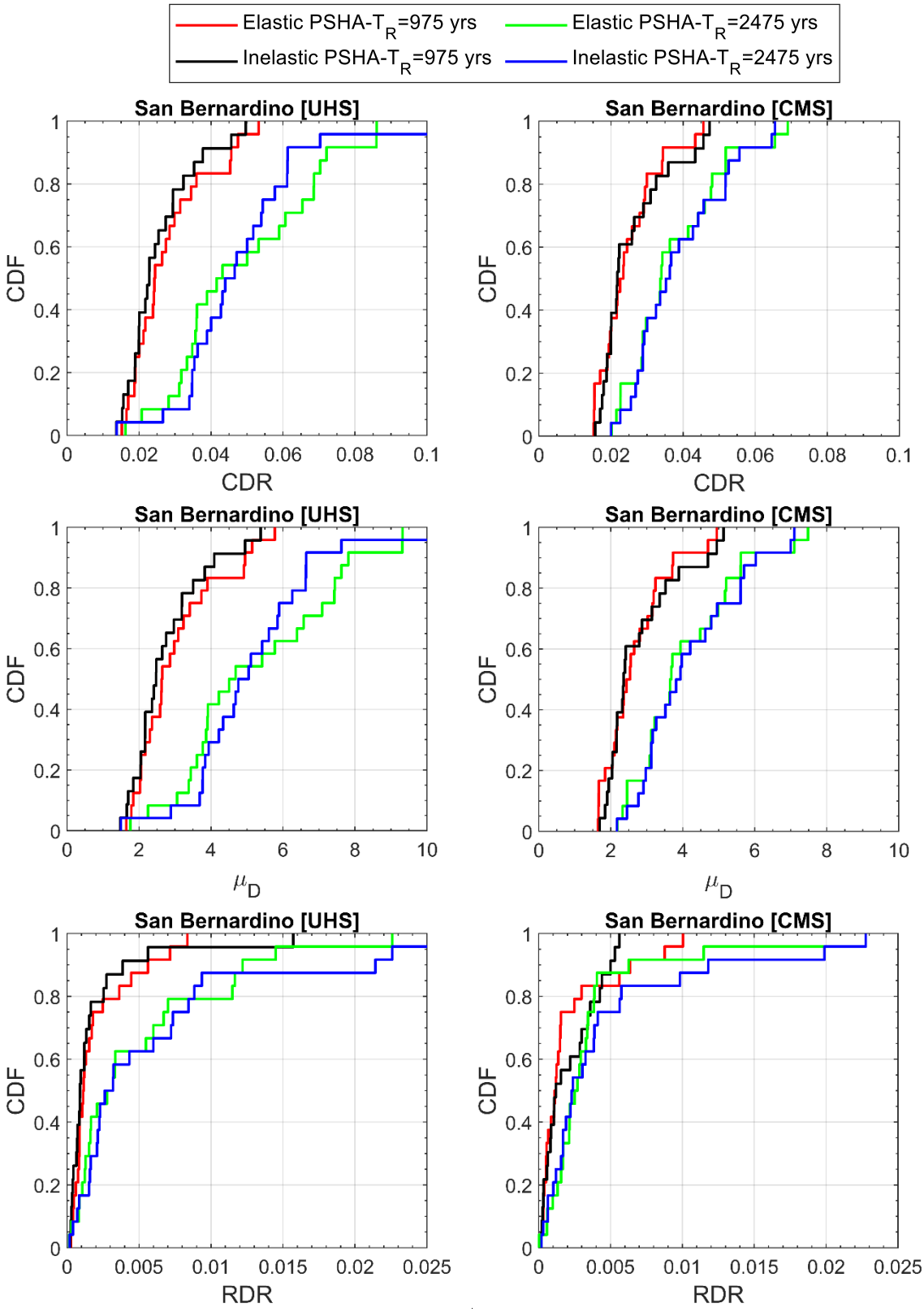

Figure 3. 5. CDFs of CDR, μ_D, and RDR obtained from elastic PSHA and inelastic PSHA-based GMSS approaches at T_R =975 years and T_R =2475 years in San Bernardino.

3.2 SENSITIVITY OF RDR TO PULSE RECORDS

Figure 3.6 illustrates the comparison between pulse period (T_p) and RDR for pulse records obtained from elastic and inelastic PSHA-based GMSS approaches in San Bernardino at T_R=2475 years. The average RDRs obtained from pulse records are also shown on the plots. Here, all pulse-like records within the pool of twenty-five ground motions were being considered. In San Bernardino, the subsets of elastic and inelastic PSHA-based selected ground motions contained more than 10 pulse records, enabling relatively meaningful statistical inferences. It is noteworthy that the UHS-based subsets included a greater number of pulse records compared to the CMS-based subsets. The results suggested that, on average, the pulse records produced higher RDRs than the pooled records (see Figure 3.5). For instance, it was found that pooled RDRs from elastic UHS records were 0.51%, whereas the RDRs for pulses reached 0.63%. Similarly, for inelastic UHS records, the pooled RDRs were 0.62%, while pulses resulted in 0.82%. This observation is also consistent with the shake table test results (Phan et al. 2007, Choi et al. 2010). It was observed that pulses with $T_p > 3T_1$ could generate RDRs higher than 1%, indicating that other ground-motion properties might influence the structural response.

In Figure 3.7, the relationships between the natural logarithms of the CDRs and RDRs are presented, based on pulse records and non-pulse records selected to match UHS using two GMSS approaches for San Bernardino at T_R = 2475 years. The figure also includes linear regression equations fitted to the data points and the coefficient of determination (R^2) values. As seen, there are positive trends between CDR and RDR, indicating that as the CDR increases, the RDR also tends to increase. It was observed that the mean CDRs obtained from pulse records were higher than those from non-pulse records, indicating that the presence of pulse-like ground motions tended to lead to higher CDRs. The higher CDRs and larger R^2 values associated with pulse records indicated that pulses had a significant impact on structural damage and warranted careful consideration in seismic design and assessment. However, it is worth noting that the estimation of the RDR can be sensitive to the material properties, computer models, other characteristic of input motions, and numerical techniques that can introduce additional uncertainty into the analyses results. Further research should be performed against experimental data or well-established benchmarks to investigate the sensitivity of these factors on results.

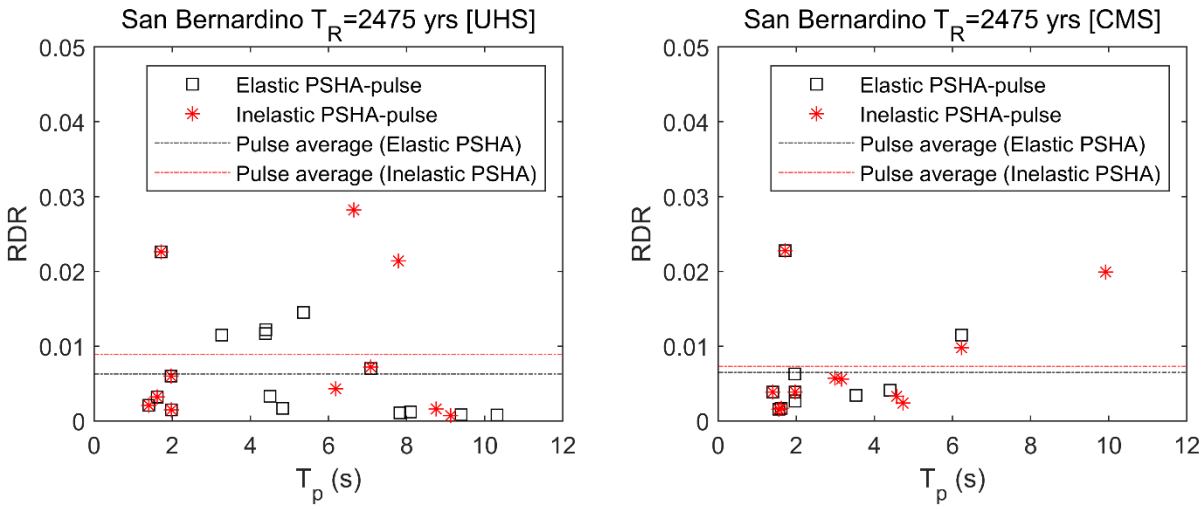

Figure 3. 6. Comparison of pulse period (T_p) and residual drift ratio (RDR) for elastic- and inelastic PSHA-based GMSS approaches in San Bernardino at T_R=2475 years.

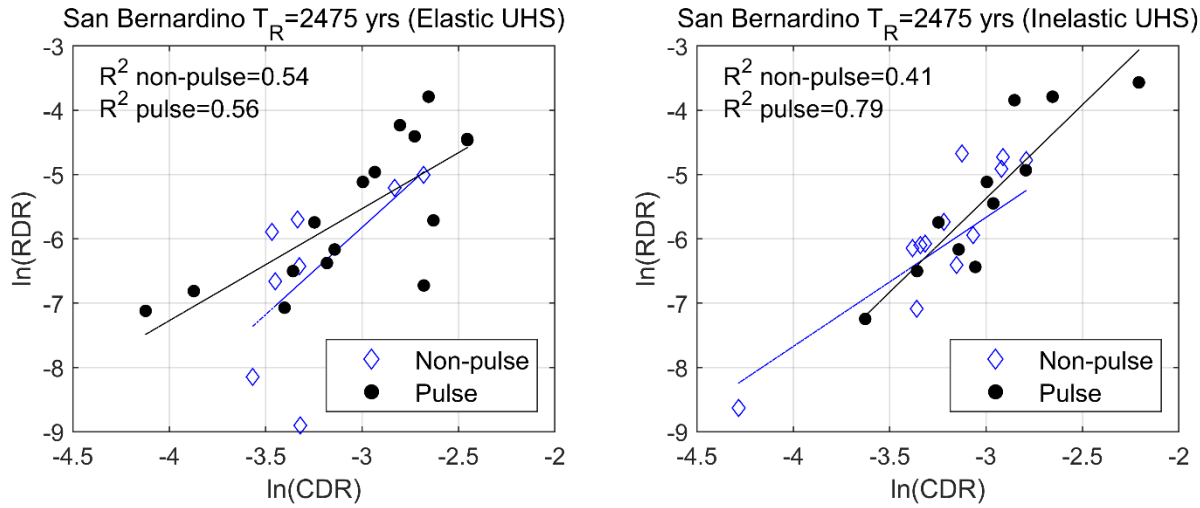

Figure 3. 7. Relationships between natural logarithms of CDRs and RDRs obtained from pulse- and non-pulse- records using elastic and inelastic UHS-based GMSS approaches for San Bernardino at T_R=2475 years.

3.3 COMPARISONS OF ELASTIC AND INELASTIC ANALYSES METHODS

The design methodology for structures varies depending on the importance level and span length of the bridge. Several methods are allowed, including the equivalent static method, elastic methods based on linear spectrum methods, and NRHA. These methods offer a range of options to design bridges with different levels of complexity and accuracy depending on the specific project requirements. This section investigates the validity of the equal displacement approximation rule (Veletsos and Newmark 1960) by comparing the CDRs obtained from different analyses methods:

elastic SDOF analysis, inelastic SDOF analysis, linear response history analysis (LRHA), and NRHA.

In this study, SDOF systems with a bilinear force-displacement relationship corresponding to the bilinear Takeda hysteretic model were analyzed. This behavior includes an initial linear segment defined by the stiffness parameter K, followed by a post-yield segment with a 2% strain hardening effect. A damping ratio of 5% was considered. For inelastic SDOF, we used the C_y values of the 25 scaled ground motions that were scaled to matched to the target inelastic spectrum at a given ductility demand level. The maximum inelastic displacement (u_{max}) was calculated using the following equation:

$$u_{max} = C_y \mu g \left(\frac{T}{2\pi}\right)^2 \tag{3.1}$$

where T is the oscillator period, μ is the ductility level, and g is the acceleration of gravity. Here the μ values were based on observations from NRHA at the specified T_R level. The CDR (indicated in orange) was obtained by dividing the u_{max} by the column height.

To overcome the approximations made in the elastic response spectrum analysis and accurately capture the linear responses of the bridge, LRHA has been employed. This approach involves employing elastic beam-column elements in the OpenSees model to accurately simulate the behavior of the bridge columns.

The findings depicted in Figures 3.8 and 3.9 indicated that the *linear* response of the bridge could be reasonably approximated by an *elastic* SDOF analysis, as evidenced by the similarity in results with linear elastic methods. It is noted that using elastic analyses or inelastic SDOF analysis methods resulted in underestimation of the CDRs in comparison to 3D NRHA (purple bar) for both return periods. Specifically, the CDRs were underestimated by approximately 20% to 40% when the μ_D was approximately 2, as observed in the case of T_R =975 years (see Figures 3.1-3.5). Moreover, the magnitude of this underestimation tended to increase as the ductility demand ratio μ_D increased (e.g., μ_D >2), ranging from 45% to 100% at T_R =2475 years. For high seismicity area, like San Bernardino, and for long T_R, inelastic SDOF system performs slightly better than the elastic SDOF.

These observations suggest that equal displacement assumption can underestimate inelastic displacement, even for some structural periods longer than about 0.5 sec, especially for large earthquake magnitudes and large ductility. This observation is consistent with those of Bozorgnia et al. (2010) and Bahrampouri et al. (2023). Therefore, relying solely on seismic demands obtained from linear elastic methods may lead to potentially unsafe design for bridges in high seismic regions. Implementing a diverse set of analytical methods could significantly enhance the safety of designs in these regions.

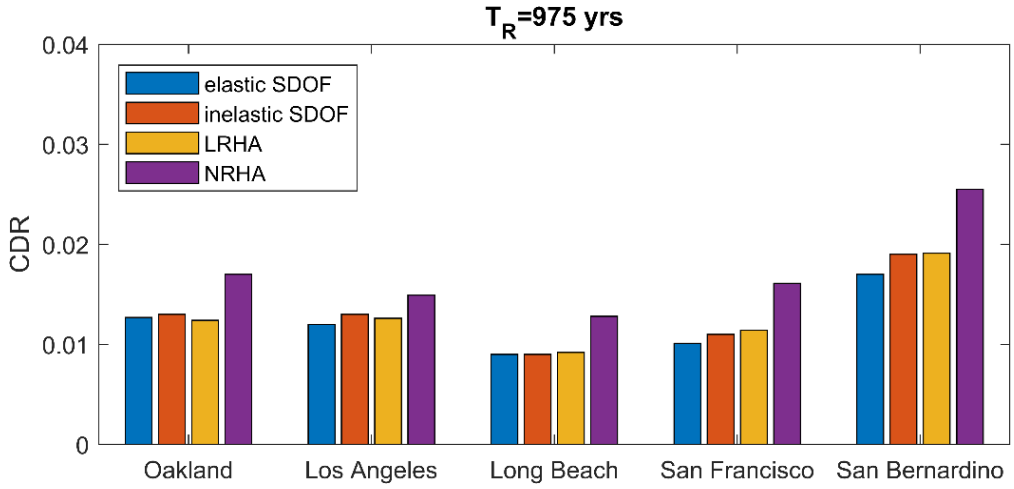

Figure 3. 8. Comparisons of CDRs obtained from elastic SDOF analysis, inelastic SDOF analysis, linear response history analysis (LRHA), and nonlinear response history analysis (NRHA) methods using sets of 25 records obtained from the inelastic PSHA-based GMSS approach at T_R=975 years.

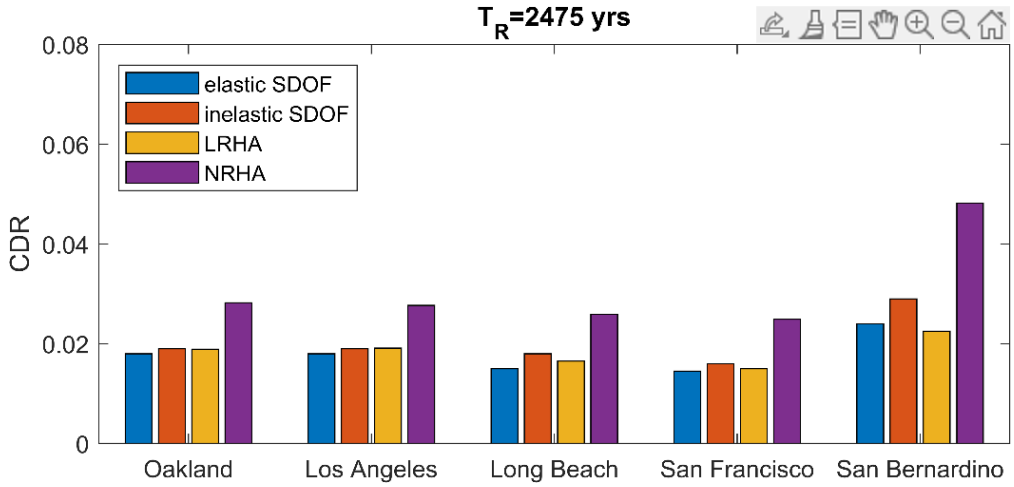

Figure 3. 9. Comparisons of CDRs obtained from elastic SDOF analysis, inelastic SDOF analysis, linear response history analysis (LRHA), and nonlinear response history analysis (NRHA) methods using sets of 25 records obtained from the inelastic PSHA-based GMSS approach at T_R=2475 years.

3.4 PROBABILISTIC SEISMIC ASSESSMENT OF BRIDGE RESPONSES

3.4.1. Damage State Definition

Fragility curves, essential tools in earthquake engineering for assessing structural vulnerability, have been developed through the analysis of various data sources, including experimental, numerical, and field data (Choi et al. 2004, Padgett and DesRoches 2008, Vosooghi and Saiidi

2012). In this study, bridge damage states (DSs) defined by Vosooghi and Saiidi (2012), who developed a probabilistic relationship between experimental damage data and EDP in the form of fragility curves, were employed. The study involved extensive analytical modeling of seismic response for both single column and multicolumn bents. A wide range of variables was considered, including aspect ratio, longitudinal steel ratio, site class, distance to active faults, earthquake return period, and the number of columns per bent. Each column was subjected to analysis under 25 different near-field and far-field ground motions. The study was based on data from 32 bridge column models, primarily tested on shake tables, and resulted in fragility curves for six EDPs corresponding to six distinct damage states (DSs). These DSs ranged from flexural cracks (DS_1) to failure (DS_6). The six EDPs considered were the maximum drift ratio (MDR), RDR, frequency ratio (FR), inelasticity index (II), maximum longitudinal steel strain (MLS), and maximum transverse steel strain (MTS). These damage states were defined based on the severity of damage observed in columns of the bridge. Table 3.1 lists the definitions of all DSs. Figure 3.10 illustrates the possible apparent DSs of bridge column.

Table 3. 1. Definitions of the damage states

DSi	**Definitions**
DS_1	Flexural cracks
DS_2	Minor spalling and possible shear cracks
DS_3	Extensive cracks and spalling
DS_4	Visible lateral and/or longitudinal reinforcing bars; and
DS_5	Compressive failure of the concrete core edge (imminent failure)
DS_6	Failure

Past studies employed various EDPs such as column-curvature ductility, drift ratio, RDR, yielding of reinforcement, abutment deformation for probabilistic seismic bridge assessment (e.g., Mackie and Stojadinovic 2001, Padgett and DesRoches 2008, Ramanathan et al. 2012, Billah and Allam 2015). In this study, we evaluated the seismic performance of the three-span bridge based on CDR. Figure 3.11 illustrates the experimental fragility curves representing the probability of exceedance of DSs for a given CDR (or MDR defined in Vosooghi and Saiidi 2012). Note that the fragility curves were assumed to be lognormally distributed. Table 3.2 lists the median and logarithmic standard deviation values of CDR-based DS fragility curves. The DS_1 level exhibited the greatest dispersion, as indicated by these results.

Figure 3. 10. Possible apparent damage states of bridge columns.

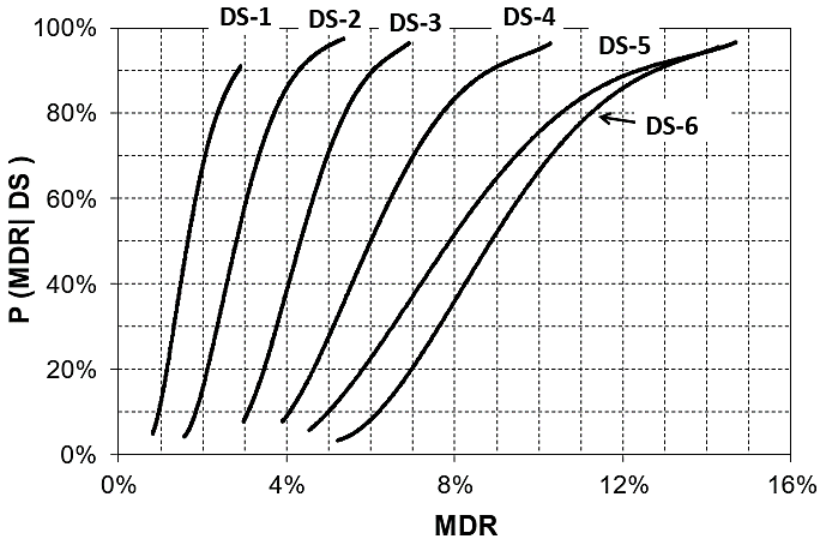

Figure 3. 11. Experimental fragility curves representing the probability of exceedance of DSs for a given CDR (or strictly speaking, MDR as defined by Vosooghi and Saiidi 2012).

Table 3. 2. Median and logarithmic standard deviation values of CDR-based DS fragility curves.

	DS_1	DS_2	DS_3	DS_4	DS_5
S_c	0.0165	0.028	0.043	0.060	0.079
β_c	0.425	0.332	0.264	0.303	0.353

3.4.2. Probability of Exceedances of Damage States

The experimental fragility curves were adopted (Vosooghi and Saiidi 2012), as the capacity-based limit state model to assess the probability that the demand is exceeding the capacity for a given IM level (Nielson 2005), as expressed by the following equation:

$$P[D > C|IM] = \Phi\left[\frac{\ln\left(\frac{S_d}{S_c}\right)}{\sqrt{\beta_{D|IM}^2 + \beta_c^2}}\right] \tag{3.2}$$

where Φ is the cumulative standard normal distribution, S_d is the mean estimate of the demand, S_c is the mean estimate of the capacity, $\beta_{D|IM}$ and β_c correspond to the logarithmic standard deviations of the demand and the capacity, respectively. Total uncertainty is determined as the square root of the sum of the squares of these individual uncertainties.

Figure 3.12 demonstrates the probabilities of CDR exceeding DS thresholds ($P(CDR>DS_i)$), which were computed for each site at T_R=975 years (left panel) and T_R=2475 years (right panel). It was observed that the elastic PSHA-based GMSS approach based on UHS tended to result in conservative estimates of the probability of exceedance of DS levels at T_R=975 years, particularly for the sites with higher seismicity. For UHS as a target spectrum at T_R=975 years, selection of input motions based on inelastic PSHA-based GMSS approach reduced the conservatism in the estimation of response compared to the elastic PSHA-based GMSS approach. At T_R=2475 years, the inelastic PSHA-based GMSS approach tended to result in DS exceedance probabilities that were generally comparable or slightly higher than those obtained from the elastic PSHA-based GMSS approach, particularly at higher DS levels.

In the case of CMS-based ground motions, at T_R=975 years, slightly lower mean and dispersion in structural responses from elastic PSHA-based GMSS approach for relatively high seismic sites resulted in lower DS exceedance probabilities compared to those obtained from inelastic PSHA-based GMSS approach. On the other hand, at T_R=2475 years, the elastic PSHA-based GMSS approach tended to yield DS exceedance probabilities that were generally

comparable or slightly higher than those obtained from the inelastic PSHA-based GMSS approach, except in San Bernardino.

When comparing UHS- and CMS-based cases, it is evident that CMS-based ground motions selected using both GMSS approaches resulted in lower DS exceedance probabilities, particularly for DS_3 levels at T_R=2475 years.

Overall, the DSs at T_R=975 years indicated that the three-span bridge considered in this study was prone to DS_1 in Los Angeles, San Francisco, and Long Beach, and more susceptible DS_2 in San Bernardino and Oakland. At T_R=2475 years, the three-span bridge was more likely to experience DS_2 in Los Angeles, San Francisco, and Long Beach, and more prone to DS_3 in San Bernardino and Oakland. Saini and Saiidi (2014) linked the DSs to the level of functionality and operability of the bridge. For instance, at DS_1, the bridge remains fully operational after the earthquake without any repairs needed. The DS_2 may not affect the bridge functionality, but repairs might be needed at plastic hinge locations. At DS_3, the bridge is closed to public access and repairs are required for the entire column. As the DS level increases, the severity of the damage and required repairs would increase.

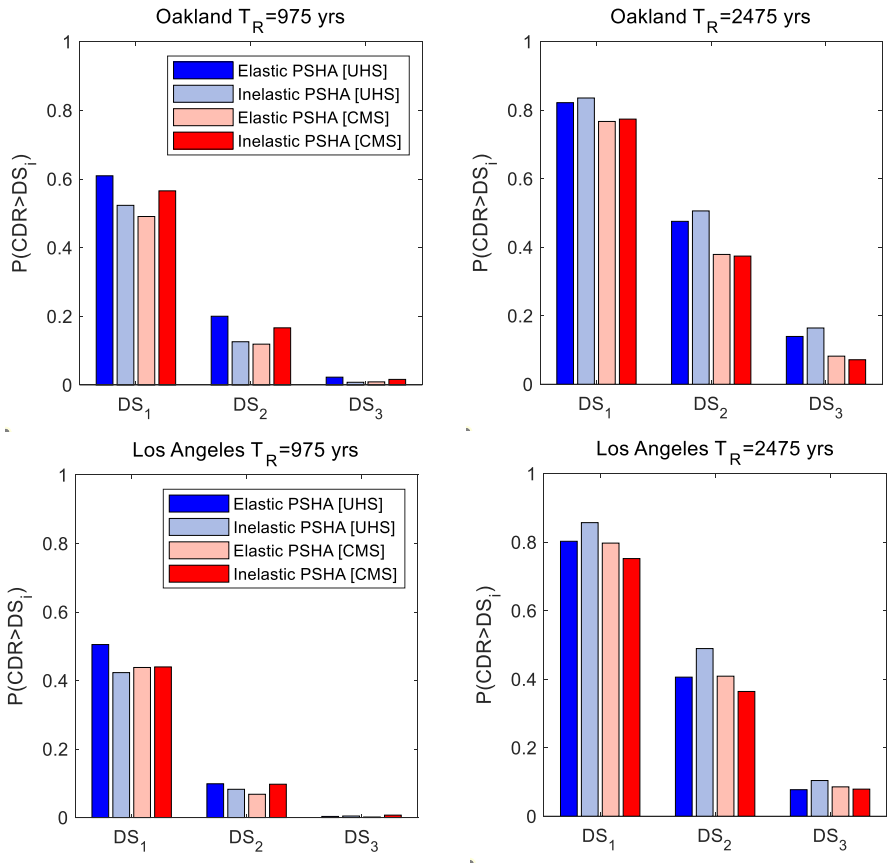

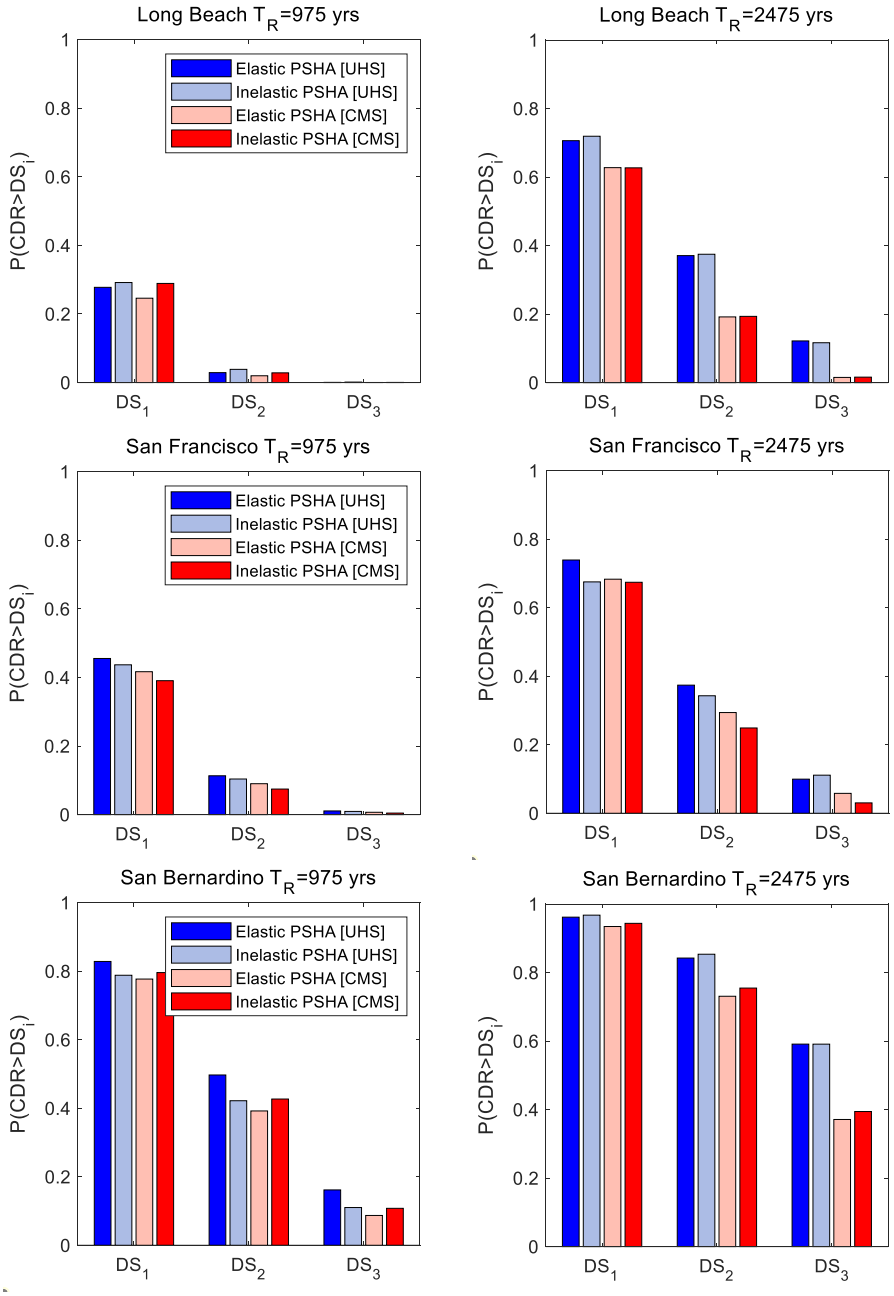

Figure 3. 12. The probabilities of CDR exceeding DS thresholds at T_R=975 years and T_R=2475 years.

3.4.3. Analytical Fragility Curves

Fragility analysis plays a crucial role in assessing damage and losses by estimating the conditional probabilities of exceeding predefined limit states at various seismic hazard levels. The fragility curves obtained from different GMSS approaches were computed. Figure 3.13 presents the fragility curves derived from UHS-based ground motions selected using different GMSS approaches in the left panel, while the right panel displays the fragilities computed using CMS-

based ground motions. These curves account only for demand uncertainty related to ground motion. To obtain fragility curves that specifically account for demand uncertainty related to ground motion, a series of steps were followed:

(1) NRHAs were conducted at multiple IM levels [corresponding to a range of T_R values of 200, 475, 975, 2475 and 5000 years] using sets of scaled ground motions, resulting in distributions of structural responses. This way, the varying dispersions in structural response at each IM level were considered.
(2) The median values of the capacity limits were used to assess the number of observations that exceeded the damage state limit, at each IM level.
(3) The probability of exceedance was determined by counting the fraction of records with responses greater than the specified damage state limit.
(4) The maximum likelihood estimation (MLE) method was utilized to fit a lognormal curve.

Here, fragility functions were computed for three DSs in San Bernardino and Oakland. For other sites, fragility curves were presented only for DS_1 and DS_2 because DS_3 threshold was exceeded only in a few instances, thus limiting the data.

.

Tables 3.3 and 3.4 list the median and the logarithmic standard deviation values of the UHS-and CMS-based fragility curves for each site, respectively. The median Sa represents the Sa value at which there is a 50% probability of exceeding a specific DS level. A higher median Sa value (μ) indicates a lower probability of damage, or a less fragile case, implying that the bridge can withstand earthquakes of higher intensity. The standard deviation or dispersion of the fragility curve ("β" value on the tables) determines the slope of the fragility curve. When the dispersion is reduced, the curves become steeper, generally indicating a decrease in exceedance probabilities at lower Sa levels and an increase at higher Sa levels.

The results indicated that the median estimates derived from CMS-based fragility curves were higher than those obtained from UHS-based counterparts, leading to a shift to the right in the fragility curves. This indicated that CMS-based records generally resulted in less conservative estimates of bridge response compared to UHS-based records. This difference became more evident as the DS level increased.

The use of inelastic UHS-based records tended generally to decrease the dispersion values of the fragility curves compared to elastic UHS-based records, with some exceptions. Moreover, the inelastic PSHA-based GMSS approach generally reduced the conservatism of the elastic PSHA-based GMSS approach. When considering CMS-based ground motions, the degree of conservatism or lack thereof observed across different GMSS approaches was inconsistent and varied depending on the site. In that case, the inelastic PSHA-based GMSS approach did not necessarily result in reduced dispersion of the fragility curves compared to the elastic PSHA-based GMSS approach.

In the context of CMS cases, as previously discussed, variations in structural response were observed to be influenced by the extent of mismatch between the recorded spectra and the inelastic spectra. In this context, the inelastic PSHA-based GMSS approach demonstrated a consistent alignment of all recorded spectra with both the elastic and inelastic target spectra across all ductility levels. Conversely, the elastic PSHA-based GMSS approach generally underestimated the target mean inelastic CMS spectra. However, in sites like Long Beach, Oakland and Los Angeles, the mean recorded spectra from this approach exceeded the target mean inelastic spectra at certain return periods. This led to conservative fragilities at the DS_2 level compared to those obtained using the inelastic PSHA-based GMSS approach.

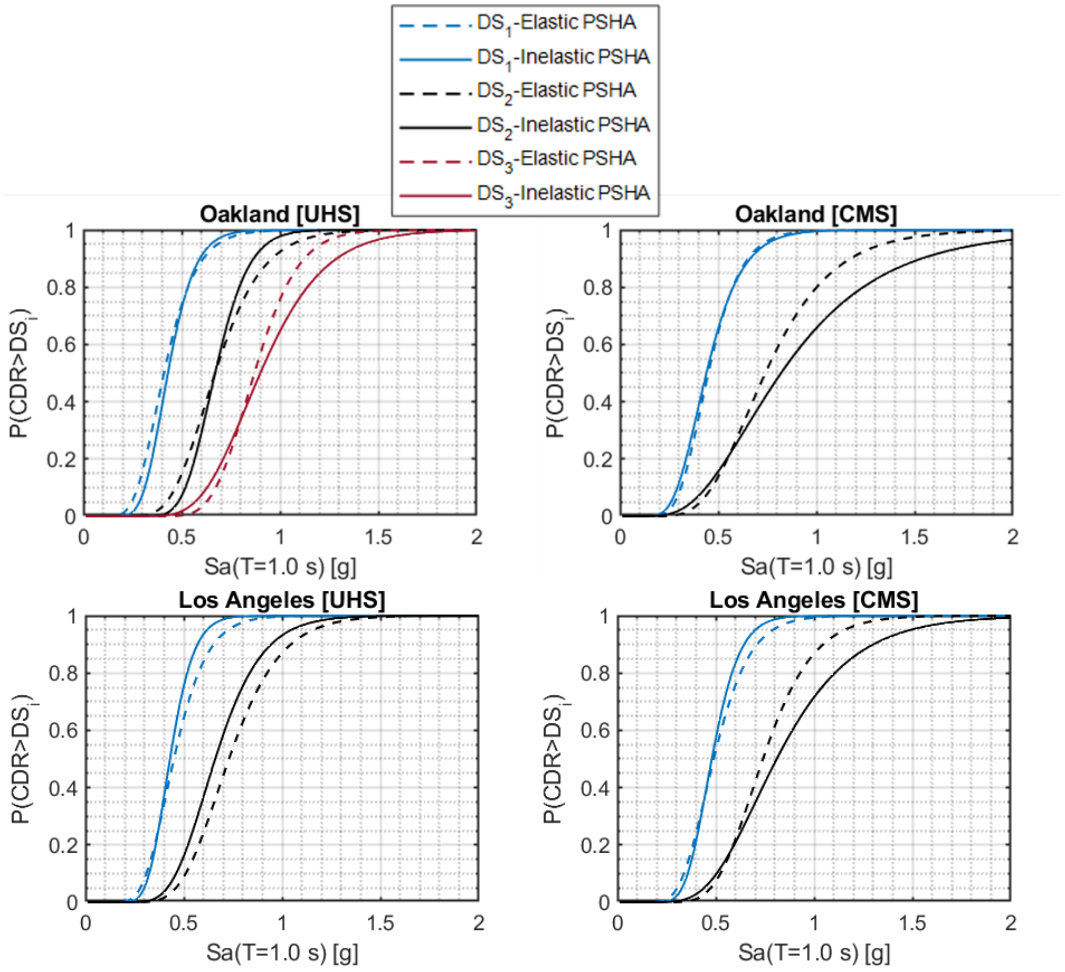

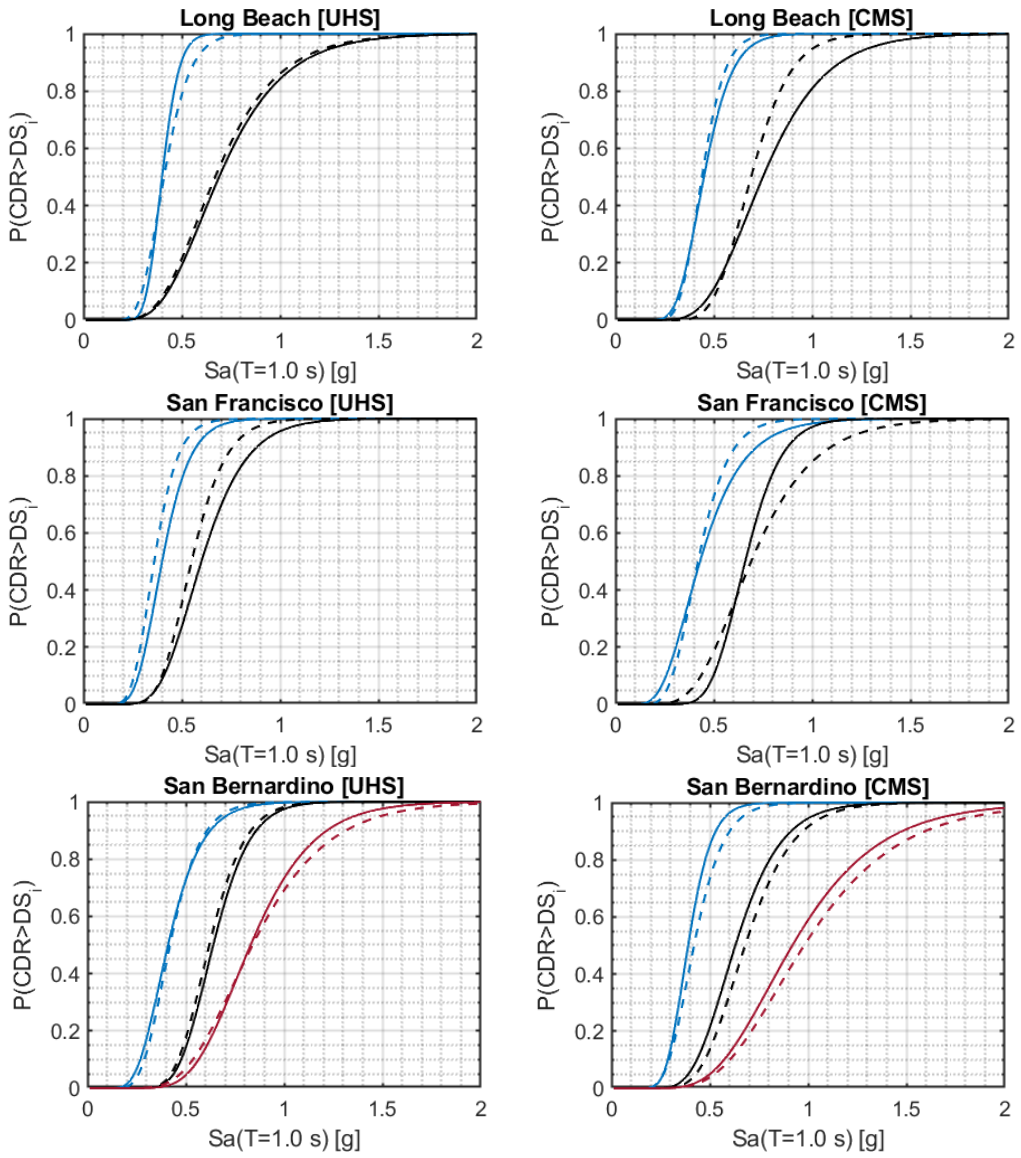

Figure 3. 13. Fragility curves including demand uncertainty for different GMSS approaches.

Table 3. 3. Parameters of fragility curves including demand uncertainty (UHS-cases)

Site	**DS_1-Elastic PSHA**		**DS_1-Inelastic PSHA**		**DS_2-Elastic PSHA**		**DS_2-Inelastic PSHA**		**DS_3-Elastic PSHA**		**DS_3-Inelastic PSHA**	
	μ	B	μ	β	μ	β	μ	β	μ	B	μ	β
Oakland	0.41	0.31	0.43	0.25	0.67	0.28	0.67	0.2	0.87	0.2	0.9	0.28
Long Beach	0.41	0.25	0.4	0.17	0.67	0.37	0.69	0.37	-	-	-	-
Los Angeles	0.45	0.29	0.43	0.22	0.73	0.28	0.66	0.28	-	-	-	-
San Francisco	0.36	0.26	0.4	0.28	0.55	0.25	0.6	0.3	-	-	-	-
San Bernardino	0.42	0.29	0.41	0.33	0.62	0.23	0.64	0.23	0.84	0.35	0.83	0.30

Table 3. 4. Parameters of fragility curves including demand uncertainty (CMS-cases)

Site	DS_1-Elastic PSHA		DS_1-Inelastic PSHA		DS_2-Elastic PSHA		DS_2-Inelastic PSHA		DS_3-Elastic PSHA		DS_3-Inelastic PSHA	
	μ	β	μ	β	μ	β	μ	β	μ	β	μ	β
Oakland	0.45	0.29	0.44	0.32	0.74	0.36	0.82	0.49	-	-	-	-
Long Beach	0.44	0.21	0.45	0.25	0.69	0.23	0.75	0.33	-	-	-	-
Los Angeles	0.49	0.29	0.48	0.23	0.74	0.27	0.81	0.37	-	-	-	-
San Francisco	0.42	0.29	0.43	0.4	0.69	0.36	0.66	0.22	-	-	-	-
San Bernardino	0.42	0.28	0.39	0.24	0.68	0.28	0.63	0.29	0.98	0.38	0.92	0.37

Figure 3.14 depicts the fragility curves that incorporate both demand and capacity uncertainties. In this case, the mean and the logarithmic standard deviation values of the demand and capacity models were implemented from Equation (3.2) to calculate the discrete probabilities of exceeding the DS. The lognormal curve was fitted to the discrete probabilities by minimizing the sum of squared errors (SSE) between the actual and fitted values. Tables 3.5 and 3.6 list the median and the logarithmic standard deviation values of the UHS-and CMS-based fragility curves for each site, respectively.

The differences observed between different GMSS approaches for demand-only uncertainty-based fragilities also remained consistent when incorporating both demand and capacity uncertainties. The inclusion of capacity uncertainties caused a shift in the median values of the fragility curves, indicating an increase in vulnerability of the bridge structure. As expected, the inclusion of the standard deviation associated with capacity uncertainty led to an increase in the dispersions of the fragility curves. In Equation 3.2, including capacity uncertainty increases overall variability in the assessment. Consequently, the median in the fragility curve shifts leftward as it reflects a more conservative scenario accounting for uncertain demand and capacity.

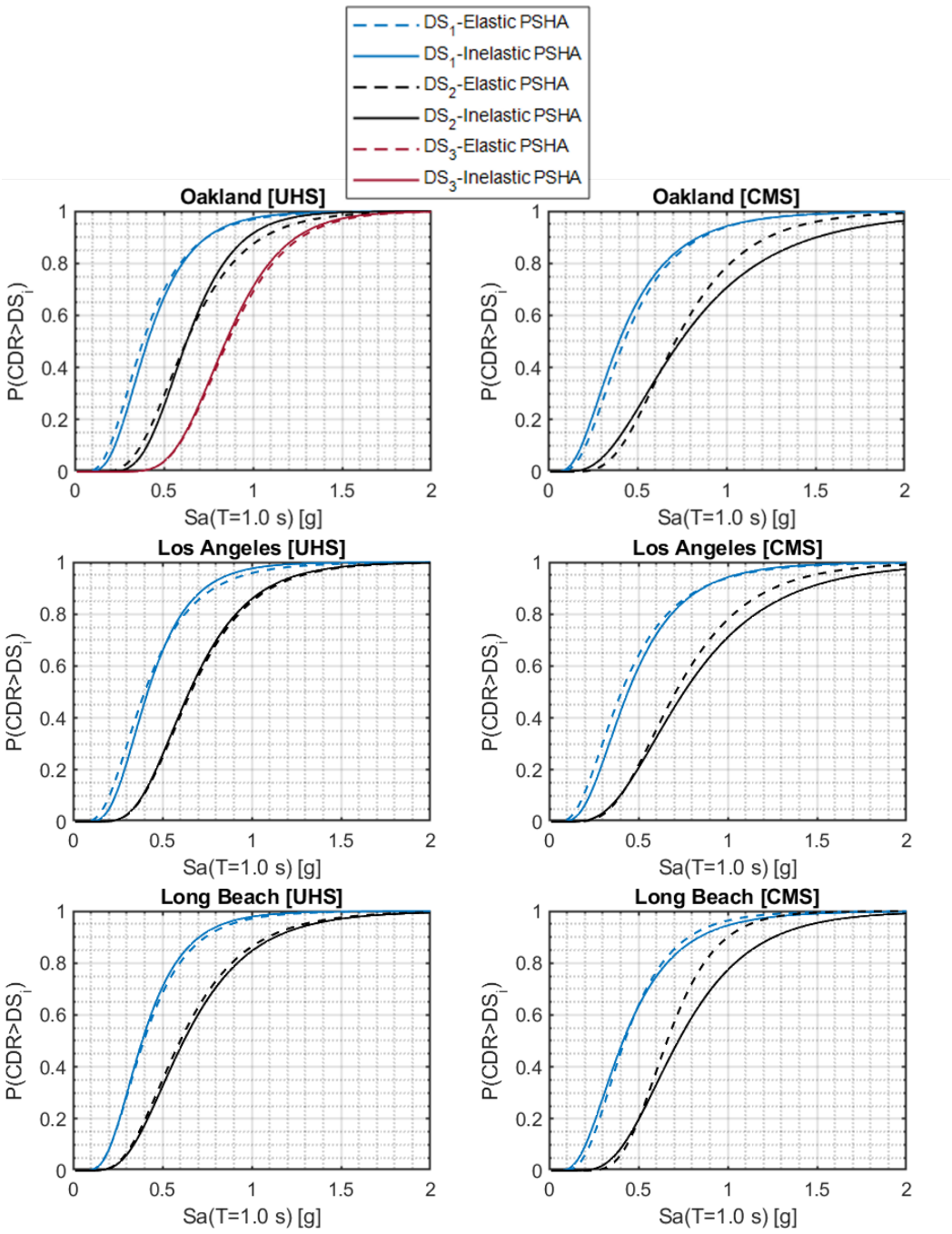
DS1-Elastic PSHA
DS1-Inelastic PSHA
DS2-Elastic PSHA
DS2-Inelastic PSHA
DS3-Elastic PSHA
DS3-Inelastic PSHA
Oakland [UHS]
Oakland [CMS]
Los Angeles [UHS]
Los Angeles [CMS]
Long Beach [UHS]
Long Beach [CMS]
P(CDR>DSi)
Sa(T=1.0 s) [g]

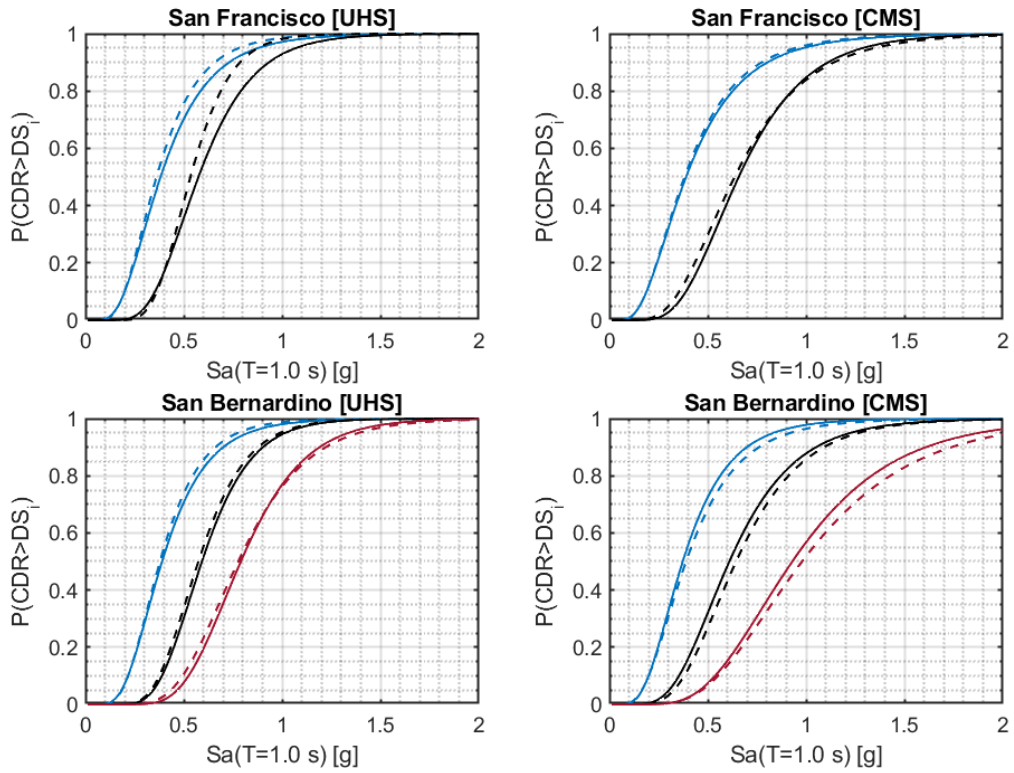

Figure 3. 14. Fragility curves including demand and capacity uncertainties for different GMSS approaches.

Table 3. 5. Parameters of fragility curves including demand and capacity uncertainties (UHS-cases)

Site	DS_1-Elastic PSHA		DS_1-Inelastic PSHA		DS_2-Elastic PSHA		DS_2-Inelastic PSHA		DS_3-Elastic PSHA		DS_3-Inelastic PSHA	
	μ	B	μ	β	μ	B	μ	β	μ	β	μ	β
Oakland	0.38	0.52	0.41	0.47	0.63	0.41	0.63	0.34	0.86	0.31	0.85	0.3
Long Beach	0.40	0.49	0.39	0.47	0.60	0.47	0.62	0.47	-	-	-	-
Los Angeles	0.40	0.53	0.42	0.44	0.66	0.40	0.65	0.40	-	-	-	-
San Francisco	0.36	0.47	0.38	0.51	0.53	0.30	0.57	0.38	-	-	-	-
San Bernardino	0.38	0.43	0.39	0.46	0.57	0.33	0.59	0.33	0.78	0.35	0.79	0.32

Table 3. 6. Parameters of fragility curves including demand and capacity uncertainties (CMS-cases)

Site	DS_1-Elastic PSHA		DS_1-Inelastic PSHA		DS_2-Elastic PSHA		DS_2-Inelastic PSHA		DS_3-Elastic PSHA		DS_3-Inelastic PSHA	
	μ	β	μ	B	μ	β	μ	β	μ	B	μ	β
Oakland	0.43	0.55	0.40	0.59	0.71	0.43	0.74	0.55	-	-	-	-
Long Beach	0.42	0.48	0.41	0.55	0.66	0.32	0.72	0.43	-	-	-	-
Los Angeles	0.41	0.58	0.44	0.52	0.71	0.45	0.76	0.51	-	-	-	-
San Francisco	0.38	0.55	0.39	0.56	0.64	0.46	0.66	0.41	-	-	-	-
San Bernardino	0.39	0.52	0.37	0.49	0.64	0.41	0.61	0.42	0.98	0.45	0.93	0.43

3.4.4. Probabilistic Risk Assessment

The annual rate of exceedance of a CDR for a threshold level x (i.e., seismic risk curve, or EDP hazard, $\lambda_{EDP}(x)$) can be computed using Equation 3.3 (see, e.g., Krawinkler and Miranda 2004, Der Kiureghian 2005). Note that the seismic risk curve's behavior is determined by convolving the fragility curve with the mean seismic hazard curve. In this study, a discrete summation approximation was utilized to calculate the annual rate of exceedance of a CDR for a specified threshold level x.

$$\lambda_{EDP}(x) = \sum_{im_i} P(CDR > x | IM = im_i).\Delta\lambda_{IM}(im_i) \tag{3.3}$$

where $P(CDR > x|IM = im_i)$ represents the probability of exceeding a specified CDR level, x, for a given $IM = im_i$. Distribution of the structural response was obtained from sets of scaled ground motions that, on average, were compatible with the target IM level. It was assumed that the structural response at each IM level (or return period) followed a lognormal distribution. $\Delta\lambda_{IM}(im_i) = \lambda_{IM}(im_i) - \lambda_{IM}(im_{i+1})$ approximates the annual rate of occurrence of IM being equal to im_i. Equation 3.3 can be generalized such that λ can be based on the traditional elastic PSHA or based on PSHA of an inelastic SDOF system.

Figure 3.15 compares the CDR risk curves (or EDP hazard curve) of the bridge obtained from different GMSS approaches for each site. It is observed that the differences in risk curves were influenced by the selected target spectra definitions, i.e., UHS and CMS, particularly at higher levels of the CDR (i.e., CDR>0.03). The CDR curves derived from CMS-based ground motions generally tended to provide a lower bound (both in terms of annual probability of exceedance and CDR) compared to the UHS-based ground motions. This suggests that the UHS-

based approach is generally more conservative when evaluating the seismic risk, as it leads to a higher annual rate of exceeding a CDR level.

In the comparison of GMSS approaches, it is observed that elastic UHS-based GMSS ground motions generally tended to slightly overestimate the annual rate of exceedance of CDR when compared to inelastic UHS-based GMSS approach. This finding aligned with the trend observed in fragility curves, indicating that the elastic UHS-based GMSS approach generally provided more conservative estimates of the seismic risk for the three-span bridge considered in this study. However, the differences were generally not substantial, as most of the fragility curves closely aligned.

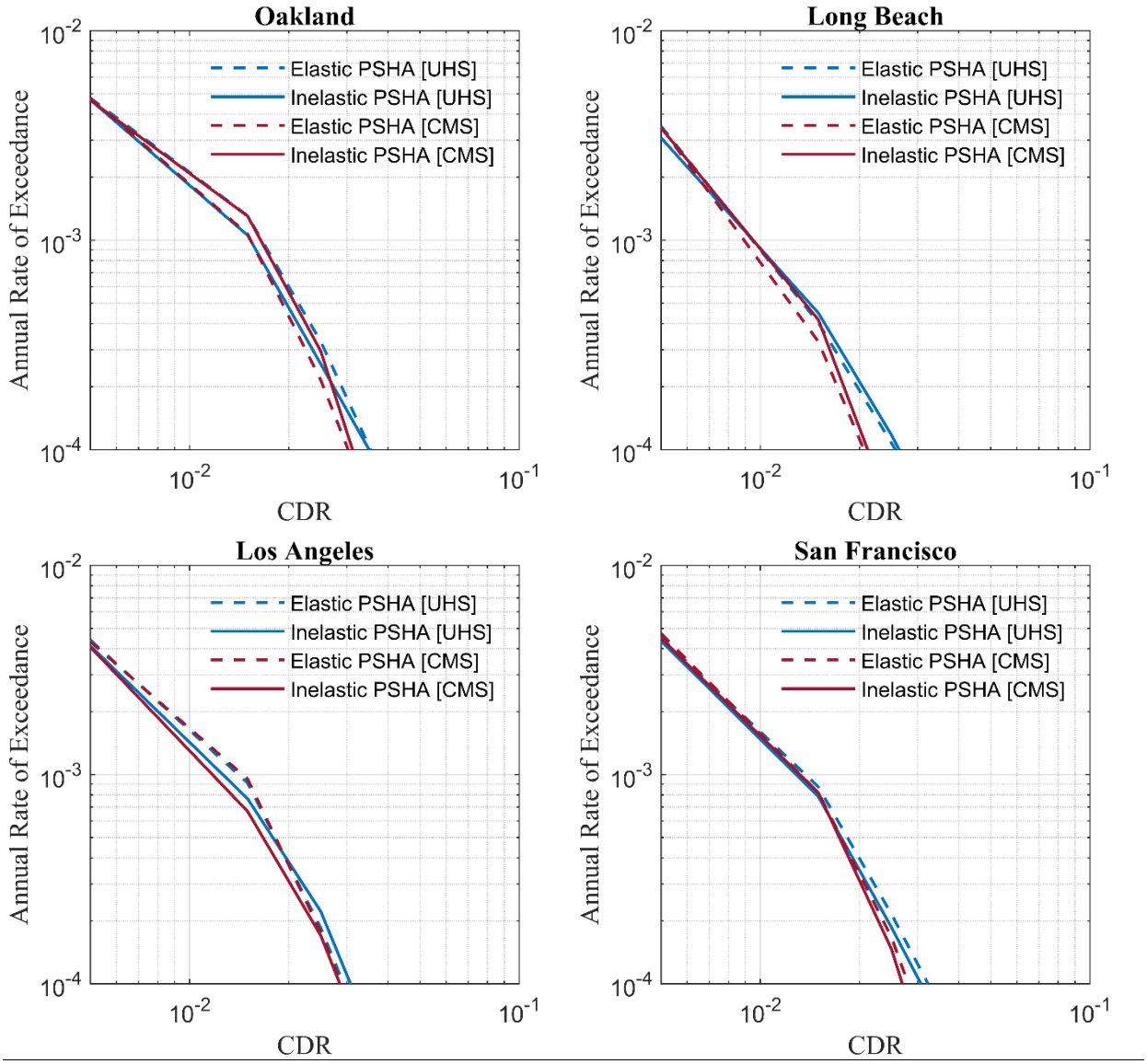

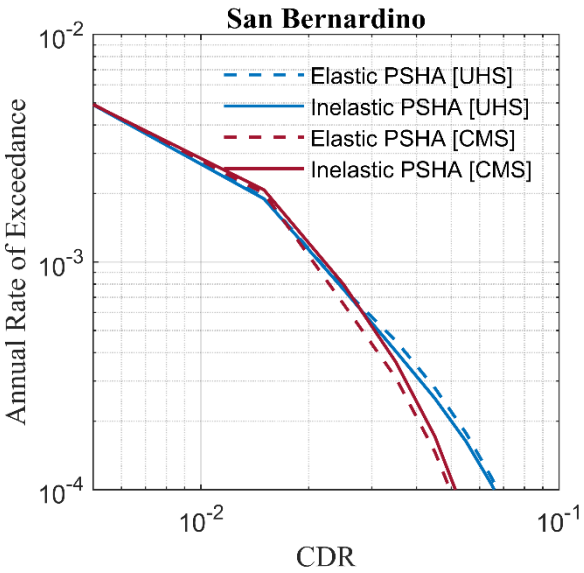

Figure 3. 15. Comparisons of CDR risk curves based on different GMSS approaches.

4 Summary and Conclusions

This report presents comparative analyses of the impact of different ground motion selection and scaling (GMSS) approaches on the seismic performance of a three-span typical bridge designed in accordance with the Caltrans SDC (2019). Two methods of GMSS were considered: GMSS based on elastic (traditional) and inelastic target spectra. Both elastic and inelastic target spectra were the results of probabilistic seismic hazard analysis (PSHA). Five sites in California were included in the study, having different seismicity levels, i.e., Oakland, Los Angeles, Long Beach, San Francisco, and San Bernardino. At each site, target Uniform Hazard Spectrum (UHS) and Conditional Mean Spectrum (CMS) were generated based on traditional elastic PSHA, and based on inelastic PSHA for five return periods: (T_R)=200, 475, 975, 2475, and 5000 years. At each T_R level, sets of 25 ground motions were selected and scaled using both GMSS approaches, and used as inputs for nonlinear response history analyses (NRHA) of a three-span typical bridge in California.

A three-dimensional (3D) OpenSees bridge model was developed for the NRHA. The effects of GMSS approaches on distributions of engineering seismic demand parameters (EDPs) including column drift ratio (CDR), residual drift ratio (RDR), displacement ductility (μD) of the three-span bridge models were investigated at T_R=975 years and T_R=2475 years.

The NRHA results revealed that at T_R =975 years, the use of elastic PSHA-based UHS ground motions led to mean values of comparable or somewhat higher structural response, especially in relatively high seismic sites. At T_R=2475 years, the inelastic PSHA-based GMSS approach was more effective in reducing the dispersion in structural response compared to the traditional elastic PSHA-based GMSS approach. The CMS-based ground motions selected by both GMSS approaches yielded comparable mean CDR and μD values, which could be attributed to a relatively close match between response spectra of elastic PSHA-based CMS records and target inelastic spectra across ductility levels. The UHS-based ground motions from both GMSS approaches generally yielded higher mean estimates of bridge responses compared to their CMS-based counterparts. Furthermore, the findings highlighted the crucial role of pulse-like records in seismic bridge design due to their significant impact on RDR.

This study also compared CDRs from elastic single-degree-of-freedom (SDOF), inelastic SDOF, linear response history analysis (LRHA), and NRHA methods at T_R =975 years and

T_R=2475 years. Findings suggested that while elastic SDOF approximates linear response well, elastic/inelastic SDOF analyses and LRHA methods might underestimate CDRs compared to NRHA, particularly for higher ductility demands. The validity of the equal displacement rule for the bridge structure was also considered in this study. Equal displacement assumption can underestimate inelastic displacement, especially in for large earthquake magnitudes and large ductility. The findings suggested that solely relying on linear elastic analyses in high-seismic sites might lead to unsafe designs. Implementing a diverse set of analytical methods could significantly enhance the safety of designs in these regions.

In the context of fragility curves, the fragility curves derived from inelastic PSHA-based UHS generally tended to reduce the dispersion of fragility curves, especially in high seismicity sites. In the case of CMS-based fragilities, the level of conservatism or lack thereof varied across sites for elastic PSHA-based GMSS approach.

EDP hazard curves or seismic risk curves for the bridge at five sites were also developed in this study. The findings indicated that the selected target spectra, UHS and CMS, had a significant influence on CDR risk curves, particularly at higher CDR levels (CDR>0.03). Specifically, the CMS-based CDR risk curves tended to yield lower annual rate of exceedances compared to the UHS-based risk curves.

The results of this study highlight the intricate relationship between GMSS approaches, EDP responses, fragilities, and seismic risk (EDP hazard) curves, and emphasize the importance of carefully selecting appropriate GMSS approaches and target spectra when assessing the seismic risk of bridges. With the recent development of inelastic GMMs, inelastic PSHA-based target spectra, and computer tools, Selecting and scaling ground motions to “match” inelastic target response spectra is possible. Such motions have a potential of reducing dispersion of the nonlinear structural response particularly at high seismicity sites. The traditional elastic PSHA-based GMSS approach can yield either conservative or unconservative results compared to the inelastic PSHA-based GMSS approach, depending on the mismatch between recorded and target inelastic spectra. The fragility functions and seismic risk curves derived in this report are specific to the bridge configurations, seismic hazard levels of sites, and soil conditions that have been evaluated and may not accurately represent different bridge configurations or loading scenarios. Future research should consider the sensitivity of results to various sources of uncertainties, such as geometry and material uncertainties when creating bridge models, different bridge types, and the number of ground motions.

5 References

Aviram, A., Mackie, K. R., and Stojadinovic, B. (2008). Effect of abutment modeling on the seismic response of bridge structures. *Earthquake engineering and engineering vibration*, 7, 395-402.

Bahrampouri, M., Bozorgnia Y., Mazzoni, S., and Campbell, K. (2023). *Use of inelastic response spectra in seismic hazard analysis and design*. DOI: 10.34948/N38G6K.

Borzi, B., Ceresa, P., Franchin, P., Noto, F., Calvi, G. M., & Pinto, P. E. (2015). Seismic vulnerability of the Italian roadway bridge stock. *Earthquake Spectra*, 31(4), 2137-2161.

Bozorgnia, Y., Hachem, M. M., and Campbell, K. W. (2010). Ground motion prediction equation ("attenuation relationship") for inelastic response spectra, *Earthquake Spectra* 26, 1–23.

Bozorgnia, Y., and Bertero, V. V. (2004). *Earthquake Engineering: From Engineering Seismology to Performance-Based Engineering*, CRC Press, Boca Raton, FL.

Bradley, B. A. (2010). A generalized conditional intensity measure approach and holistic ground-motion selection. *Earthquake Engineering and Structural Dynamics*, 39(12), 1321-1342.

Campbell, K. W., and Bozorgnia, Y. (2014). NGA-West2 ground motion model for the average horizontal components of PGA, PGV, and 5% damped linear acceleration response spectra. *Earthquake Spectra*, 30(3), 1087-1115.

Choi, E., DesRoches, R., and Nielson, B. (2004). Seismic fragility of typical bridges in moderate seismic zones. *Engineering structures*, 26(2), 187-199.

Choi, H., Saiidi, M. S., Somerville, P., and El-Azazy, S. (2010). Experimental study of reinforced concrete bridge columns subjected to near-fault ground motions. *ACI Structural Journal*, 107(1), 3.

Field, E. H., Jordan, T. H., and Cornell, C. A. (2003). OpenSHA: A developing community-modeling environment for seismic hazard analysis. *Seismological Research Letters*, 74(4), 406-419.

Field, E. H., Arrowsmith, R. J., Biasi, G. P., Bird, P., Dawson, T. E., Felzer, K. R., ... & Zeng, Y. (2014). Uniform California earthquake rupture forecast, version 3 (UCERF3)—The time-independent model. *Bulletin of the Seismological Society of America*, *104*(3), 1122-1180.

Gardoni, P., Der Kiureghian, A., and Mosalam, K. M. (2002). Probabilistic capacity models and fragility estimates for reinforced concrete columns based on experimental observations. *Journal of Engineering Mechanics*, 128(10), 1024-1038.

Kiureghian, A. D. (2005). Non-ergodicity and PEER's framework formula. *Earthquake Engineering and Structural Dynamics*, 34(13), 1643-1652.

Kohrangi, M., Bazzurro, P., and Vamvatsikos, D. (2016). Vector and scalar IMs in structural response estimation, Part I: Hazard analysis. *Earthquake Spectra*, 32(3), 1507-1524.

Krawinkler, H., and Miranda, E. (2004). Performance-based earthquake engineering. *Earthquake engineering: from engineering seismology to performance-based engineering*, Bozorgnia and Bertero (Ed.), CRC Press, Chapter 9, 1-9.

Kullback, S., and. Leibler, R. A (1951). On information and sufficiency. *The Ann. of Math. Statistics*, vol. 22, no. 1, pp. 79–86.

Mackie, K., and Stojadinović, B. (2001). Probabilistic seismic demand model for California highway bridges. *Journal of Bridge Engineering*, 6(6), 468-481.

Mackie, K., and Stojadinović, B. (2003). *Seismic demands for performance-based design of bridges.* Berkeley: Pacific Earthquake Engineering Research Center.

Mander, J. B., Priestley, M. J. N., and Park, R. (1988). Observed stress-strain behavior of confined concrete. *Journal of structural engineering*, 114(8), 1827-1849.

Mazzoni, S., McKenna, F., Scott, M. H., and Fenves, G. L. (2006). *OpenSees command language manual*. Pacific earthquake engineering research (PEER) center, 264(1), 137-158.

Mazzoni, S., Bozorgnia, Y., Bahrampouri, M. (2023). *Expansion of NGA-West2 ground-motion database to include inelastic-response intensity measures*. GIRS 2023-07 report. DOI:10.34948/N3B88W.

McKenna, F., Scott, M. H., and Fenves, G. L. (2010). Nonlinear finite-element analysis software architecture using object composition. *Journal of Computing in Civil Engineering*, 24(1), 95-107.

Menegotto M, Pinto P. (1973) Method of Analysis for Cyclically Loaded R.C. Plane Frames Including Changes in Geometry and Non-Elastic Behavior of Elements under Combined Normal Force and Bending, in: *IABSE Symposium of Resistance and Ultimate Deformability of Structures Acted on by Well Defined Repeated Loads*, Lisbon.

Monteiro, R., Zelaschi, C., Silva, A., and Pinho, R. (2019). Derivation of fragility functions for seismic assessment of RC bridge portfolios using different intensity measures. *Journal of Earthquake Engineering*, 23(10), 1678-1694.

Muntasir Billah, A. H. M., and Alam, M. S. (2015). Seismic fragility assessment of concrete bridge pier reinforced with superelastic shape memory alloy. *Earthquake Spectra*, 31(3), 1515-1541.

Neuenhofer, A., and Filippou, F. C. (1998). Geometrically nonlinear flexibility-based frame finite element. *Journal of Structural Engineering*, 124(6), 704-711.

Nielson, B. G. (2005). *Analytical fragility curves for highway bridges in moderate seismic zones*. Ph.D. thesis, Georgia Institute of Technology, Atlanta.

Padgett, J. E., and DesRoches, R. (2008). Methodology for the development of analytical fragility curves for retrofitted bridges. *Earthquake Engineering and Structural Dynamics*, 37(8), 1157-1174.

Padgett, J. E., Nielson, B. G., and DesRoches, R. (2008). Selection of optimal intensity measures in probabilistic seismic demand models of highway bridge portfolios. *Earthquake Engineering and Structural Dynamics*, 37(5), 711-725.

Phan, V., Saiidi, M. S., Anderson, J., and Ghasemi, H. (2007). Near-fault ground motion effects on reinforced concrete bridge columns. *Journal of structural engineering*, 133(7), 982-989.

Ramanathan, K., DesRoches, R., and Padgett, J. E. (2012). A comparison of pre-and post-seismic design considerations in moderate seismic zones through the fragility assessment of multispan bridge classes. *Engineering Structures*, 45, 559-573.

Saini, A., and Saiidi, M. (2014). *Probabilistic damage control approach for seismic design of bridge columns*. California Department of Transportation.

Scott, M. H., and Hamutçuoğlu, O. M. (2008). Numerically consistent regularization of force-based frame elements. *International journal for numerical methods in engineering*, 76(10), 1612-1631.

Seismic Design Criteria (2019). *Version 2.0, California Department of Transportation (Caltrans)*, Sacramento, CA.

Shahi, S. K., and Baker, J. W. (2014). An efficient algorithm to identify strong-velocity pulses in multicomponent ground motions. *Bulletin of the Seismological Society of America*, 104(5), 2456-2466.

Shoushtari, E., Saiidi, M. S., Itani, A., and Moustafa, M. A. (2021). Seismic performance of a two-span steel girder bridge with ABC connections. *Engineering Structures*, 241, 112502.

Tarbali, K., Bradley, B. A., and Baker, J. W. (2019). Ground motion selection in the near-fault region considering directivity-induced pulse effects. *Earthquake Spectra*, 35(2), 759-786.

Veletsos, A. S., and Newmark, N. M. (1960, July). *Effect of inelastic behavior on the response of simple systems to earthquake motions*. Department of Civil Engineering, University of Illinois.

Vosooghi, A., and Saiidi, M. S. (2012). Experimental fragility curves for seismic response of reinforced concrete bridge columns. *ACI Structural Journal*, 109(6), 825.

Yassin, M. H. M. (1994). *Nonlinear analysis of prestressed concrete structures under monotonic and cyclic loads*. University of California, Berkeley.

Zengin, E., and Abrahamson, N. A. (2020). A vector-valued intensity measure for near-fault ground motions. *Earthquake Engineering and Structural Dynamics*, 49(7), 716-734.

Zengin, E., and Abrahamson, N. (2020). Conditional Ground-Motion Model for Damaging Characteristics of Near-Fault Ground Motions Based on Instantaneous Power. *Bulletin of the Seismological Society of America*, 110(6), 2828-2842.

Zengin, E., and Abrahamson, N. A. (2021). A procedure for matching the near-fault ground motions based on spectral accelerations and instantaneous power. *Earthquake Spectra*, 37(4), 2545-2561.

Zengin, E. (2022). Effectiveness of Instantaneous Power in predicting the collapse responses of structures under pulse-like ground motions*. Advances in Structural Engineering*, 25(8), 1806-1814.

6 Appendix A: Comparisons Between Record Spectra and Target Spectra Using Different GMSS Approaches

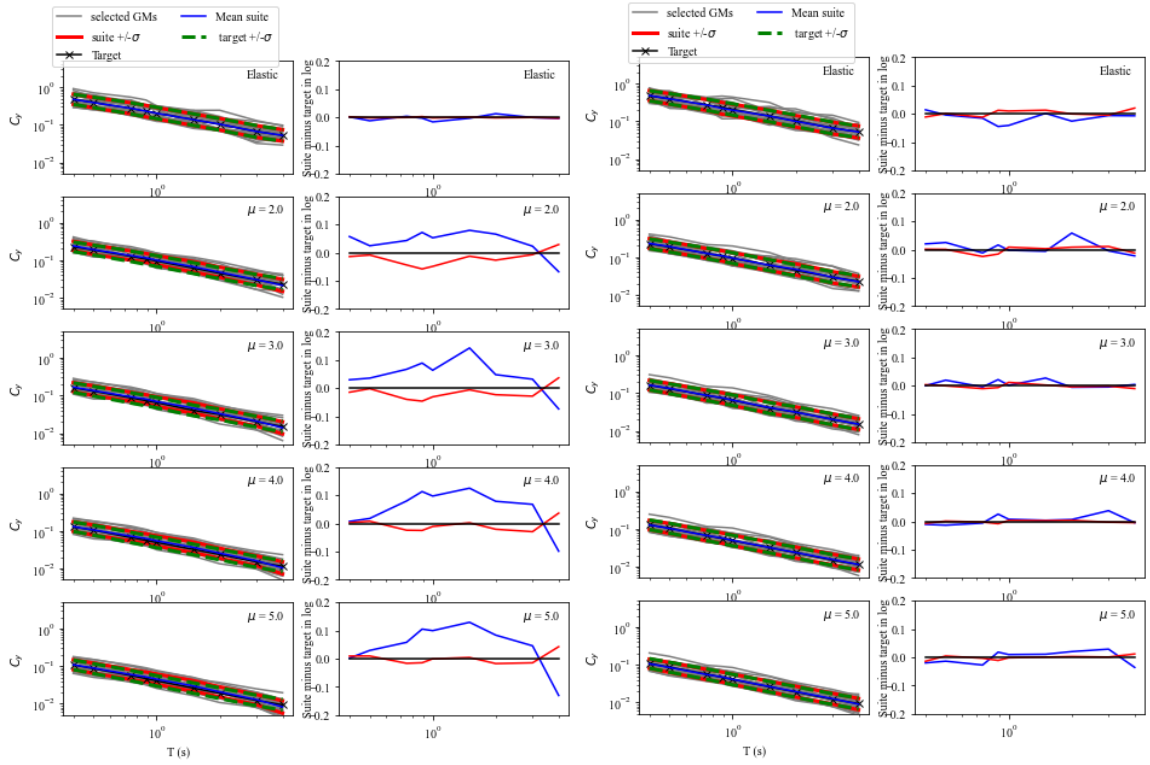

Figure A.1. Comparisons of the spectra of the suite mean and standard deviation with the targets for elastic and inelastic **UHS** representing different ductility levels, at **T_R=200 years**, for **Oakland**, using elastic PSHA-based GMSS approach (left panel) and inelastic PSHA-based GMSS approach (right panel).

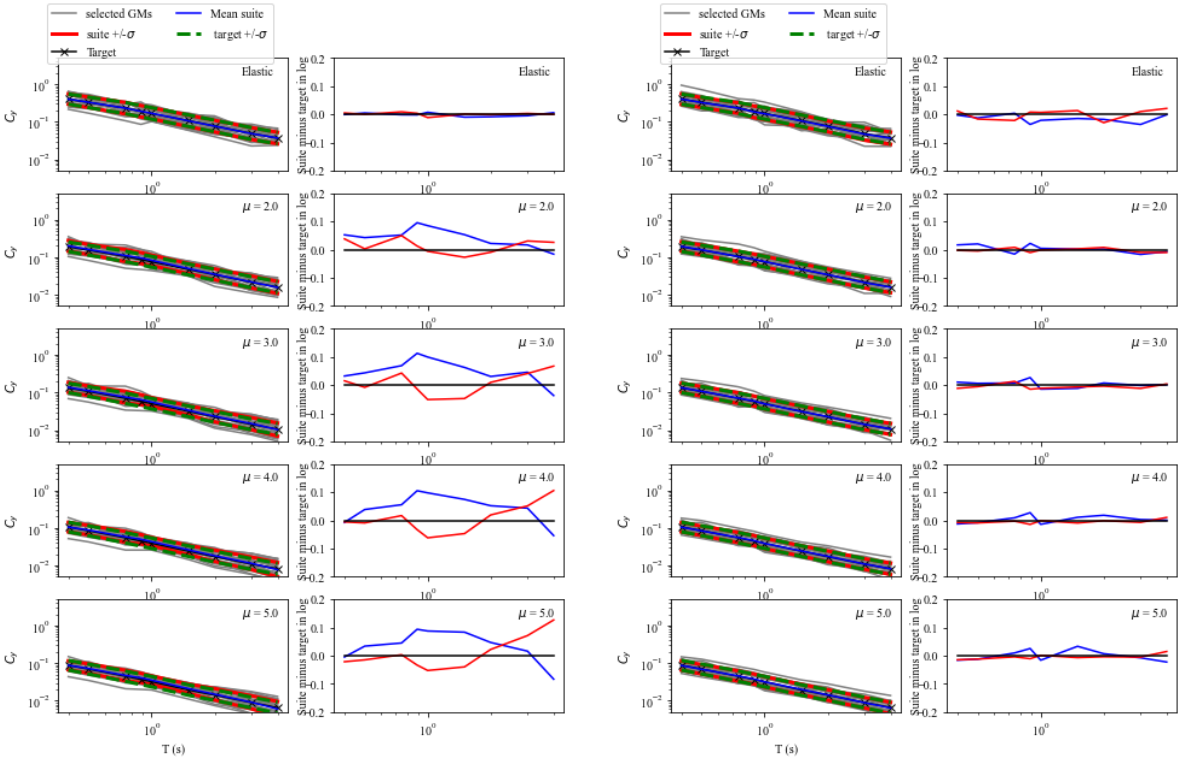

Figure A.2. Comparisons of the spectra of the suite mean and standard deviation with the targets for elastic and inelastic **UHS** representing different ductility levels, at **T_R=200 years**, for **Los Angeles**, using elastic PSHA-based GMSS approach (left panel) and inelastic PSHA-based GMSS approach (right panel).

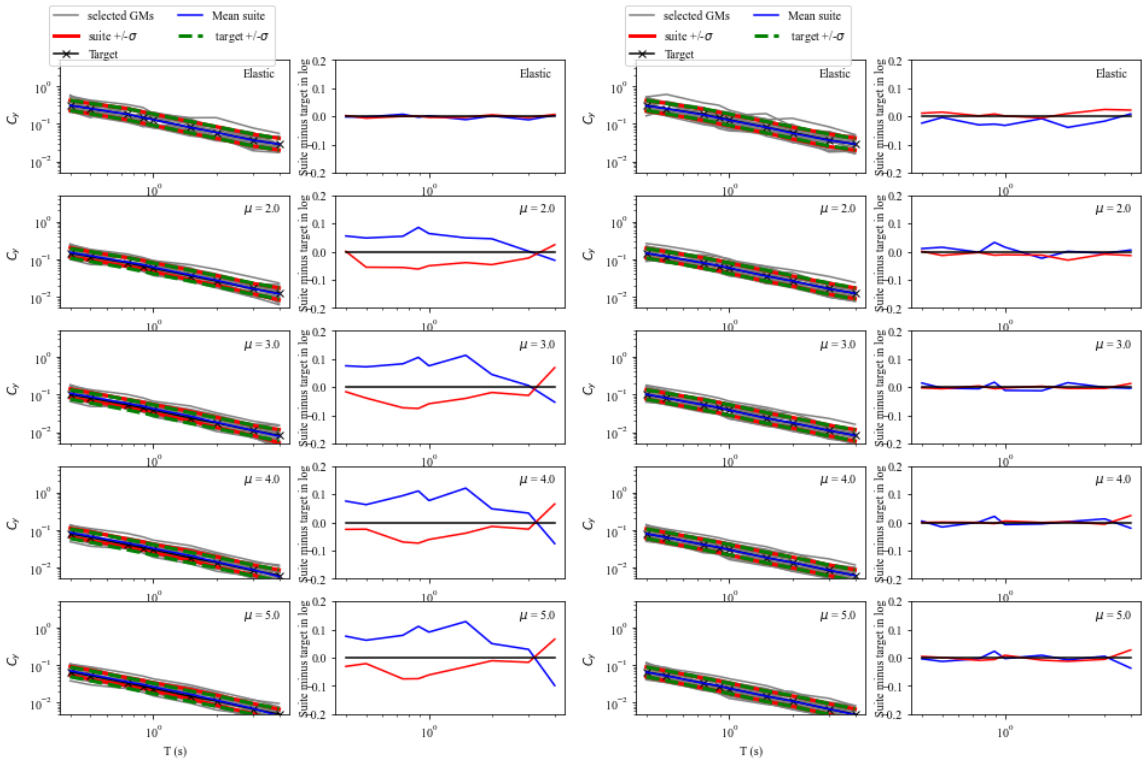

Figure A.3. Comparisons of the spectra of the suite mean and standard deviation with the targets for elastic and inelastic **UHS** representing different ductility levels, at **T_R=200 years**, for **Long Beach**, using elastic PSHA-based GMSS approach (left panel) and inelastic PSHA-based GMSS approach (right panel).

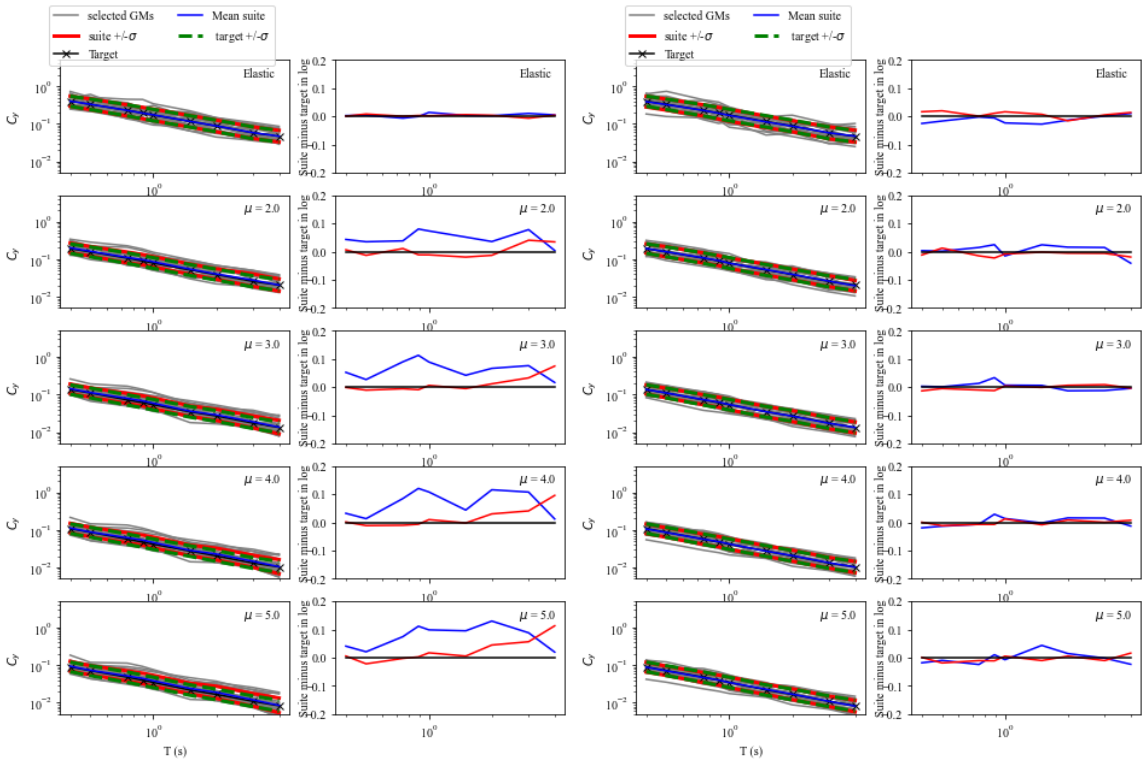

Figure A.4. Comparisons of the spectra of the suite mean and standard deviation with the targets for elastic and inelastic **UHS** representing different ductility levels, at **T_R=200 years**, for **San Francisco**, using elastic PSHA-based GMSS approach (left panel) and inelastic PSHA-based GMSS approach (right panel).

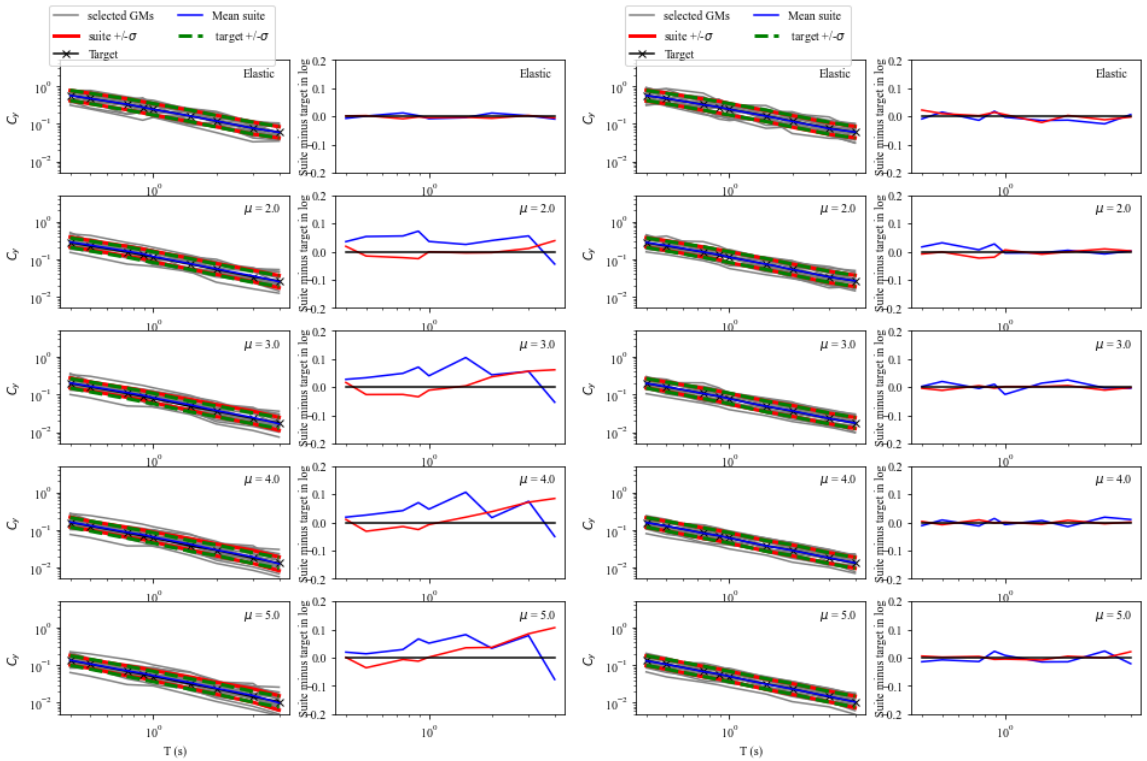

Figure A.5. Comparisons of the spectra of the suite mean and standard deviation with the targets for elastic and inelastic **UHS** representing different ductility levels, at **T_R=200 years**, for **San Bernardino**, using elastic PSHA-based GMSS approach (left panel) and inelastic PSHA-based GMSS approach (right panel).

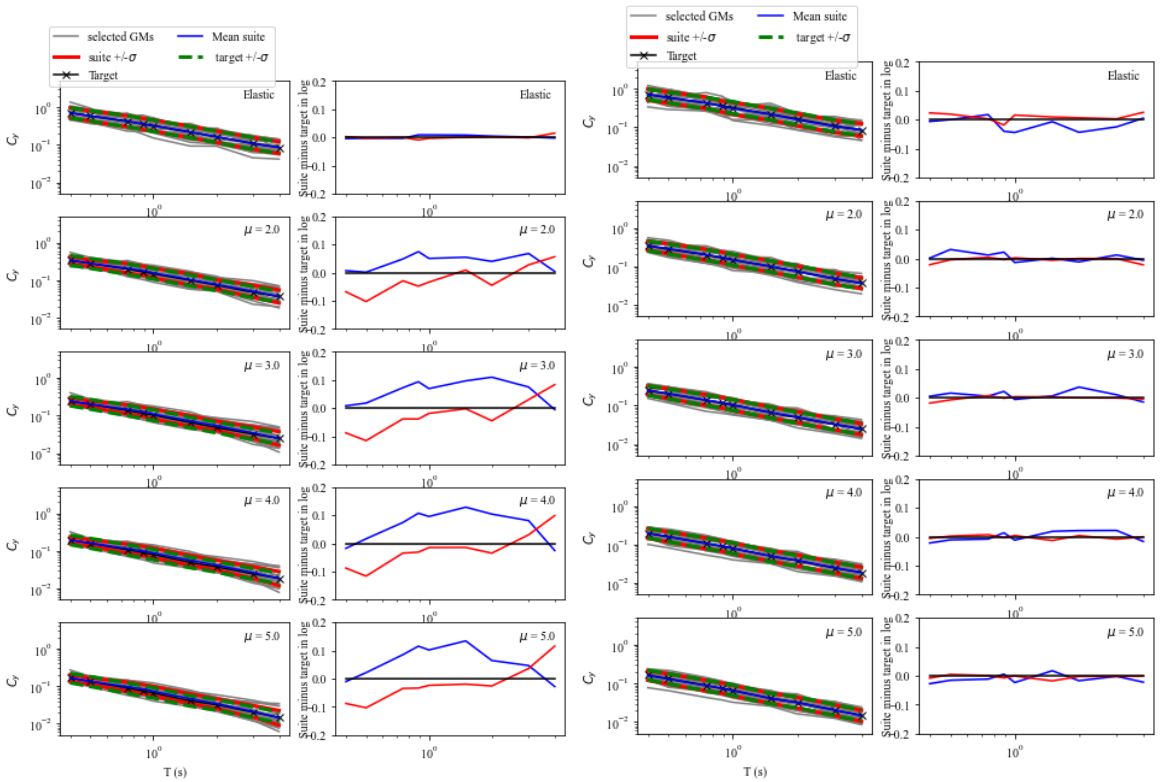

Figure A.6. Comparisons of the spectra of the suite mean and standard deviation with the targets for elastic and inelastic **UHS** representing different ductility levels, at **T_R=475 years**, for **Oakland** using elastic PSHA-based GMSS approach (left panel) and inelastic PSHA-based GMSS approach (right panel).

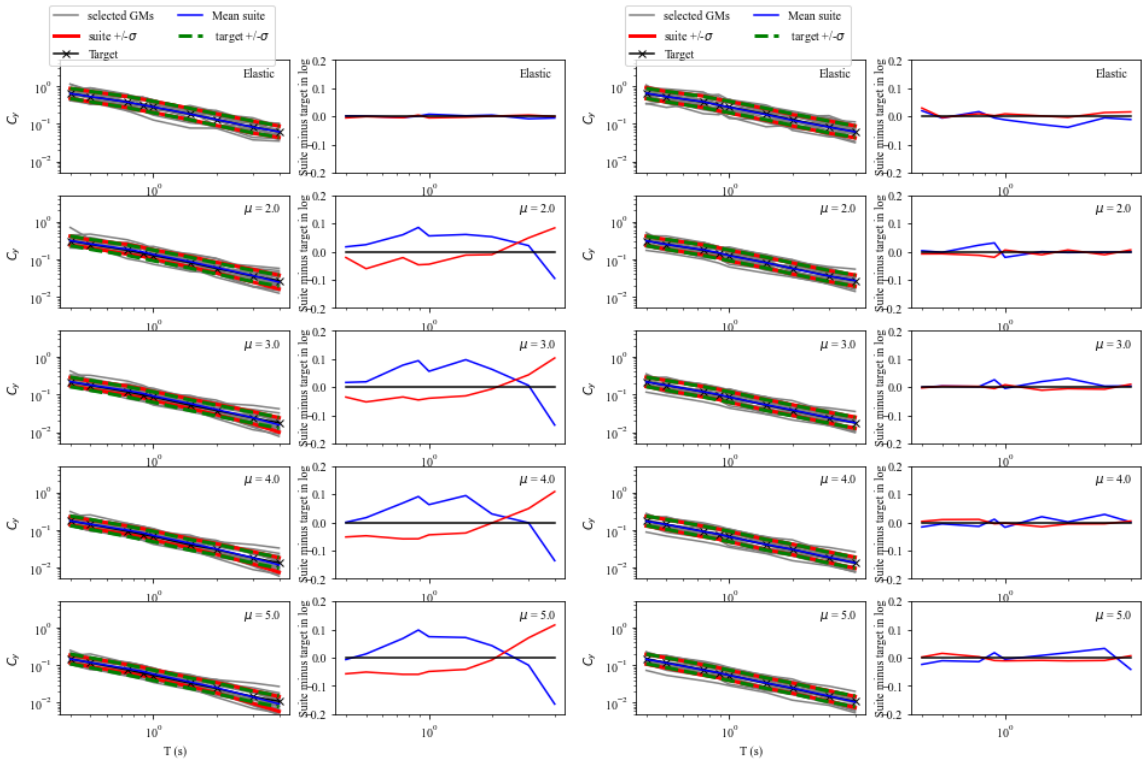

Figure A.7. Comparisons of the spectra of the suite mean and standard deviation with the targets for elastic and inelastic **UHS** representing different ductility levels, at **T_R=475 years**, for **Los Angeles** using elastic PSHA-based GMSS approach (left panel) and inelastic PSHA-based GMSS approach (right panel).

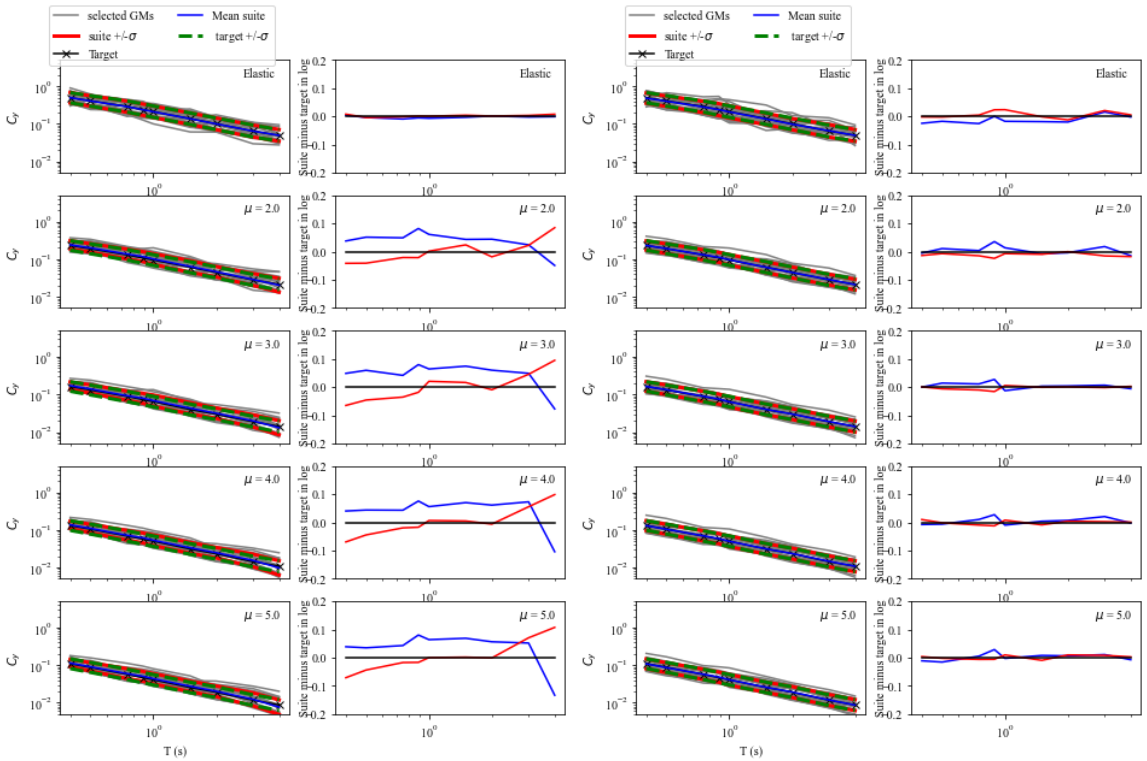

Figure A.8. Comparisons of the spectra of the suite mean and standard deviation with the targets for elastic and inelastic **UHS** representing different ductility levels, at **T_R=475 years**, for **Long Beach** using elastic PSHA-based GMSS approach (left panel) and inelastic PSHA-based GMSS approach (right panel).

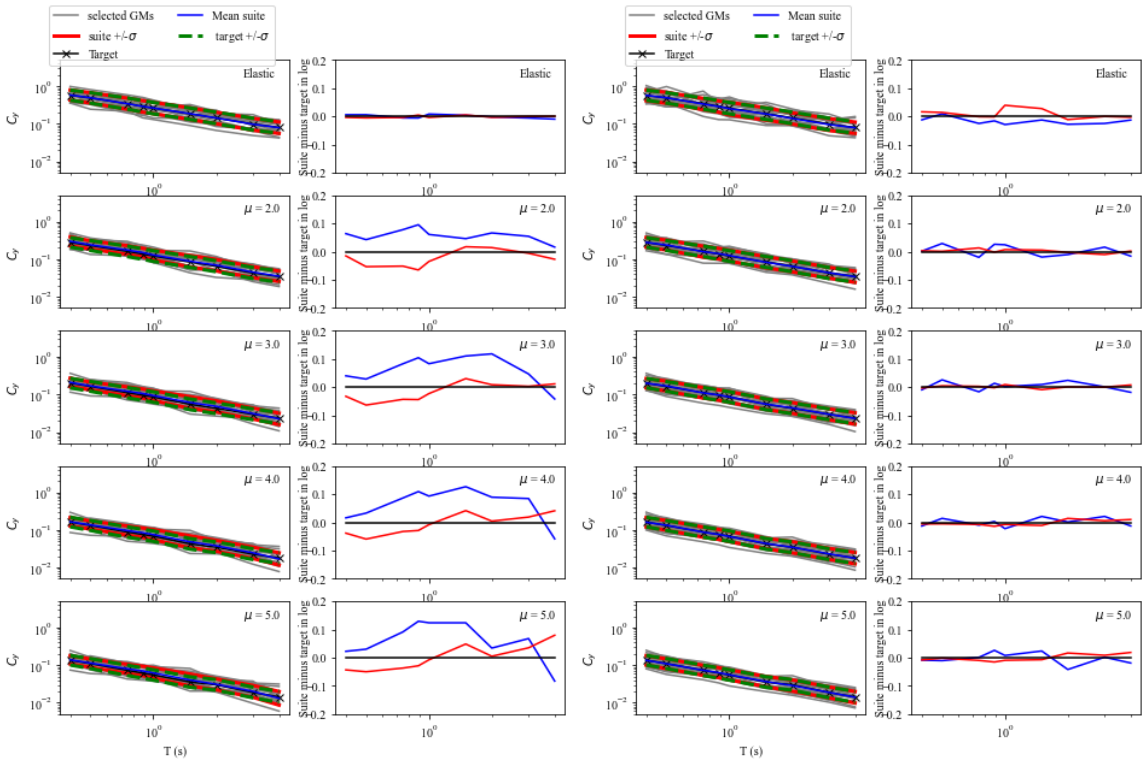

Figure A.9. Comparisons of the spectra of the suite mean and standard deviation with the targets for elastic and inelastic **UHS** representing different ductility levels, at **T_R=475 years**, **for San Francisco** using elastic PSHA-based GMSS approach (left panel) and inelastic PSHA-based GMSS approach (right panel).

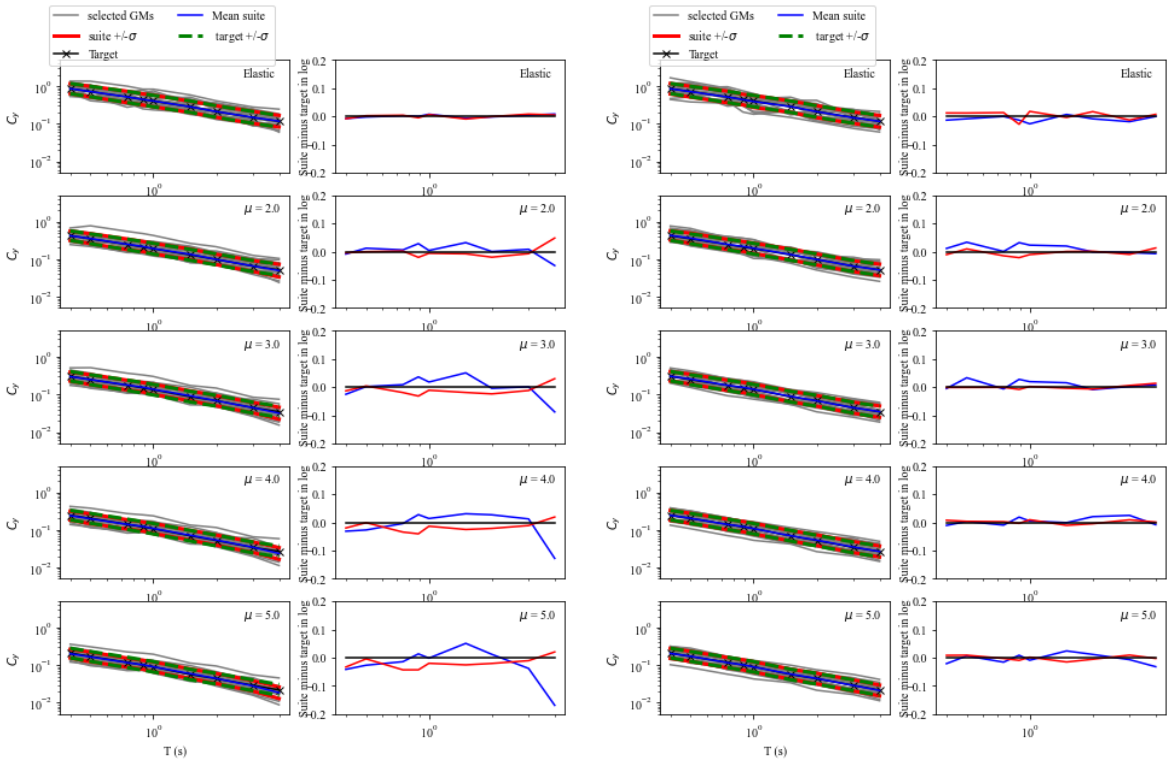

Figure A.10. Comparisons of the spectra of the suite mean and standard deviation with the targets for elastic and inelastic **UHS** representing different ductility levels, at **T_R=475 years**, for **San Bernardino** using elastic PSHA-based GMSS approach (left panel) and inelastic PSHA-based GMSS approach (right panel).

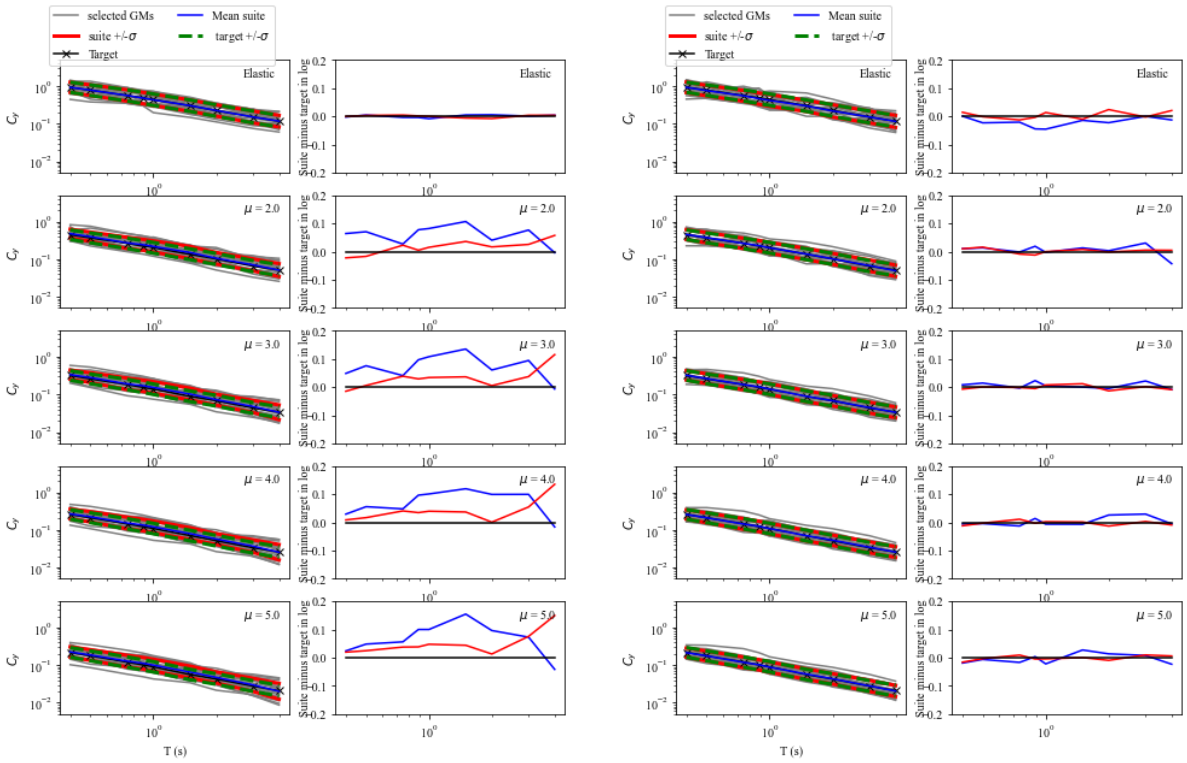

Figure A.11. Comparisons of the spectra of the suite mean and standard deviation with the targets for elastic and inelastic **UHS** representing different ductility levels, at **T_R=975 years**, for **Oakland** using elastic PSHA-based GMSS approach (left panel) and inelastic PSHA-based GMSS approach (right panel).

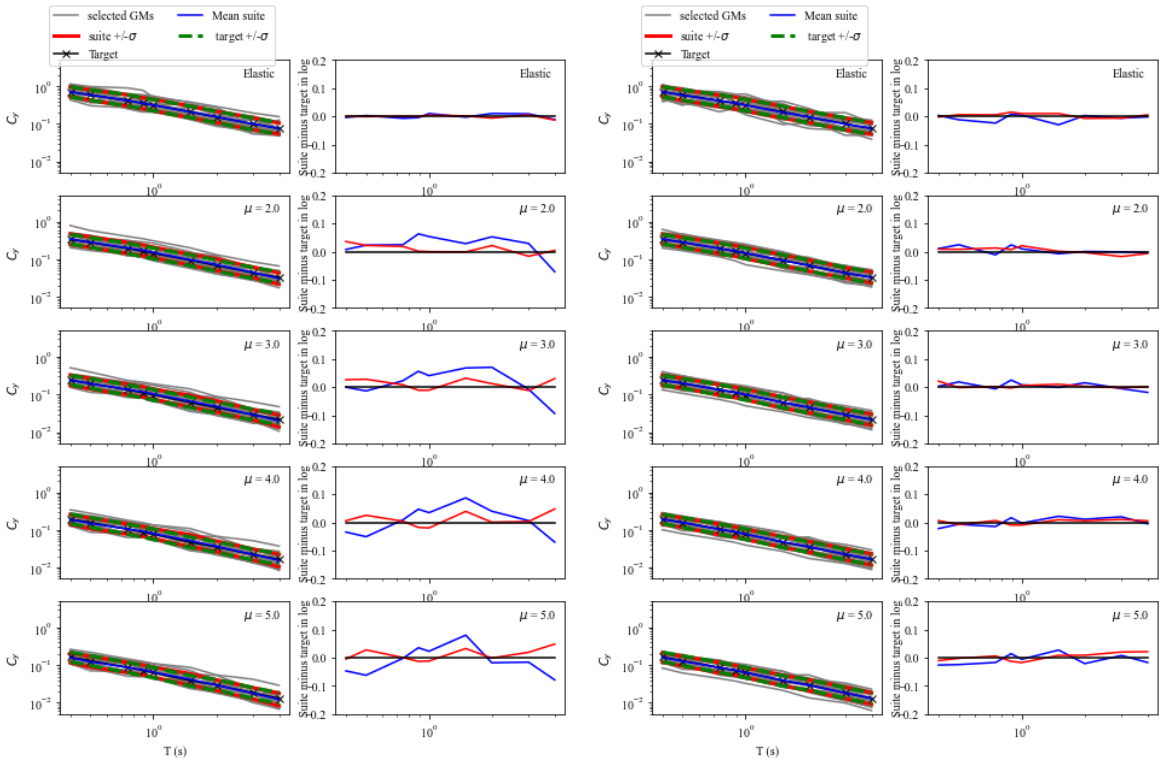

Figure A.12. Comparisons of the spectra of the suite mean and standard deviation with the targets for elastic and inelastic **UHS** representing different ductility levels, at **T_R=975 years**, for **Long Beach** using elastic PSHA-based GMSS approach (left panel) and inelastic PSHA-based GMSS approach (right panel).

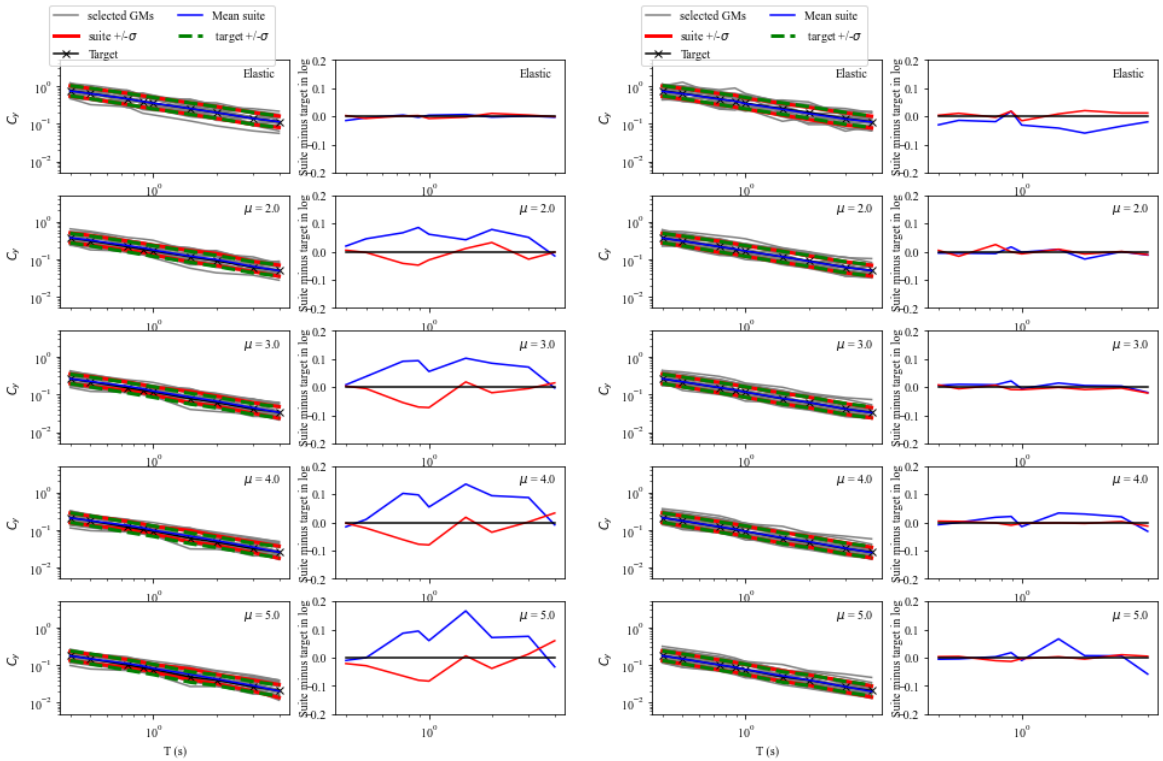

Figure A.13. Comparisons of the spectra of the suite mean and standard deviation with the targets for elastic and inelastic **UHS** representing different ductility levels, at **T_R=975 years**, for **San Francisco** using elastic PSHA-based GMSS approach (left panel) and inelastic PSHA-based GMSS approach (right panel).

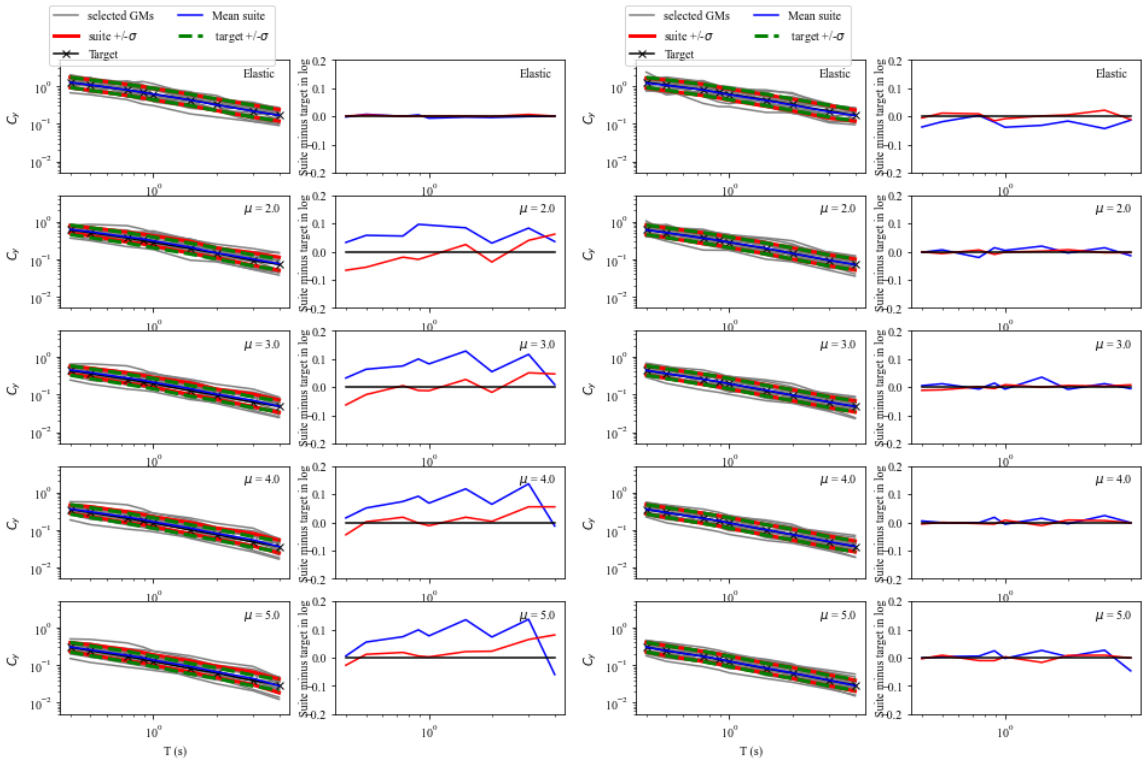

Figure A.14. Comparisons of the spectra of the suite mean and standard deviation with the targets for elastic and inelastic **UHS** representing different ductility levels, at **T_R=2475 years**, for **Oakland** using elastic PSHA-based GMSS approach (left panel) and inelastic PSHA-based GMSS approach (right panel).

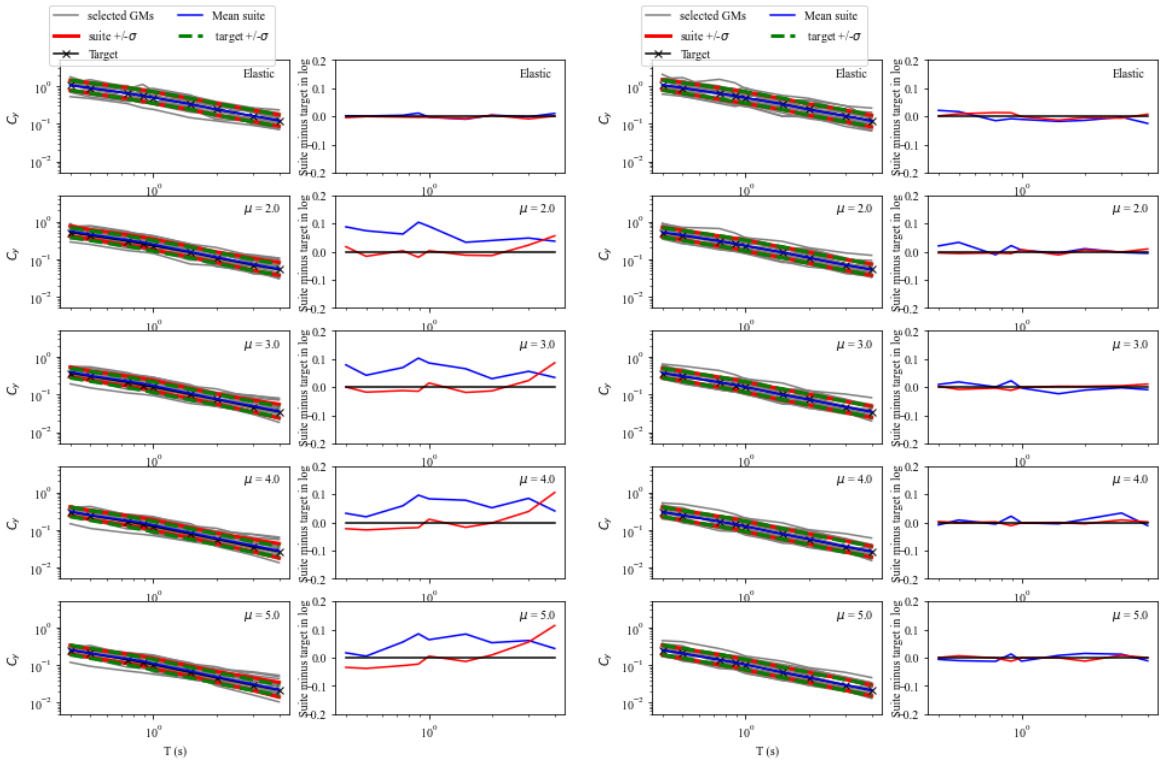

Figure A.15. Comparisons of the spectra of the suite mean and standard deviation with the targets for elastic and inelastic **UHS** representing different ductility levels, at **T_R=2475 years**, for **Long Beach** using elastic PSHA-based GMSS approach (left panel) and inelastic PSHA-based GMSS approach (right panel).

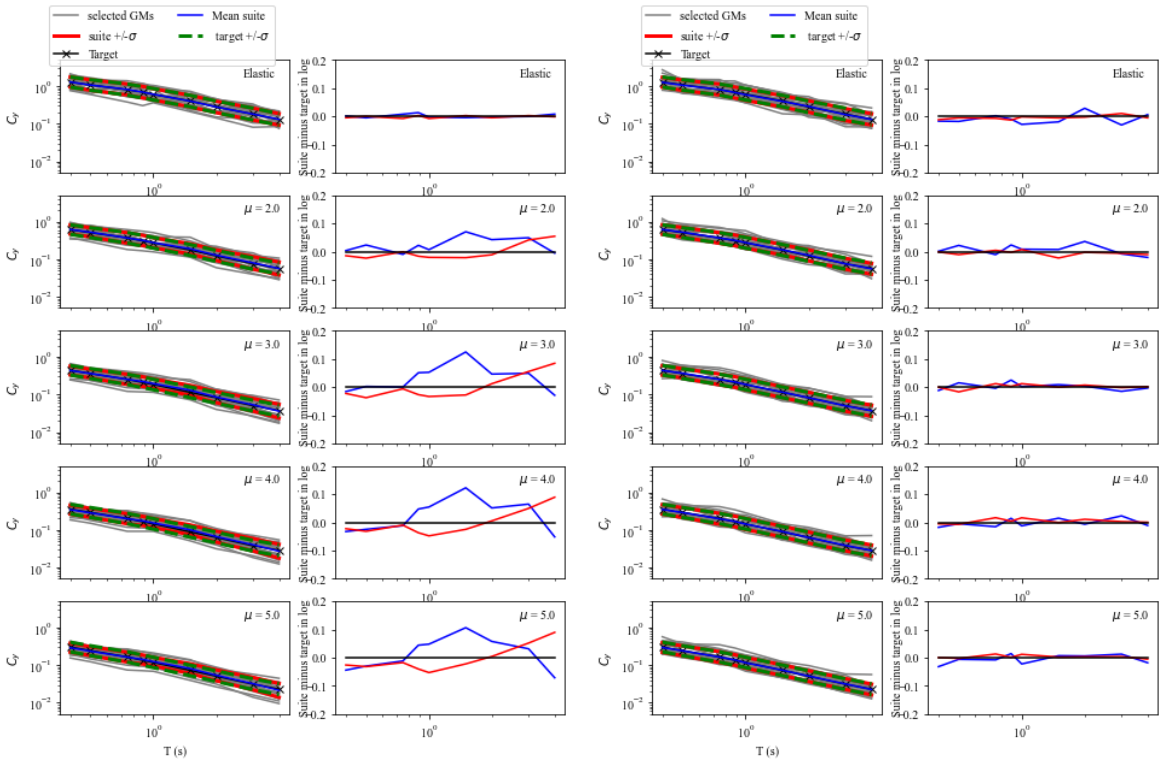

Figure A.16. Comparisons of the spectra of the suite mean and standard deviation with the targets for elastic and inelastic **UHS** representing different ductility levels, at **T_R=2475 years**, for **Los Angeles** using elastic PSHA-based GMSS approach (left panel) and inelastic PSHA-based GMSS approach (right panel).

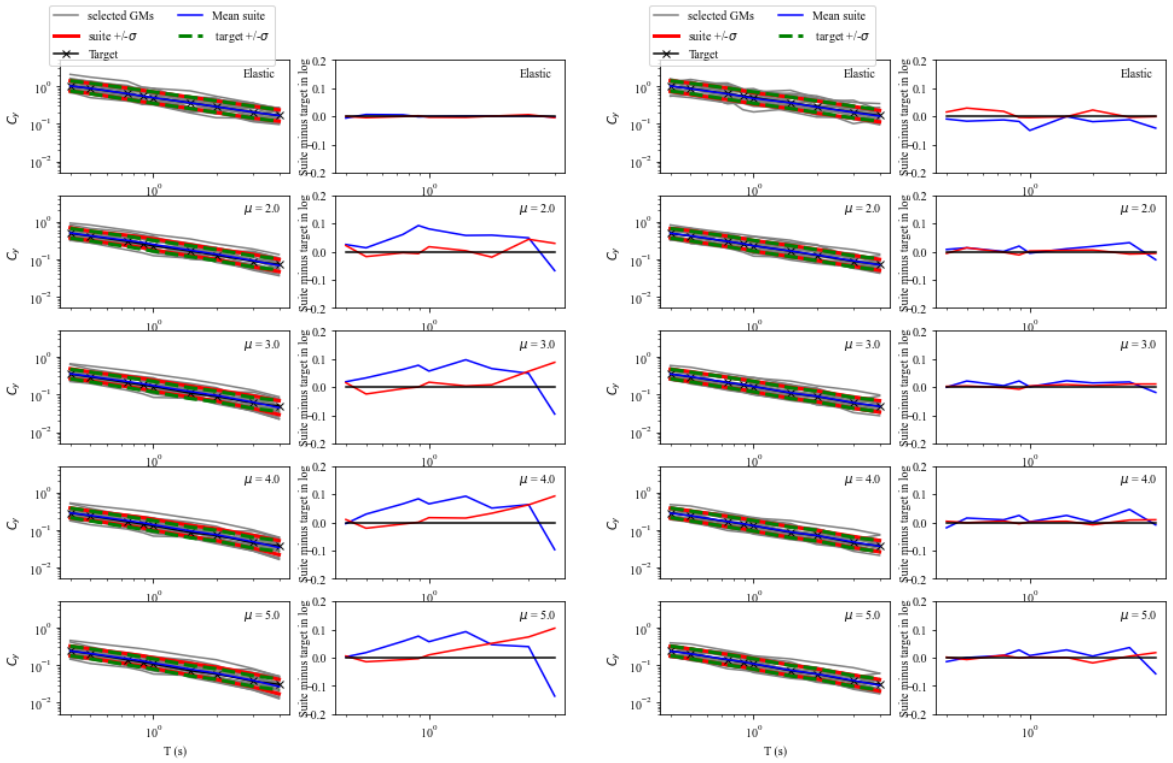

Figure A.17. Comparisons of the spectra of the suite mean and standard deviation with the targets for elastic and inelastic **UHS** representing different ductility levels, at **T_R=2475 years**, for **San Francisco** using elastic PSHA-based GMSS approach (left panel) and inelastic PSHA-based GMSS approach (right panel).

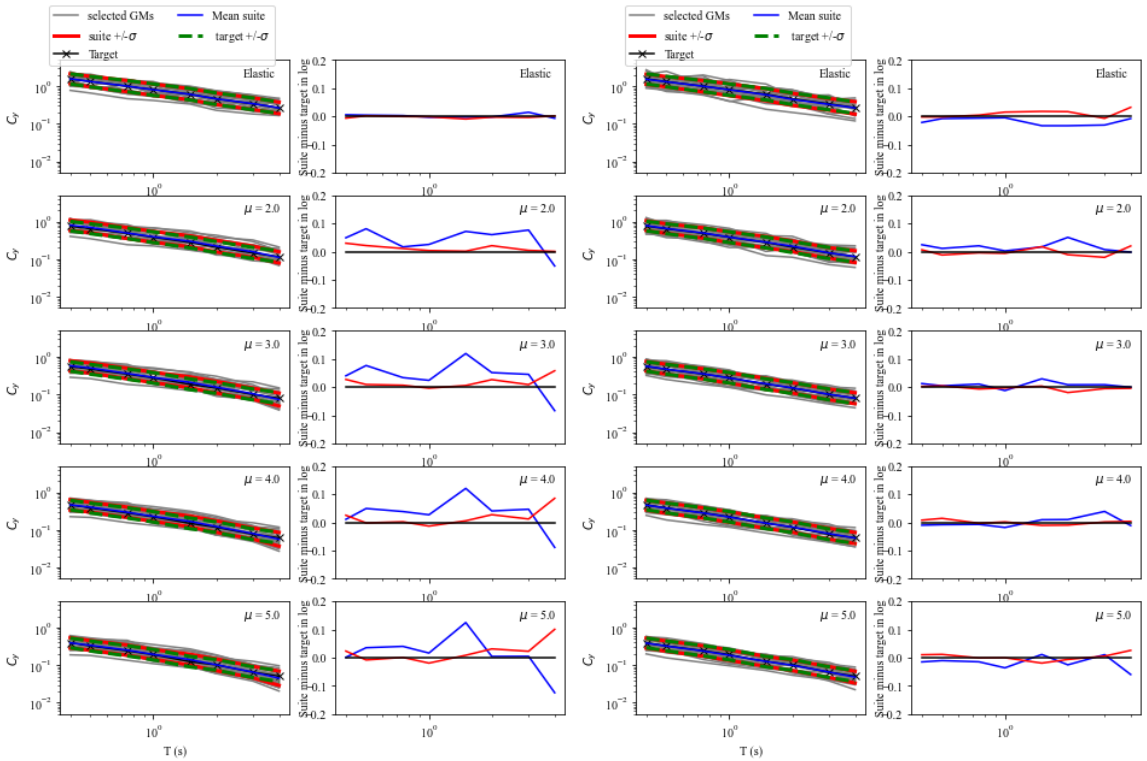

Figure A.18. Comparisons of the spectra of the suite mean and standard deviation with the targets for elastic and inelastic **UHS** representing different ductility levels, at **T_R=2475 years**, for **San Bernardino** using elastic PSHA-based GMSS approach (left panel) and inelastic PSHA-based GMSS approach (right panel).

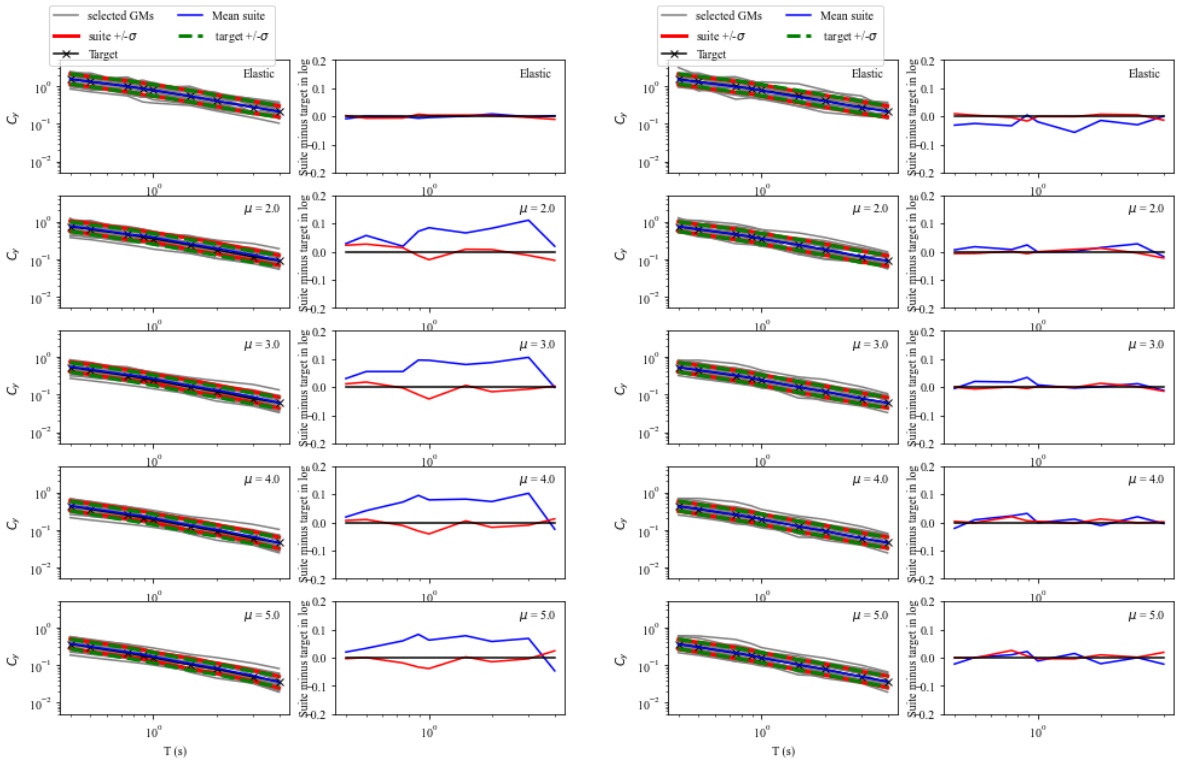

Figure A.19. Comparisons of the spectra of the suite mean and standard deviation with the targets for elastic and inelastic **UHS** representing different ductility levels, at **T_R=5000 years**, for **Oakland** using elastic PSHA-based GMSS approach (left panel) and inelastic PSHA-based GMSS approach (right panel).

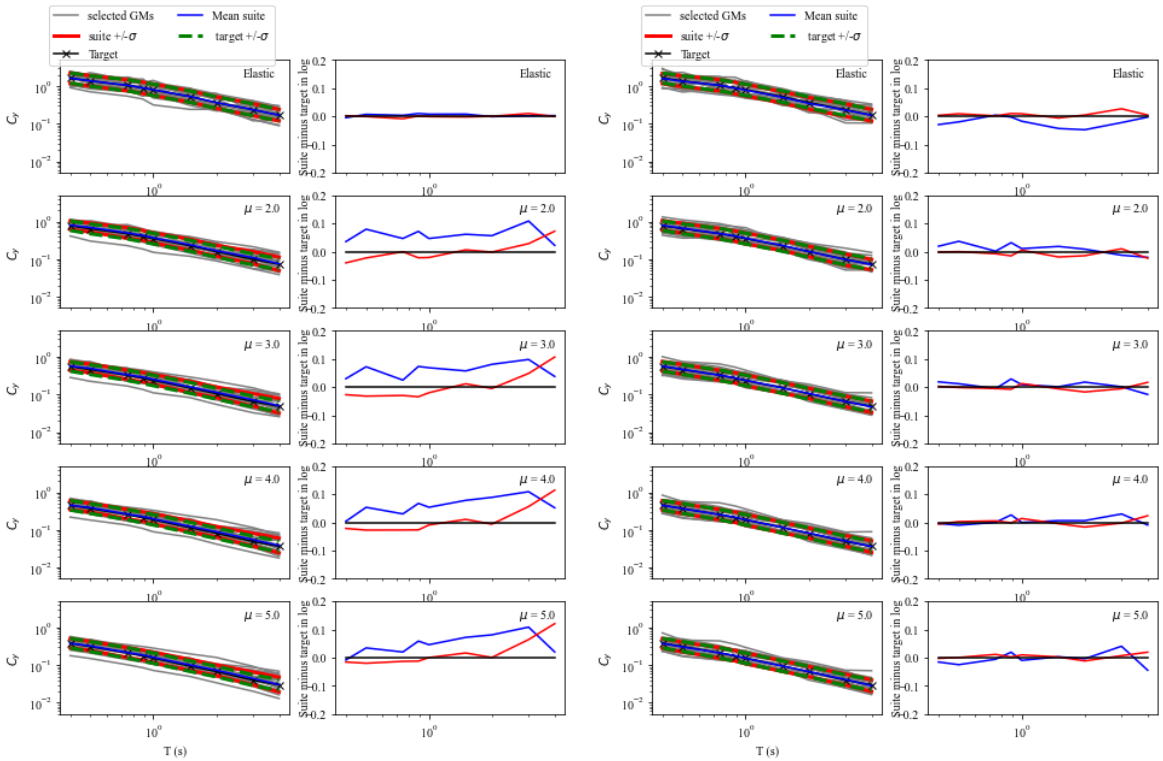

Figure A.20. Comparisons of the spectra of the suite mean and standard deviation with the targets for elastic and inelastic **UHS** representing different ductility levels, at **T_R=5000 years**, for **Los Angeles** using elastic PSHA-based GMSS approach (left panel) and inelastic PSHA-based GMSS approach (right panel).

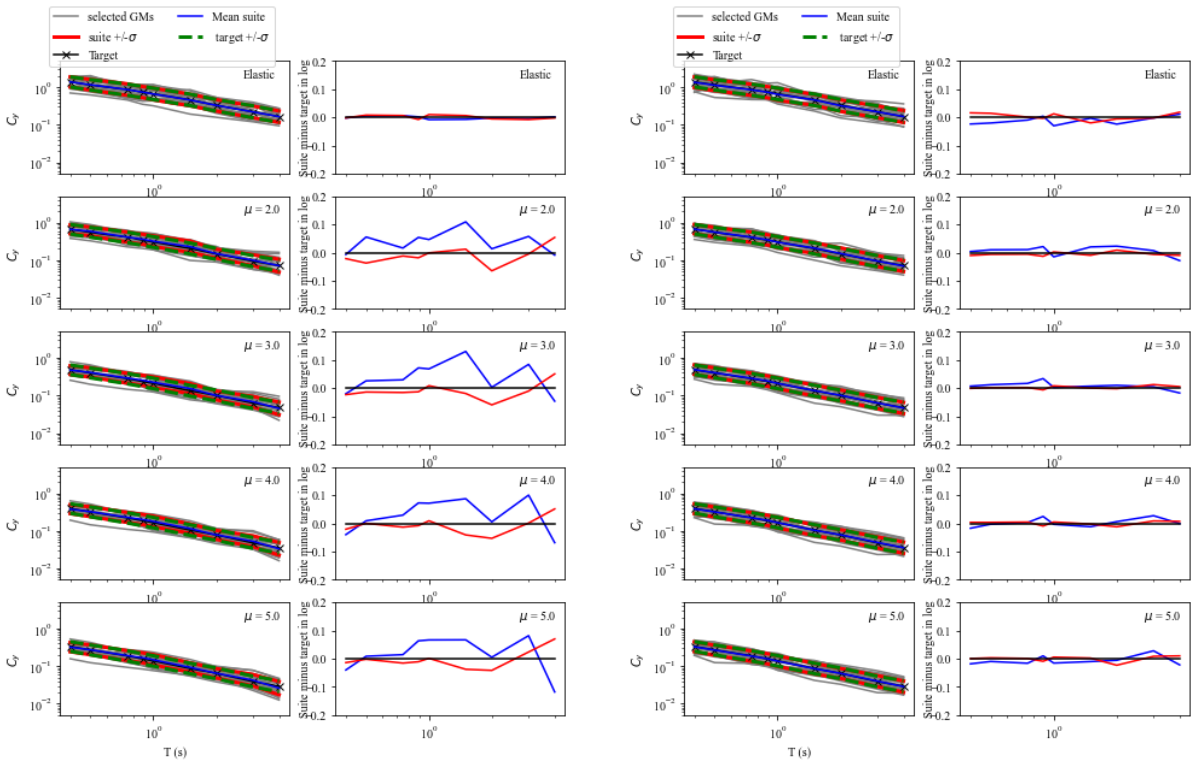

Figure A.21. Comparisons of the spectra of the suite mean and standard deviation with the targets for elastic and inelastic **UHS** representing different ductility levels, at **T_R=5000 years**, for **Long Beach** using elastic PSHA-based GMSS approach (left panel) and inelastic PSHA-based GMSS approach (right panel).

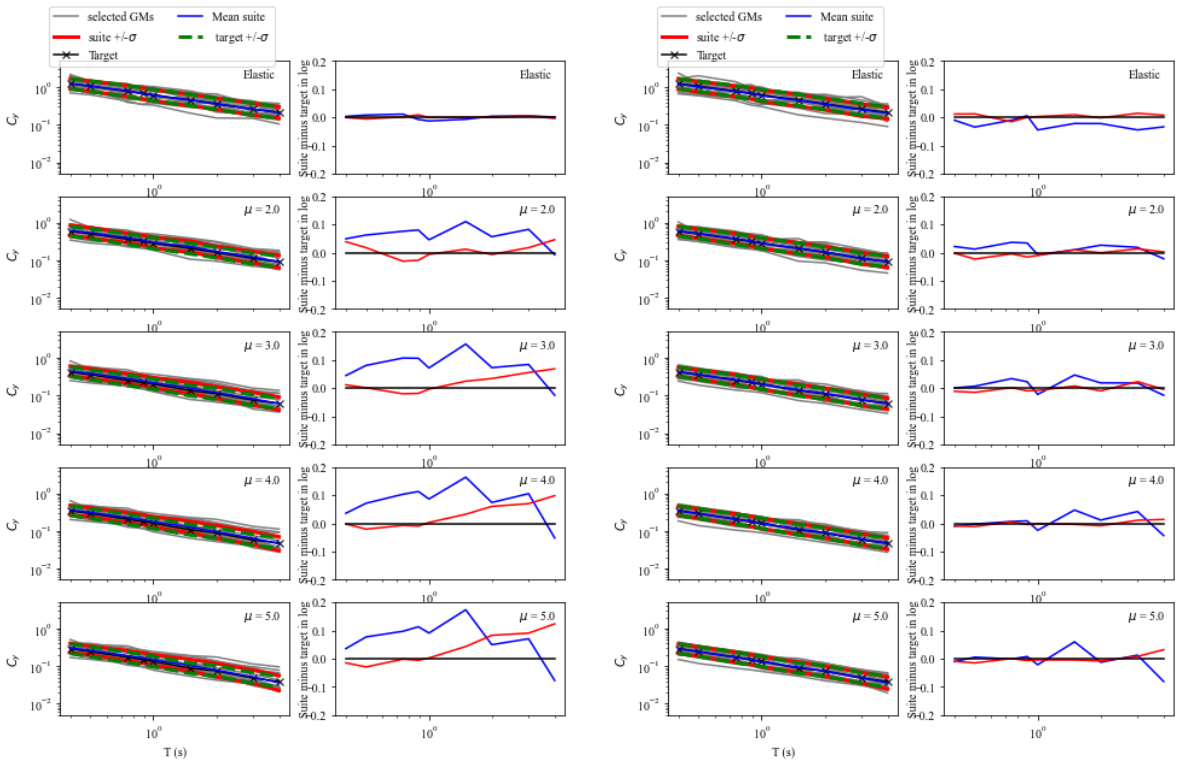

Figure A.22. Comparisons of the spectra of the suite mean and standard deviation with the targets for elastic and inelastic **UHS** representing different ductility levels, at **T_R=5000 years**, for **San Francisco** using elastic PSHA-based GMSS approach (left panel) and inelastic PSHA-based GMSS approach (right panel).

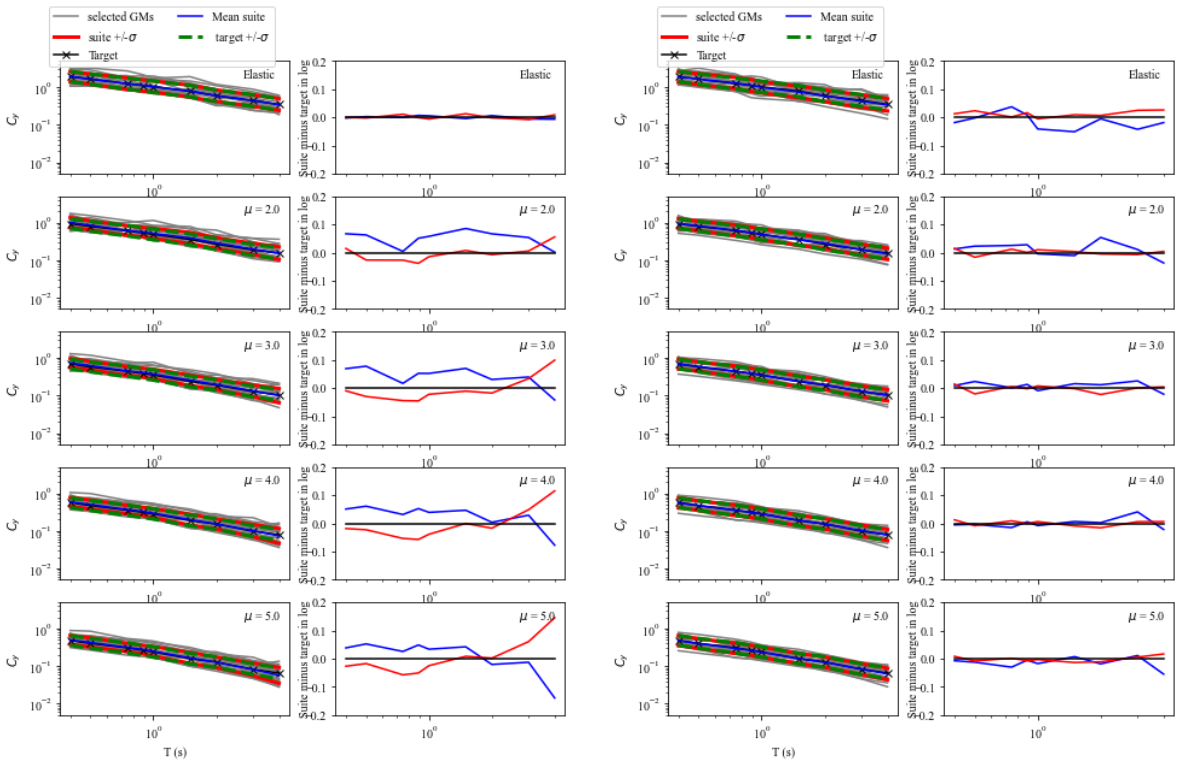

Figure A.23. Comparisons of the spectra of the suite mean and standard deviation with the targets for elastic and inelastic **UHS** representing different ductility levels, at **T_R=5000 years**, for **San Bernardino** using elastic PSHA-based GMSS approach (left panel) and inelastic PSHA-based GMSS approach (right panel).

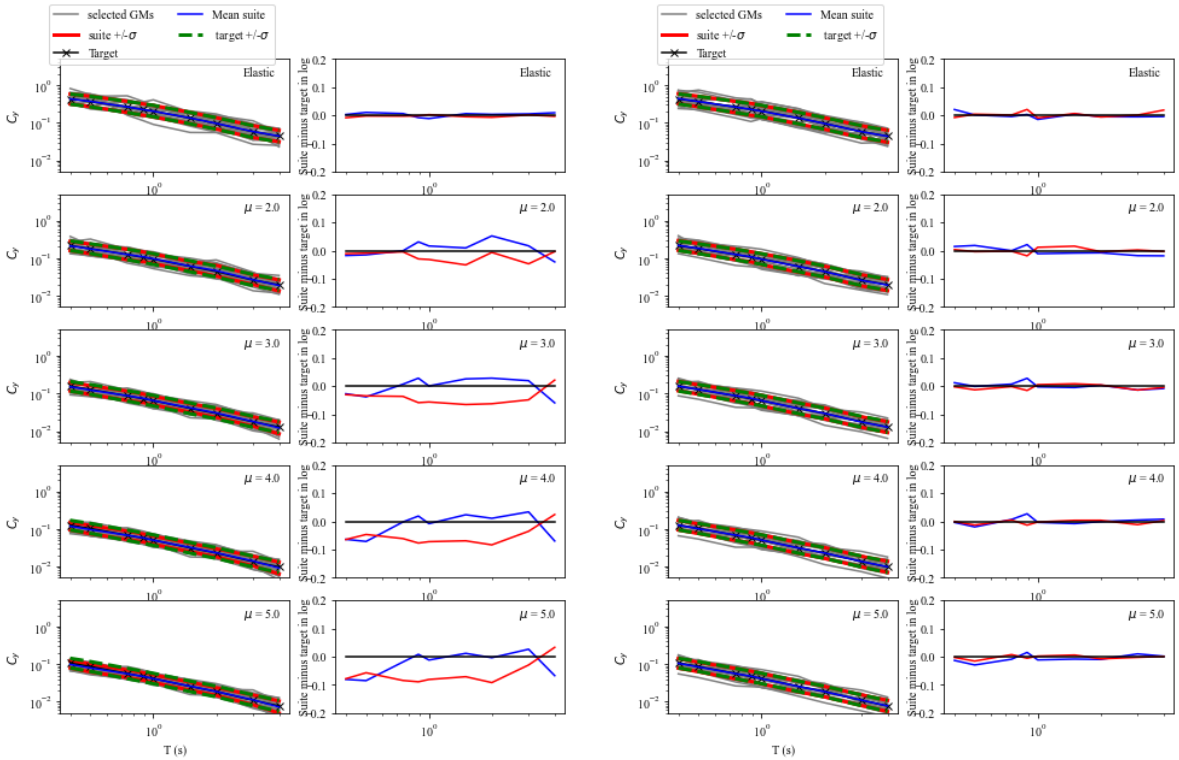

Figure A.24. Comparisons of the spectra of the suite mean and standard deviation with the targets for elastic and inelastic **CMS** representing different ductility levels, at **T_R=200 years**, for **Oakland** using elastic PSHA-based GMSS approach (left panel) and inelastic PSHA-based GMSS approach (right panel).

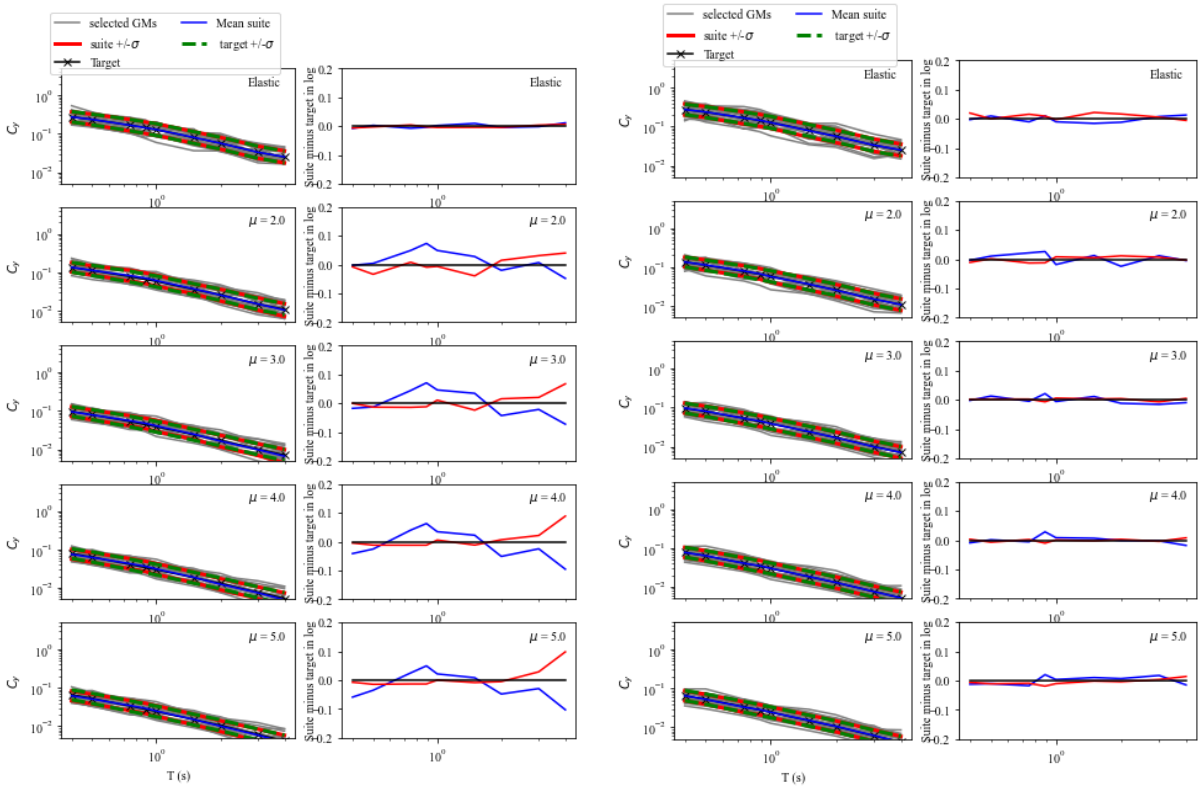

Figure A.25. Comparisons of the spectra of the suite mean and standard deviation with the targets for elastic and inelastic **CMS** representing different ductility levels, at **T_R=200 years**, for **Long Beach** using elastic PSHA-based GMSS approach (left panel) and inelastic PSHA-based GMSS approach (right panel).

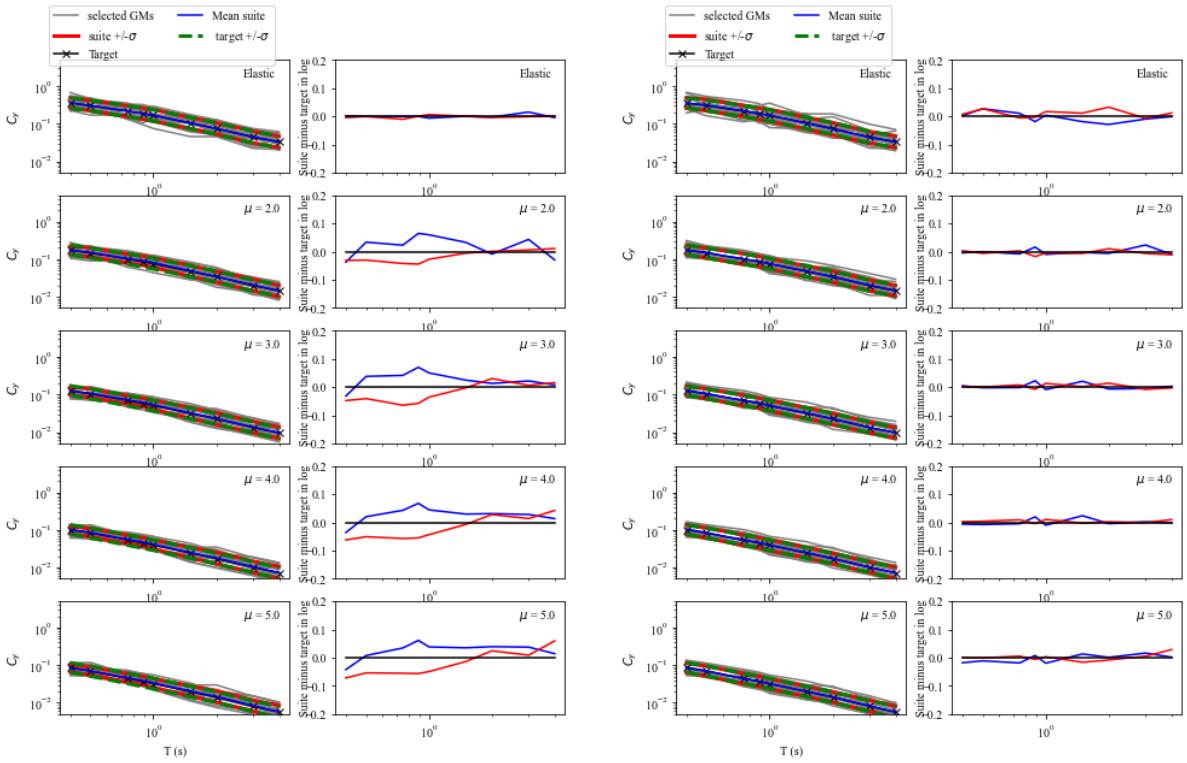

Figure A.26. Comparisons of the spectra of the suite mean and standard deviation with the targets for elastic and inelastic **CMS** representing different ductility levels, at **T_R=200 years**, for **Los Angeles** using elastic PSHA-based GMSS approach (left panel) and inelastic PSHA-based GMSS approach (right panel).

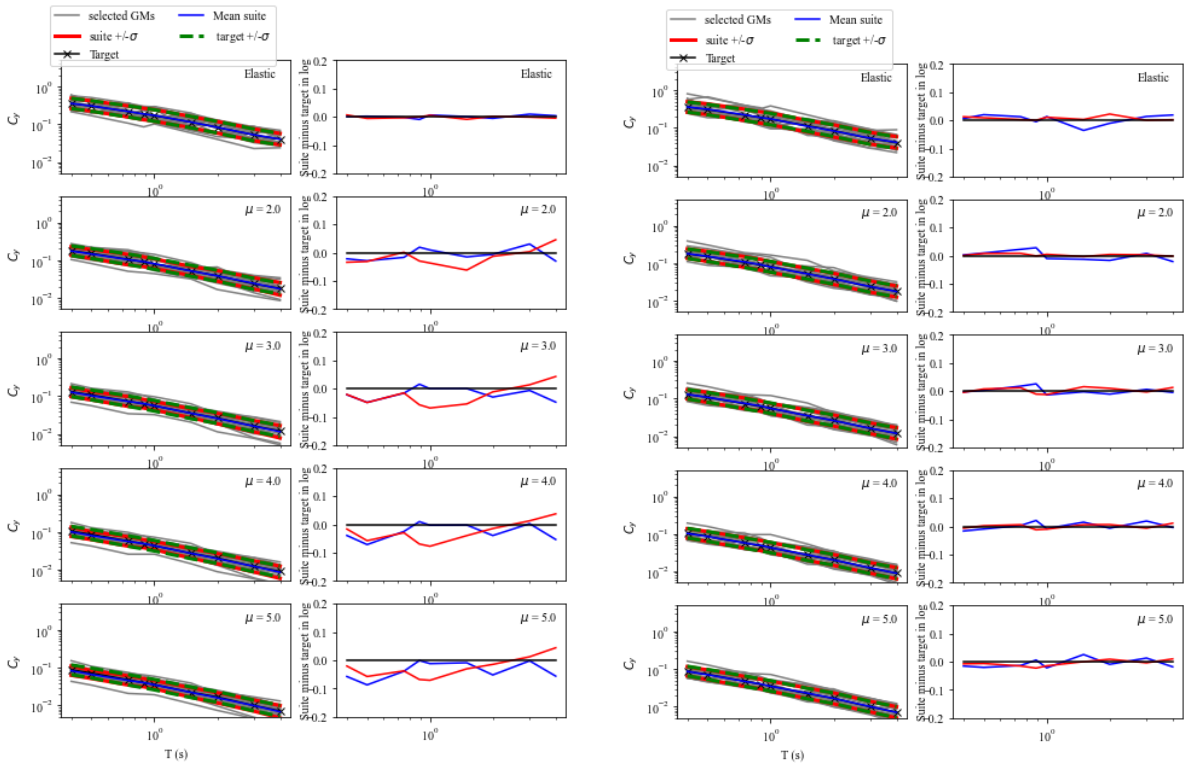

Figure A.27. Comparisons of the spectra of the suite mean and standard deviation with the targets for elastic and inelastic **CMS** representing different ductility levels, at **T_R=200 years,** for **San Francisco** using elastic PSHA-based GMSS approach (left panel) and inelastic PSHA-based GMSS approach (right panel).

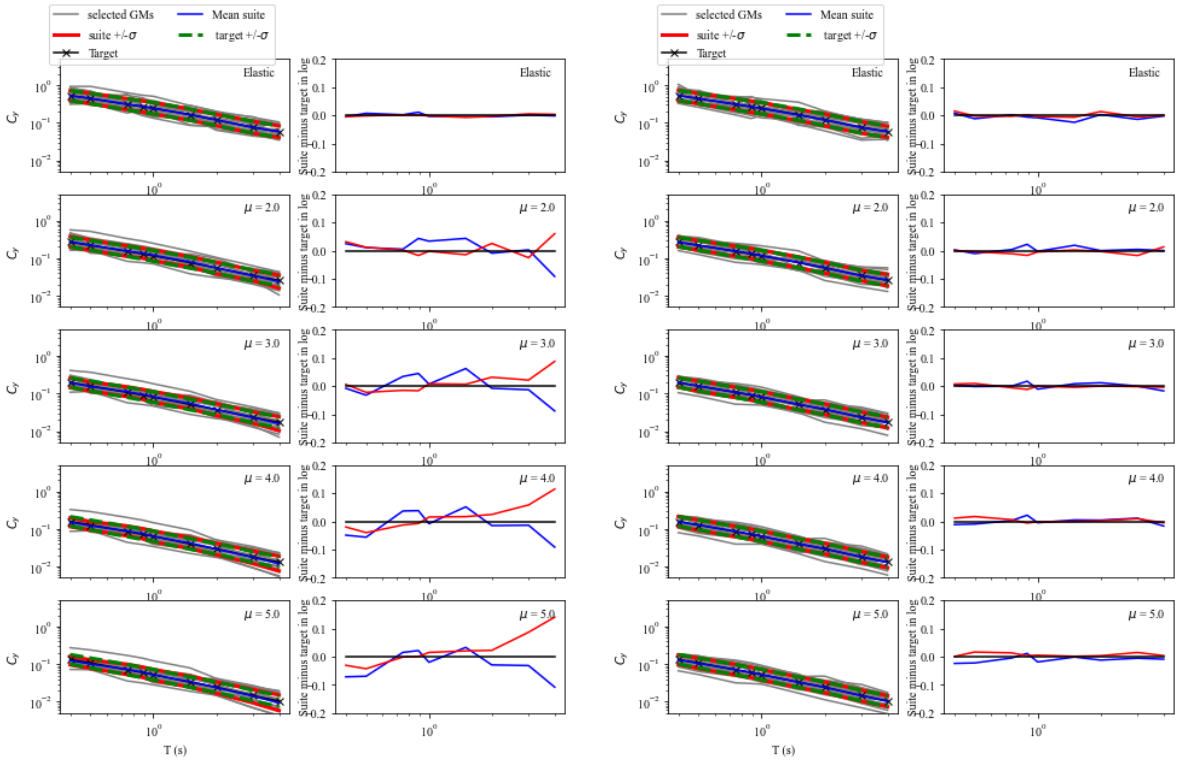

Figure A.28. Comparisons of the spectra of the suite mean and standard deviation with the targets for elastic and inelastic **CMS** representing different ductility levels, at **T_R=200 years**, for **San Bernardino** using elastic PSHA-based GMSS approach (left panel) and inelastic PSHA-based GMSS approach (right panel).

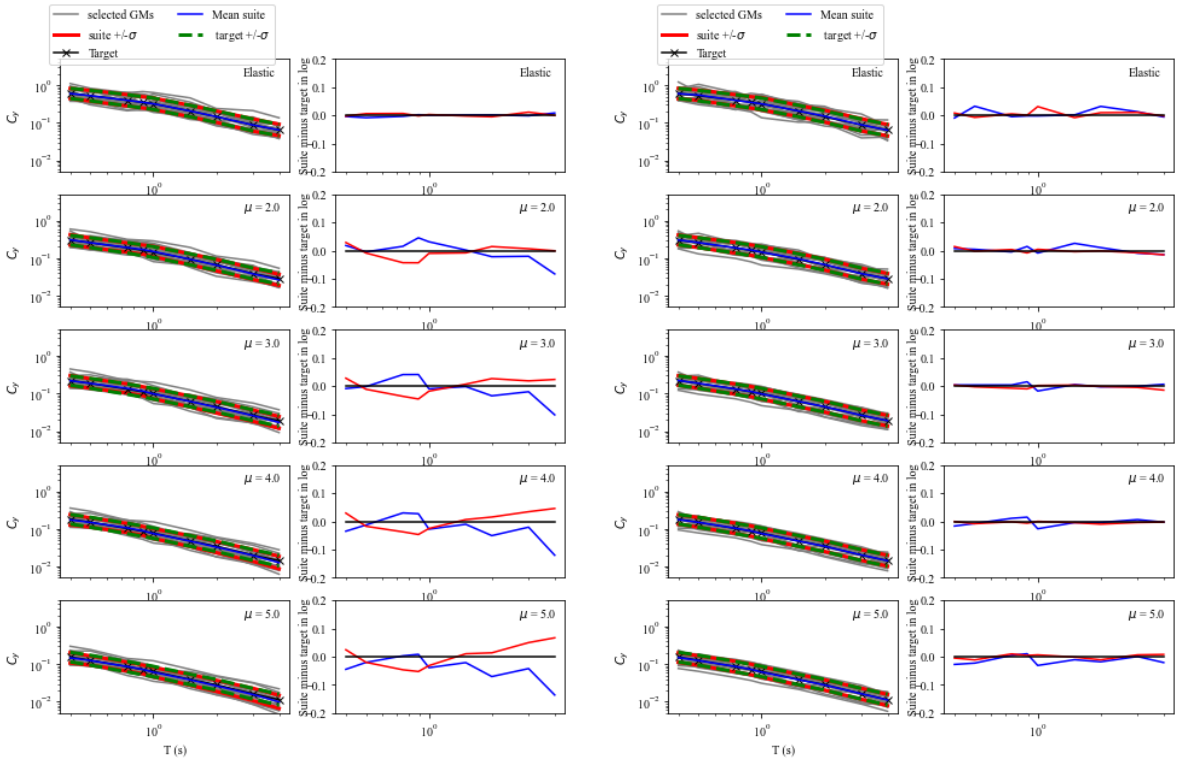

Figure A.29. Comparisons of the spectra of the suite mean and standard deviation with the targets for elastic and inelastic **CMS** representing different ductility levels, at **T_R=475 years**, for **Oakland** using elastic PSHA-based GMSS approach (left panel) and inelastic PSHA-based GMSS approach (right panel).

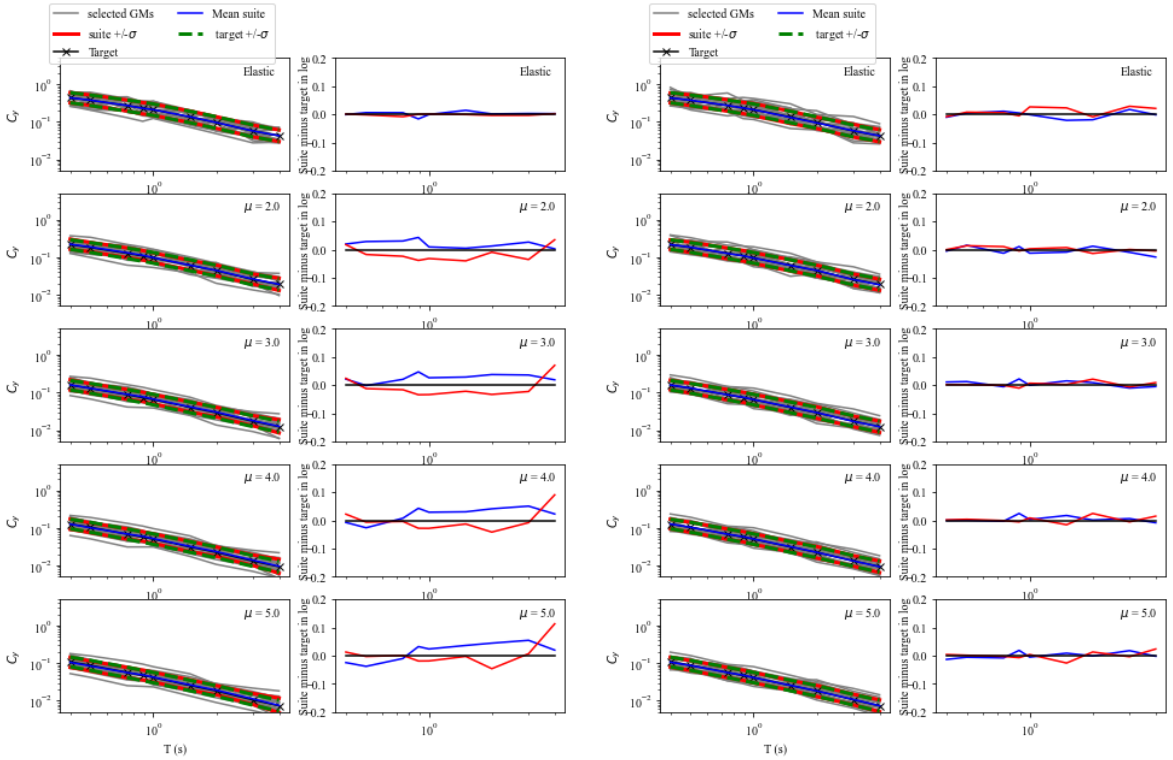

Figure A.30. Comparisons of the spectra of the suite mean and standard deviation with the targets for elastic and inelastic **CMS** representing different ductility levels, at **T_R=475 years**, for **Long Beach** using elastic PSHA-based GMSS approach (left panel) and inelastic PSHA-based GMSS approach (right panel).

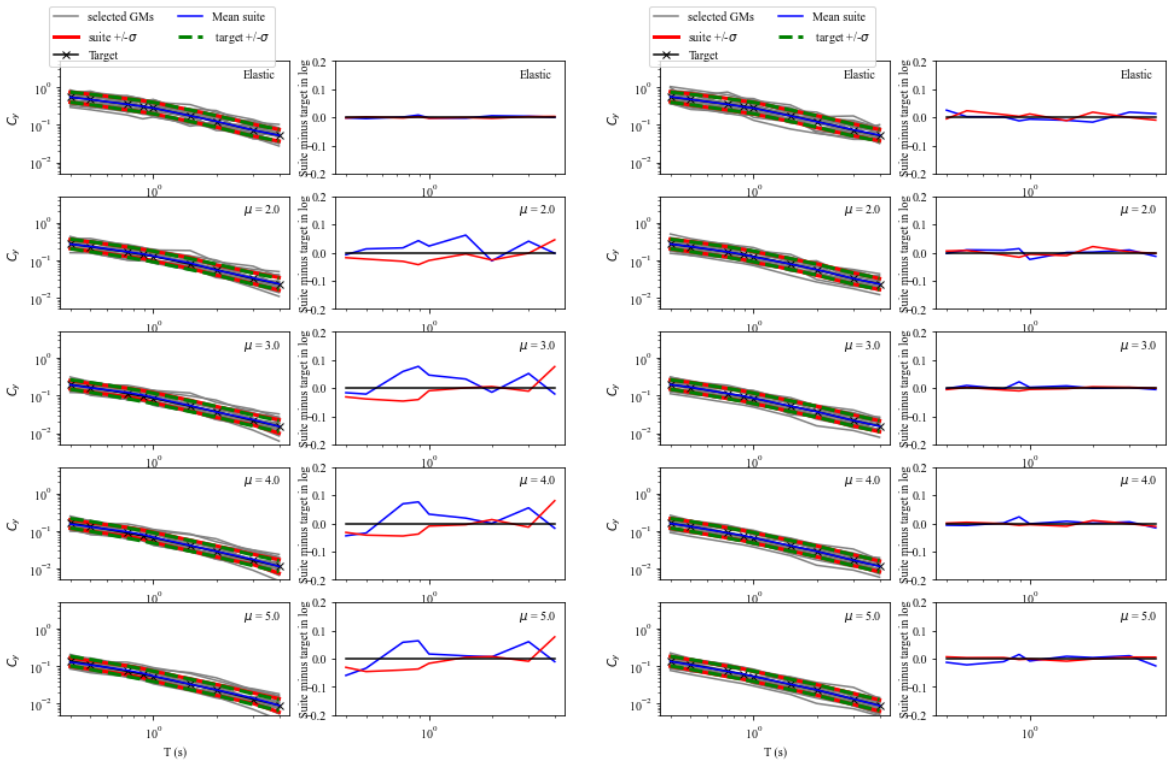

Figure A.31. Comparisons of the spectra of the suite mean and standard deviation with the targets for elastic and inelastic **CMS** representing different ductility levels, at **T_R=475 years**, for **Los Angeles** using elastic PSHA-based GMSS approach (left panel) and inelastic PSHA-based GMSS approach (right panel).

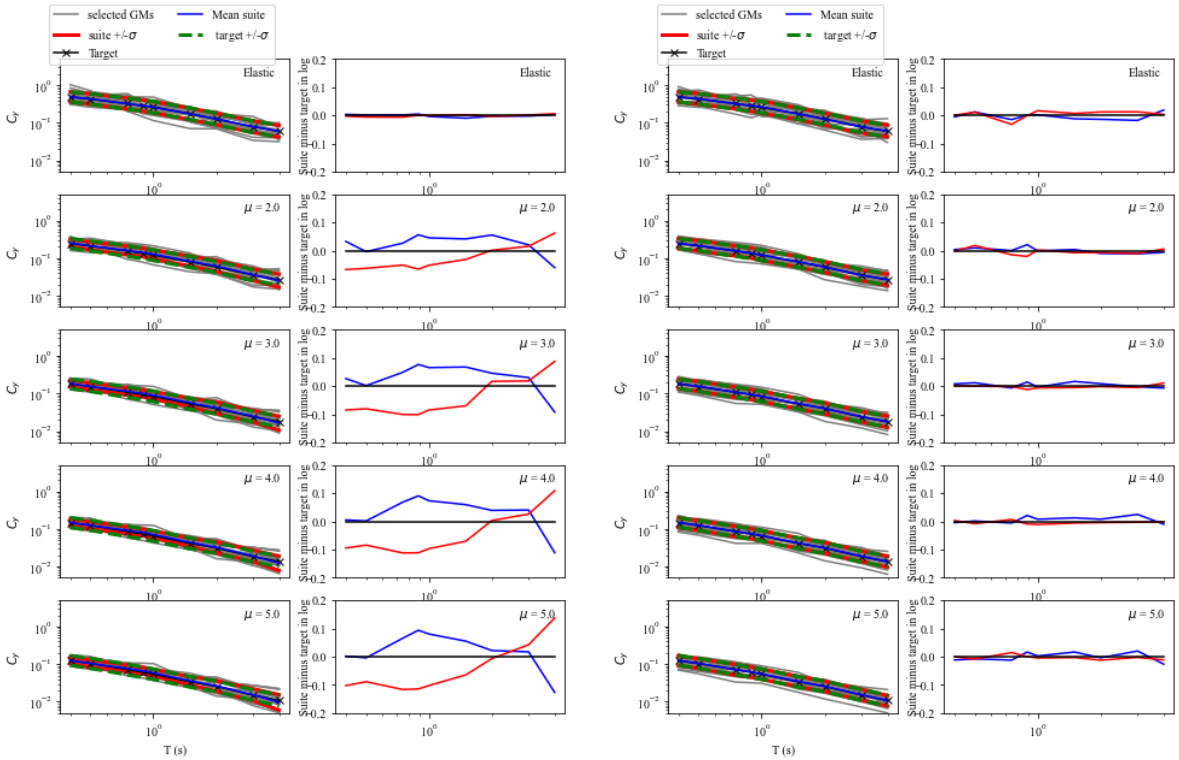

Figure A.32. Comparisons of the spectra of the suite mean and standard deviation with the targets for elastic and inelastic **CMS** representing different ductility levels, at **T_R=475 years**, for **San Francisco** using elastic PSHA-based GMSS approach (left panel) and inelastic PSHA-based GMSS approach (right panel).

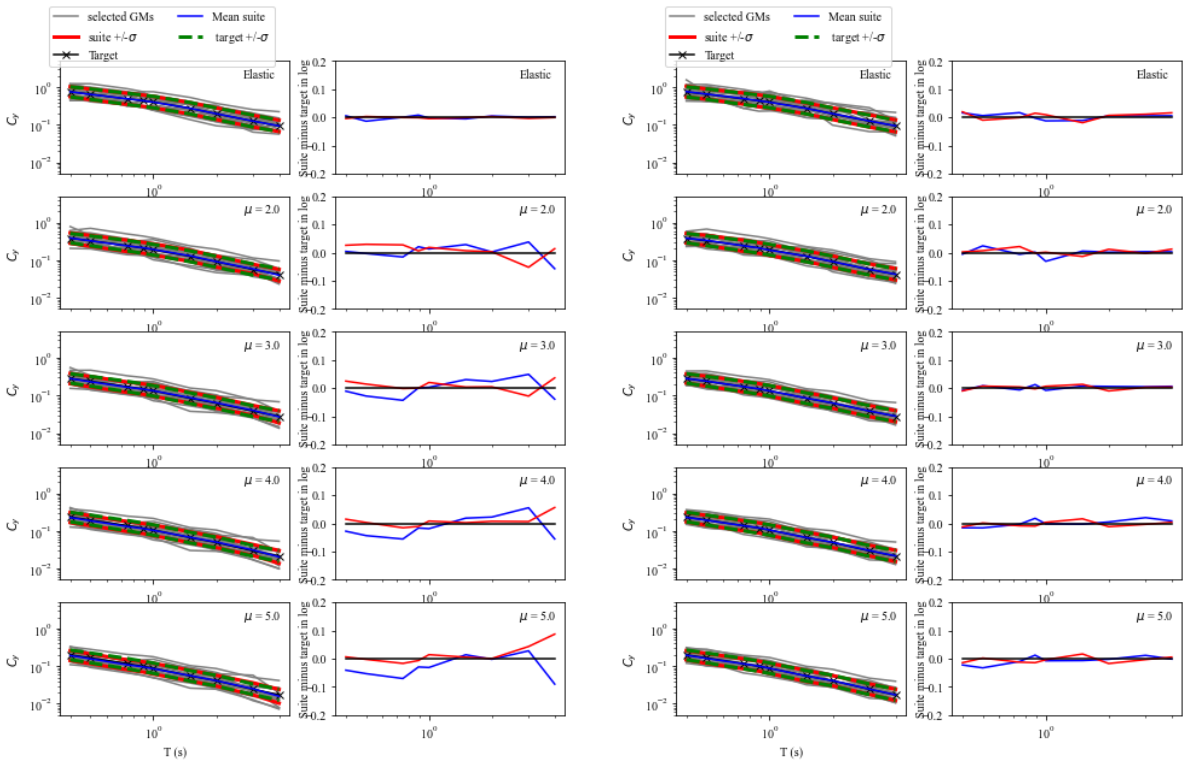

Figure A.33. Comparisons of the spectra of the suite mean and standard deviation with the targets for elastic and inelastic **CMS** representing different ductility levels, at **T_R=475 years**, for **San Bernardino** using elastic PSHA-based GMSS approach (left panel) and inelastic PSHA-based GMSS approach (right panel).

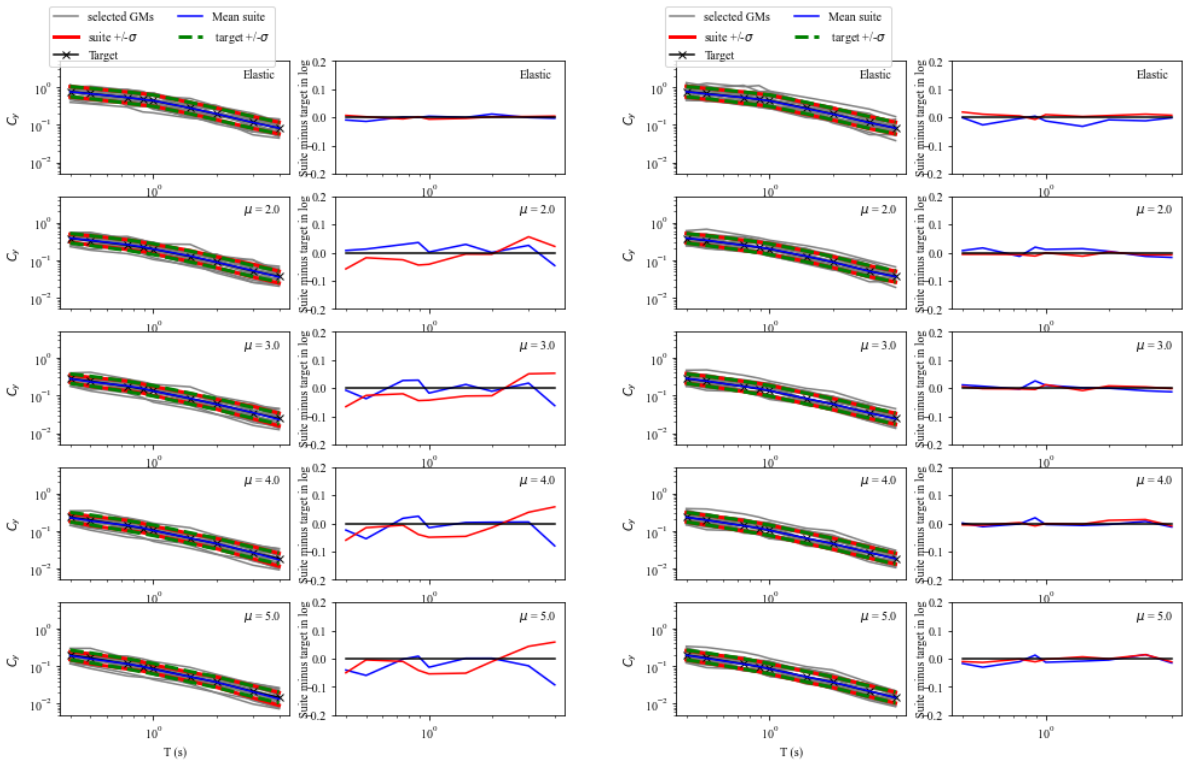

Figure A.34. Comparisons of the spectra of the suite mean and standard deviation with the targets for elastic and inelastic **CMS** representing different ductility levels, at **T_R=975 years**, for **Oakland** using elastic PSHA-based GMSS approach (left panel) and inelastic PSHA-based GMSS approach (right panel).

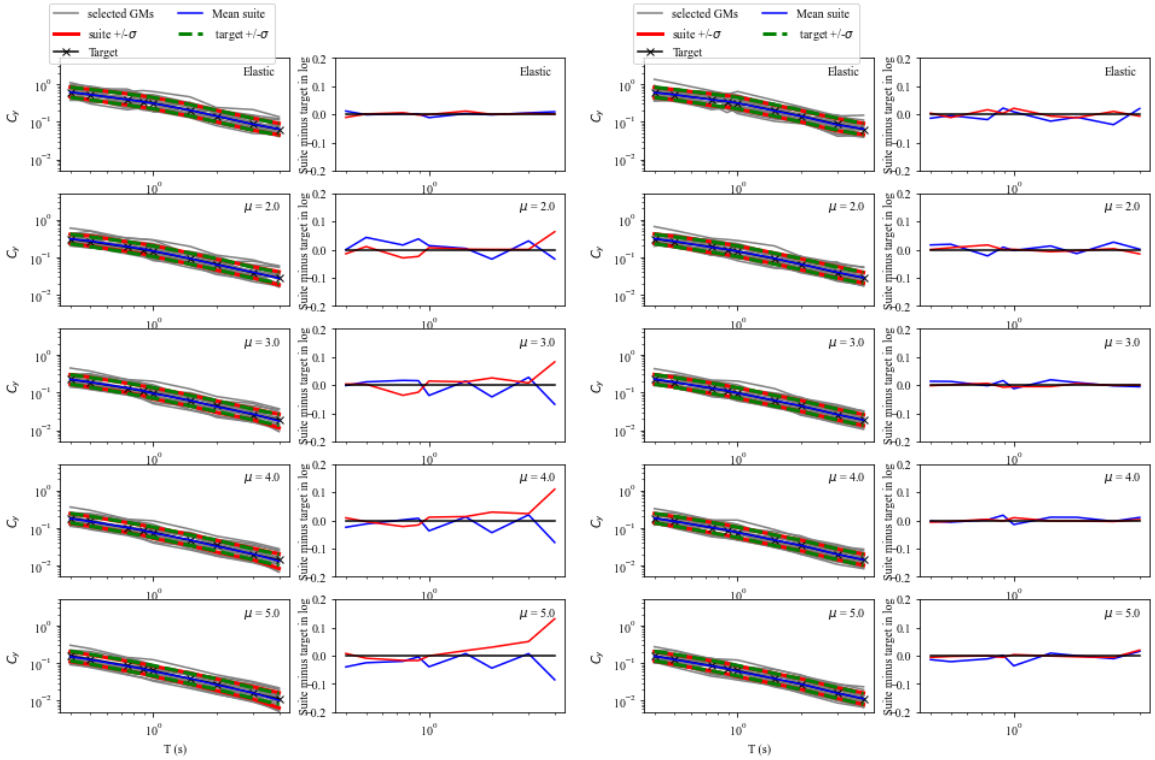

Figure A.35. Comparisons of the spectra of the suite mean and standard deviation with the targets for elastic and inelastic **CMS** representing different ductility levels, at **T_R=975 years**, for **Long Beach** using elastic PSHA-based GMSS approach (left panel) and inelastic PSHA-based GMSS approach (right panel).

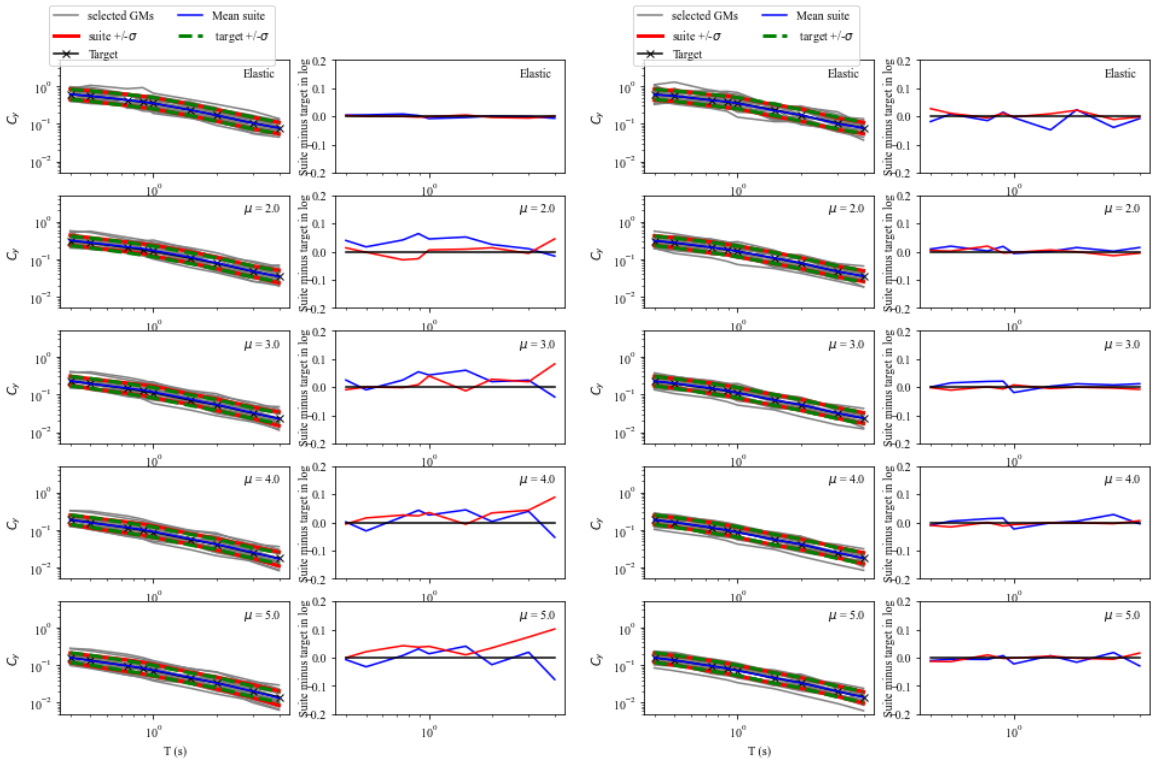

Figure A.36. Comparisons of the spectra of the suite mean and standard deviation with the targets for elastic and inelastic **CMS** representing different ductility levels, at **T_R=975 years**, for **San Francisco** using elastic PSHA-based GMSS approach (left panel) and inelastic PSHA-based GMSS approach (right panel).

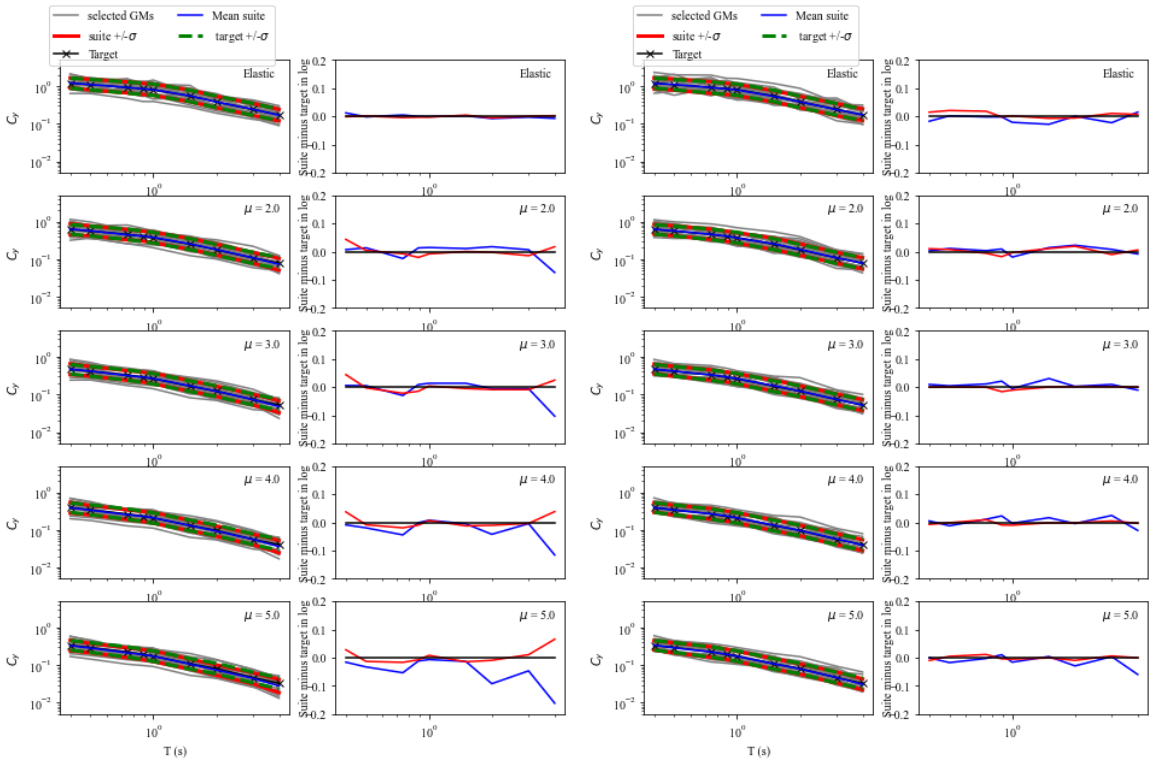

Figure A.37. Comparisons of the spectra of the suite mean and standard deviation with the targets for elastic and inelastic **CMS** representing different ductility levels, at **T_R=975 years**, for **San Bernardino** using elastic PSHA-based GMSS approach (left panel) and inelastic PSHA-based GMSS approach (right panel).

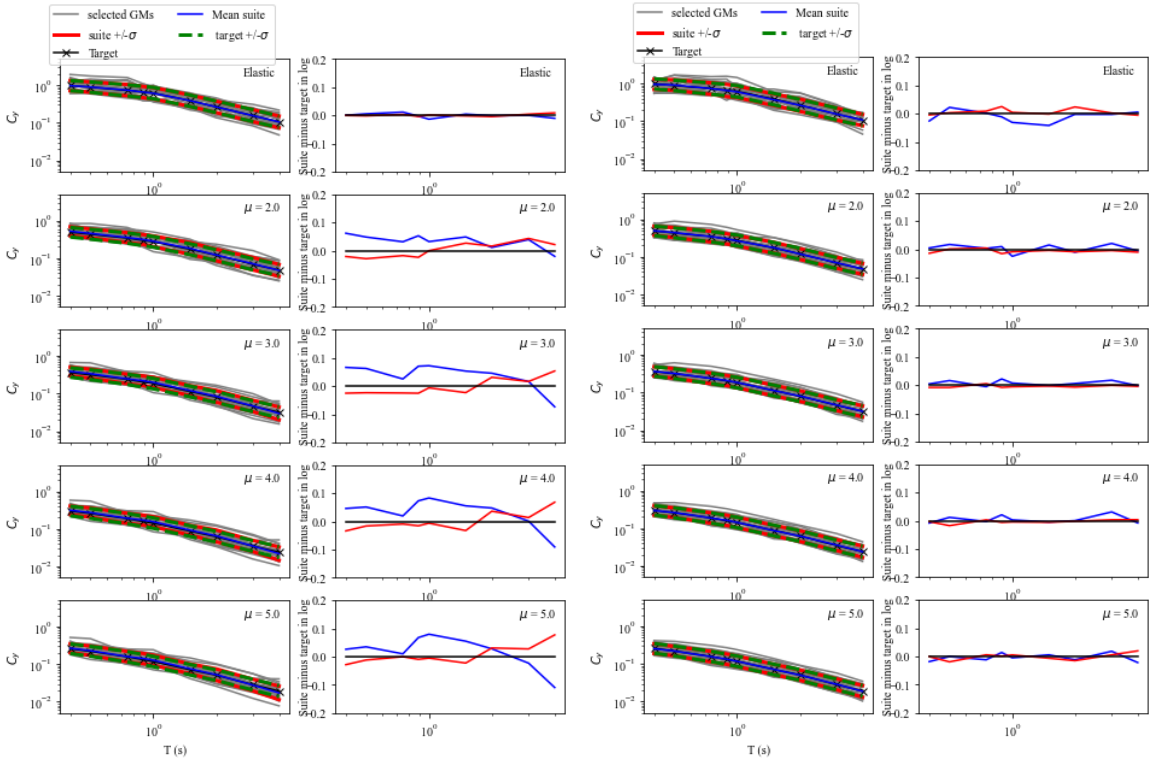

Figure A.38. Comparisons of the spectra of the suite mean and standard deviation with the targets for elastic and inelastic **CMS** representing different ductility levels, at **T_R=2475 years**, for **Oakland** using elastic PSHA-based GMSS approach (left panel) and inelastic PSHA-based GMSS approach (right panel).

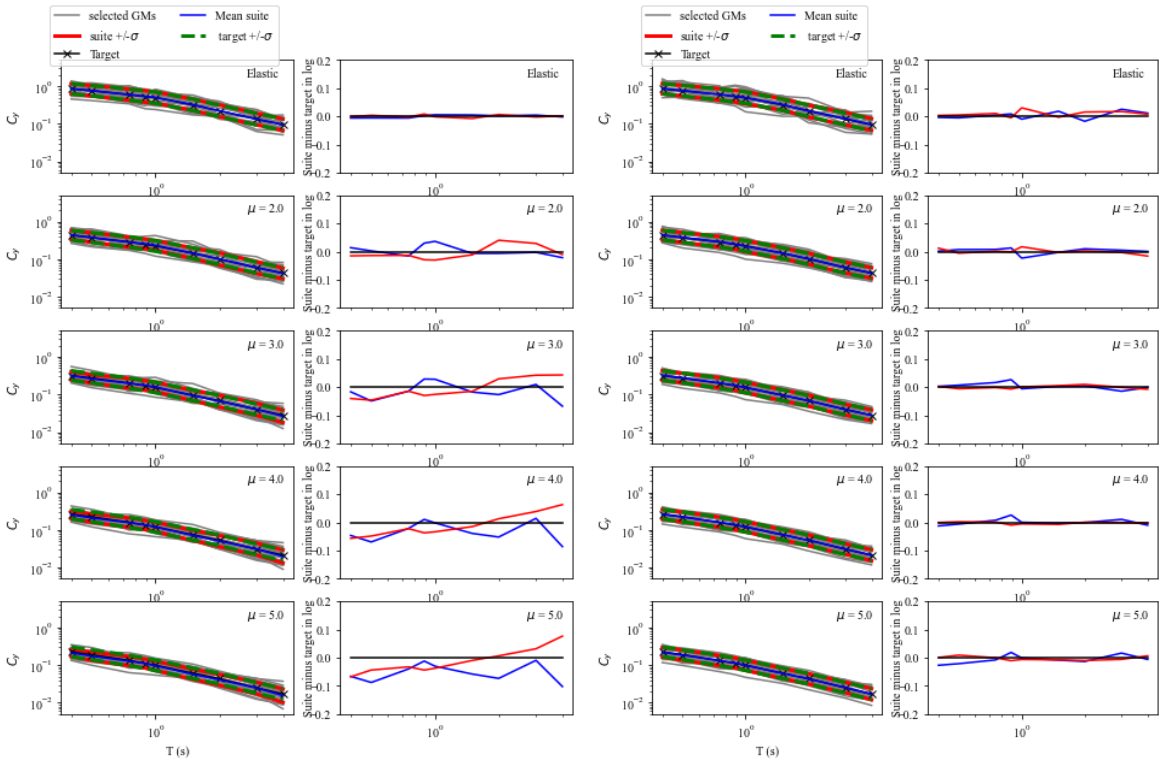

Figure A.39. Comparisons of the spectra of the suite mean and standard deviation with the targets for elastic and inelastic **CMS** representing different ductility levels, at **T_R=2475 years**, for **Long Beach** using elastic PSHA-based GMSS approach (left panel) and inelastic PSHA-based GMSS approach (right panel).

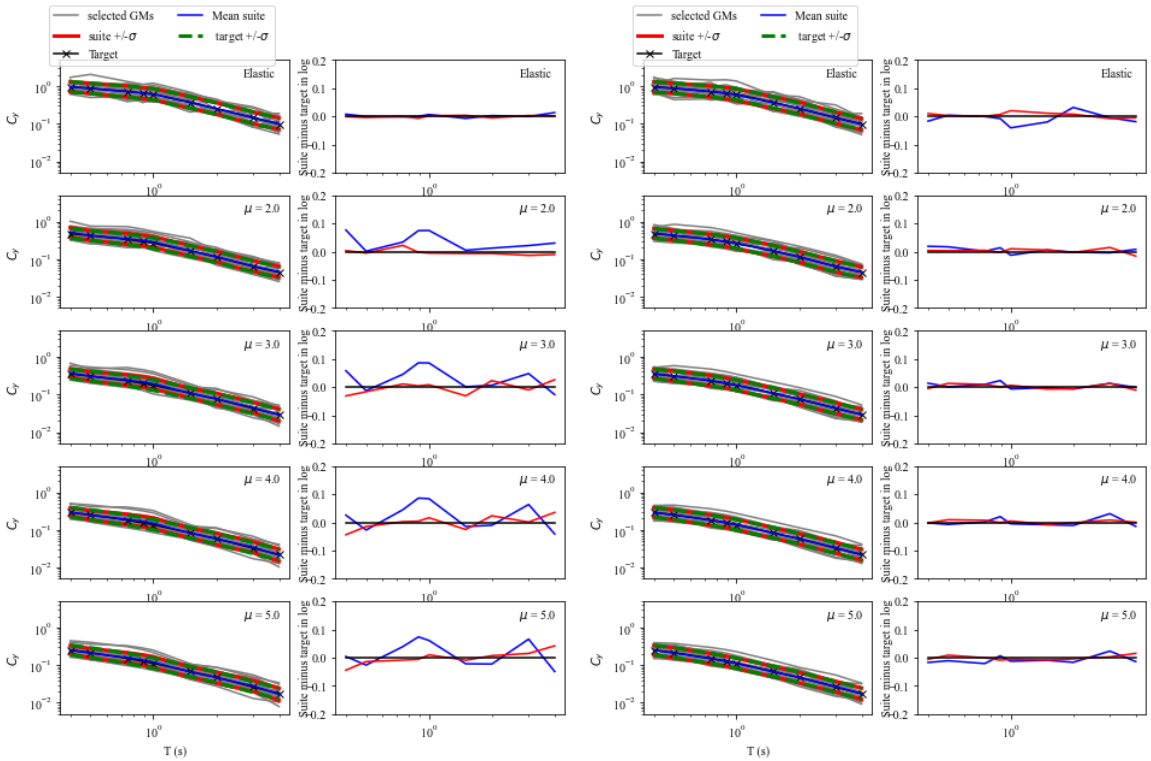

Figure A.40. Comparisons of the spectra of the suite mean and standard deviation with the targets for elastic and inelastic **CMS** representing different ductility levels, at **T_R=2475 years**, for **Los Angeles** using elastic PSHA-based GMSS approach (left panel) and inelastic PSHA-based GMSS approach (right panel).

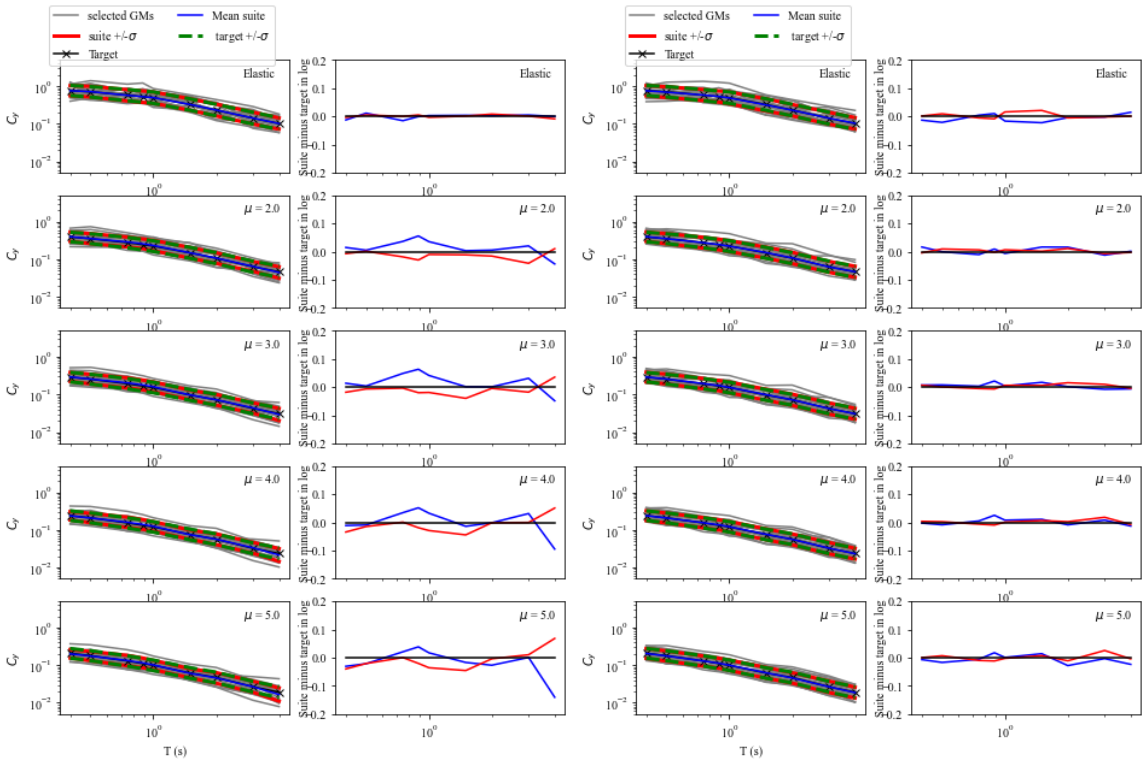

Figure A.41. Comparisons of the spectra of the suite mean and standard deviation with the targets for elastic and inelastic **CMS** representing different ductility levels, at **T_R=2475 years**, for **San Francisco** using elastic PSHA-based GMSS approach (left panel) and inelastic PSHA-based GMSS approach (right panel).

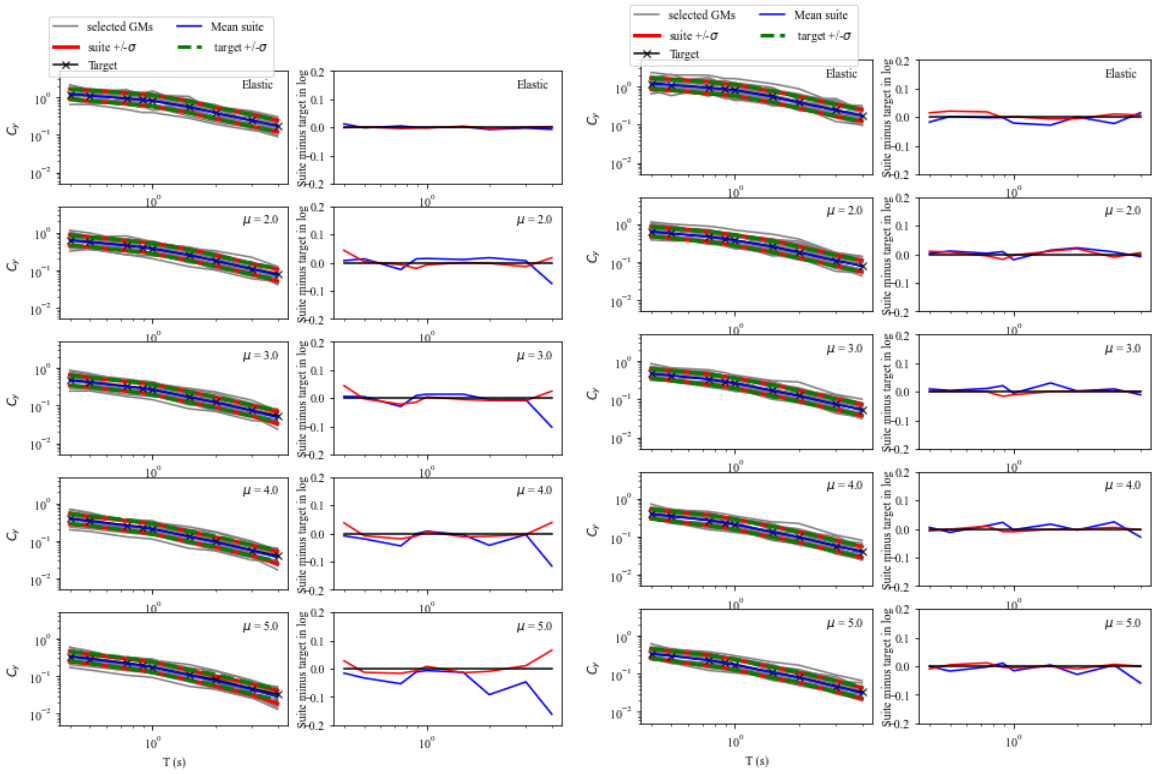

Figure A.42. Comparisons of the spectra of the suite mean and standard deviation with the targets for elastic and inelastic **CMS** representing different ductility levels, at **T_R=2475 years**, for **San Bernardino** using elastic PSHA-based GMSS approach (left panel) and inelastic PSHA-based GMSS approach (right panel).

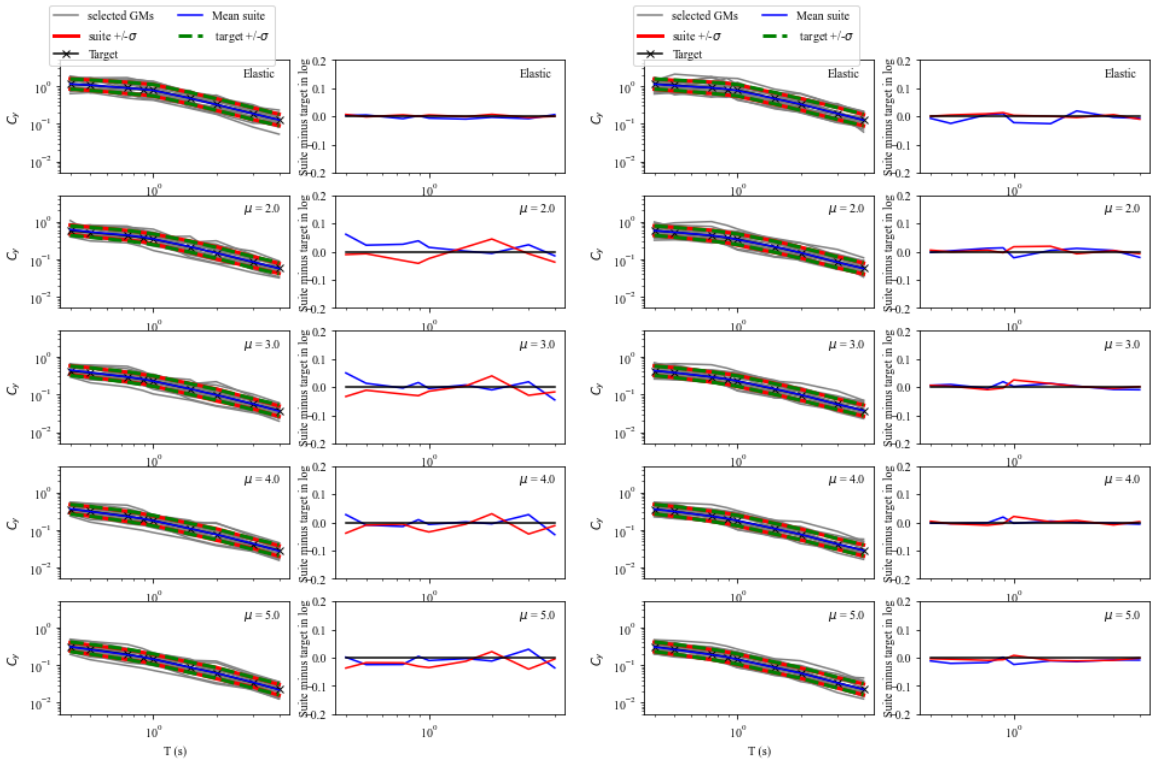

Figure A.43. Comparisons of the spectra of the suite mean and standard deviation with the targets for elastic and inelastic **CMS** representing different ductility levels, at **T_R=5000 years**, for **Oakland** using elastic PSHA-based GMSS approach (left panel) and inelastic PSHA-based GMSS approach (right panel).

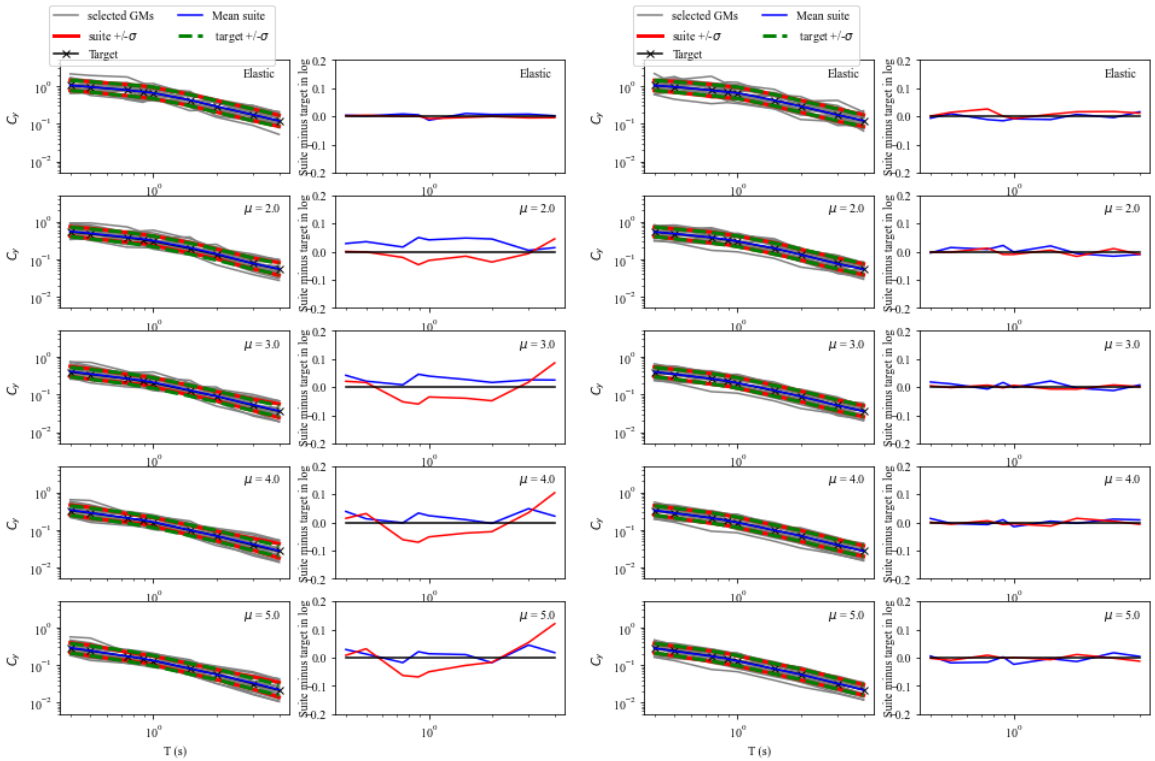

Figure A.44. Comparisons of the spectra of the suite mean and standard deviation with the targets for elastic and inelastic **CMS** representing different ductility levels, at **T_R=5000 years**, for **Long Beach** using elastic PSHA-based GMSS approach (left panel) and inelastic PSHA-based GMSS approach (right panel).

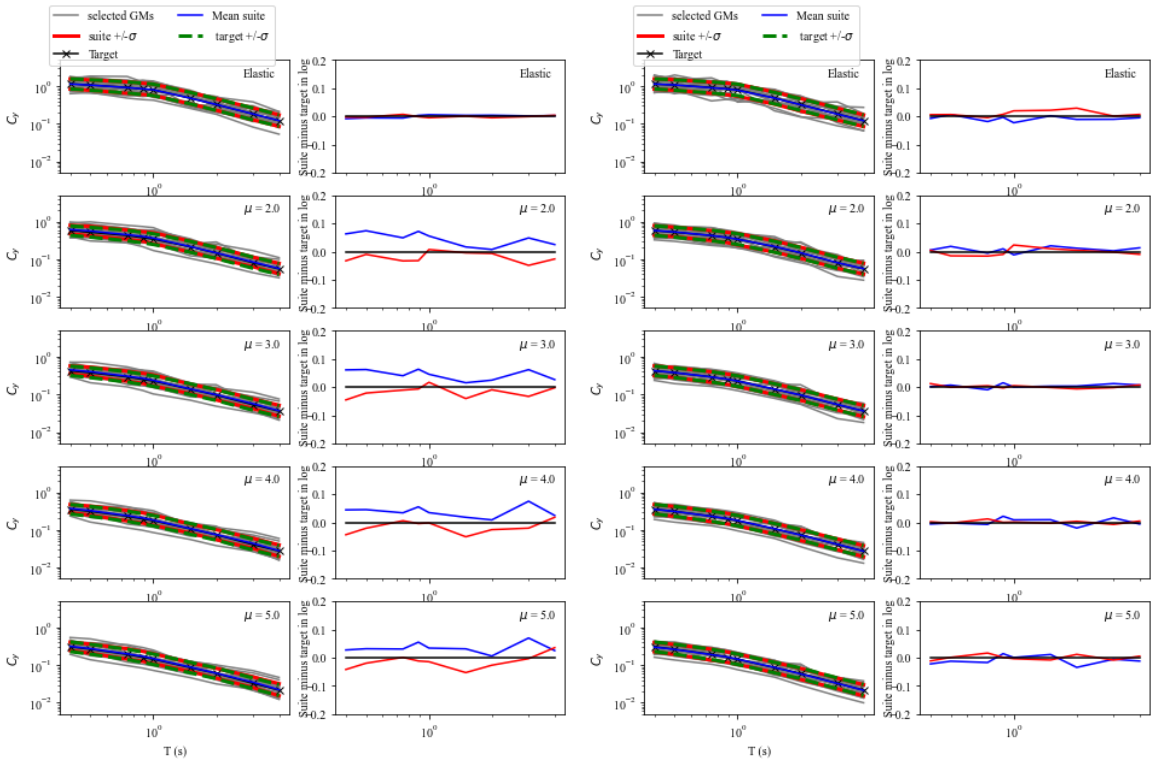

Figure A.45. Comparisons of the spectra of the suite mean and standard deviation with the targets for elastic and inelastic **CMS** representing different ductility levels, at **T_R=5000 years**, for **Los Angeles** using elastic PSHA-based GMSS approach (left panel) and inelastic PSHA-based GMSS approach (right panel).

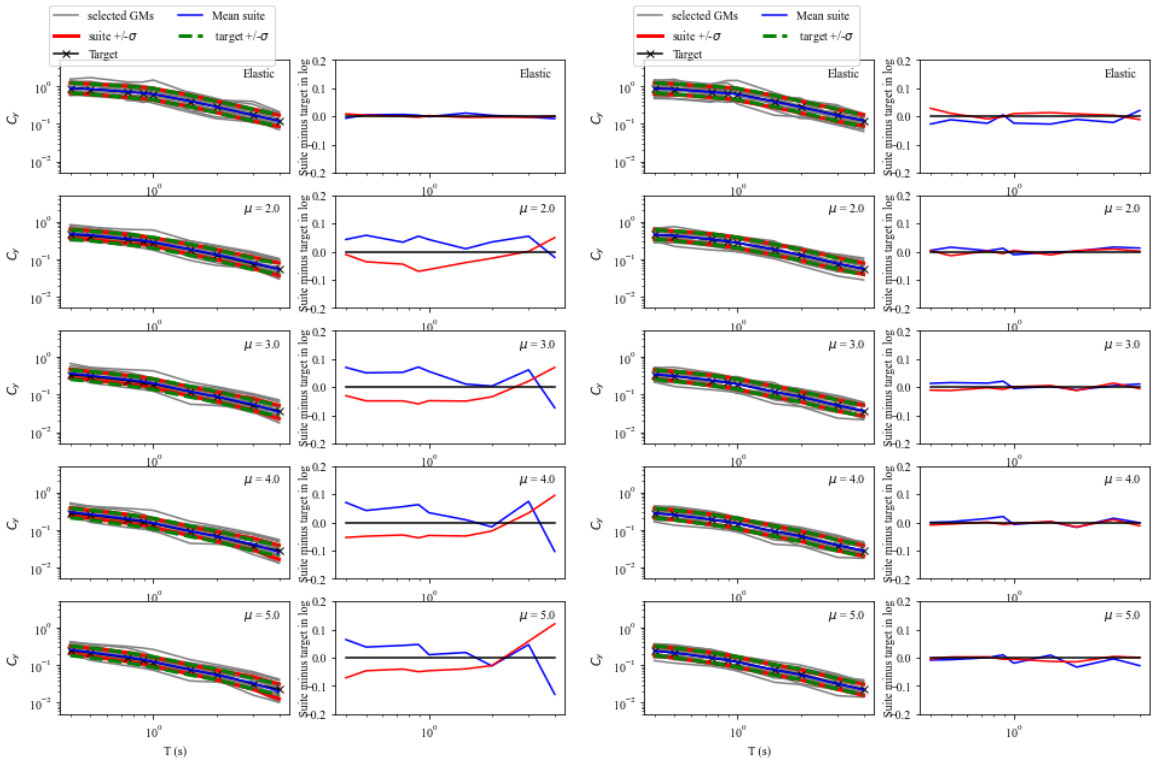

Figure A.46. Comparisons of the spectra of the suite mean and standard deviation with the targets for elastic and inelastic **CMS** representing different ductility levels, at **T_R=5000 years**, for **San Francisco** using elastic PSHA-based GMSS approach (left panel) and inelastic PSHA-based GMSS approach (right panel).

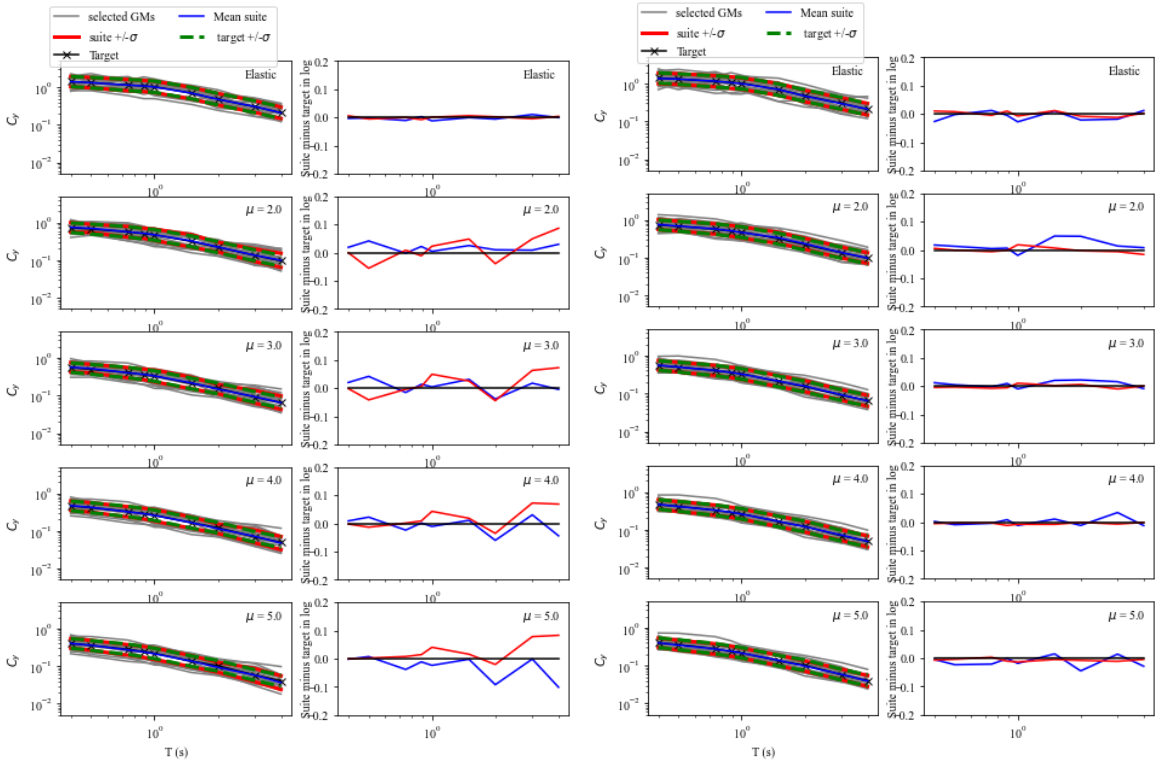

Figure A.47. Comparisons of the spectra of the suite mean and standard deviation with the targets for elastic and inelastic **CMS** representing different ductility levels, at **T_R=5000 years**, for **San Bernardino** using elastic PSHA-based GMSS approach (left panel) and inelastic PSHA-based GMSS approach (right panel).